SOURCE DEPTHS UTILIZING BROAD BAND DATA

George H. Sutton, Jerry A. Carter and Noël Barstow
Rondout Associates, Incorporated
P.O. Box 224
Stone Ridge, New York 12484

MARCH 1987

FINAL TECHNICAL REPORT
ARPA ORDER NO: 4435
CONTRACT: F08606-85-C-0029

Prepared for:
DEFENSE ADVANCED RESEARCH PROJECTS AGENCY (DARPA)
1400 Wilson Boulevard
Arlington, VA 22209

Monitored by:
AFTAC/TGR
PATRICK AFB
FLORIDA 32925-6001

The views and conclusions contained in this document are those of the authors and should not be interpreted as representing the official policies, either expressed or implied, of the Defense Advanced Research Projects Agency or the United States Government.

87   6   24   065

REPORT DOCUMENTATION PAGE

1a. REPORT SECURITY CLASSIFICATION	1b. RESTRICTIVE MARKINGS
Unclassified	

2a. SECURITY CLASSIFICATION AUTHORITY	3. DISTRIBUTION/AVAILABILITY OF REPORT
	Approved for public release;
2b. DECLASSIFICATION/DOWNGRADING SCHEDULE	distribution is unlimited

4. PERFORMING ORGANIZATION REPORT NUMBER(S)	5. MONITORING ORGANIZATION REPORT NUMBER(S)

6a. NAME OF PERFORMING ORGANIZATION	6b. OFFICE SYMBOL (If applicable)	7a. NAME OF MONITORING ORGANIZATION
Rondout Associates, Inc.		AFTAC/TGR

6c. ADDRESS (City, State and ZIP Code)	7b. ADDRESS (City, State and ZIP Code)
P.O. Box 224 Stone Ridge, NY 12484	Patrick Air Force Base Florida 32925-6001

8a. NAME OF FUNDING/SPONSORING ORGANIZATION	8b. OFFICE SYMBOL (If applicable)	9. PROCUREMENT INSTRUMENT IDENTIFICATION NUMBER
DARPA	GSD	

8c. ADDRESS (City, State and ZIP Code)	10. SOURCE OF FUNDING NOS.			
	PROGRAM ELEMENT NO.	PROJECT NO.	TASK NO.	WORK UNIT NO.
1400 Wilson Boulevard Arlington, Virginia 22209	62714 E	DT/5126	A11	6A10

11. TITLE (Include Security Classification)
Source Depths Utilizing Broad Band Data

12. PERSONAL AUTHOR(S)
George H. Sutton, PI, Jerry A. Carter, Noel Barstow

13a. TYPE OF REPORT	13b. TIME COVERED	14. DATE OF REPORT (Yr., Mo., Day)	15. PAGE COUNT
Final Technical	FROM 11Apr85 TO 28Feb87	19 March 1987	109

16. SUPPLEMENTARY NOTATION

17. COSATI CODES			18. SUBJECT TERMS (Continue on reverse if necessary and identify by block number)
FIELD	GROUP	SUB. GR.	earthquake depths, depth phases, synthetic depth sections,
8	11		polarization processing, Kuril/Kamchatka, northeastern U.S.
17	10		

19. ABSTRACT (Continue on reverse if necessary and identify by block number)

This report covers the effort of a two year research project to improve our ability to discriminate between nuclear explosions and earthquakes based on the depth of an event determined from local and regional phases. The approach taken has been to improve phase identification and picking abilities for depth phases pP and sP through adaptive filtering to reduce effects of mode conversion and scattering. Three-component polarization methods are applied to broad-band digital data from a set of earthquakes located in the northeastern United States and from the short period records of the Ocean Sub-bottom Seismometer (OSS) for events in the Kuril/Kamchatka area. Data from the northeast U.S. are compared with suites of synthetic seismograms for different depths and focal mechanisms obtained using two velocity/ attenuation models appropriate for northeastern United States and Canada. This comparison provides a basis for identification of the depth phases and discrimination of other reflected/ refracted arrivals in the P wavetrain. Polarization state filtering (following procedures proposed by Samson) is used to emphasize those frequencies exhibiting the desired particle motion within a time window that slides through the P wavetrain. Adaptive orientation of the

20. DISTRIBUTION/AVAILABILITY OF ABSTRACT	21. ABSTRACT SECURITY CLASSIFICATION
UNCLASSIFIED/UNLIMITED ☒ SAME AS RPT. ☐ DTIC USERS ☐	Unclassified

22a. NAME OF RESPONSIBLE INDIVIDUAL	22b. TELEPHONE NUMBER (Include Area Code)	22c. OFFICE SYMBOL
Dr. Dean A. Clauter	305-494-5263	AFTAC/TGR

DD FORM 1473, 83 APR EDITION OF 1 JAN 73 IS OBSOLETE.

19. (continued)

state filtered data into radial and transverse horizontal components and determination of
azimuths and apparent angles of incidence further facilitate phase identification and
comparison with synthetics. Eight local and regional earthquakes and one quarry blast in the
northeastern U.S. were selected for study in the first phase of the project. It was found
that depths could be determined fairly reliably but that complicated source time functions
can lead to misidentification of the depth phases and consequently incorrect depth estimates.
Fortunately, complicated source functions should occur only for earthquakes and not ex-
plosions. The second phase of the project applied the methods developed using the well
constrained events of the northeastern U.S. to the OSS data. Polarization filtering reduced
much of the P coda and emphasized discrete portions of the wavetrain as anticipated. However,
the unique location of the OSS, well below the sea bottom, presented problems. The sea-bottom
reflection added downgoing waves to the usual upgoing wave field and inhibited the use of the
angle of incidence as a method of identifying phases. In addition, the sea-surface reflection
at 7.7 seconds effectively masked depth phase arrivals for events deeper than about 23 km.
The depths obtained for the Kuril/Kamchatka events were poor matches to the published depths.

Accession For

NTIS GRA&I ☑
DTIC TAB ☐
Unannounced ☐
Justification

By
Distribution/
Availability Codes
Dist | Avail and/or Special
A-1

TABLE OF CONTENTS

SECTION   PAGE

LIST OF FIGURES

LIST OF TABLES

(THIS PAGE INTENTIONALLY LEFT BLANK)

SECTION I

INTRODUCTION

The purpose of the research presented in this document is to refine our ability to discriminate between nuclear explosions and earthquakes based on the depth of an event determined from local and regional phases. If the depths of seismic events can be determined accurately, many events can be eliminated as potential nuclear explosions based on the practical limit of nuclear explosion burial depth. This discriminant has been used for many years at teleseismic distances. The higher frequency data obtained at local and regional distances improves the depth resolution of the method and thus the minimum depth at which the discriminant may be applied. In addition, smaller events not recorded at teleseismic distances may be seen at regional and/or local distances.

Our approach to this problem has been to improve phase identification and picking abilities of depth phases pP and sP through filtering and three-component polarization methods. These methods are applied first to data from a set of earthquakes located in the northeastern United States and adjacent Canada. The area of study was chosen for several reasons:

(1) the large majority of events in this area occur at depths less than 15 km so that a data set of shallow events is readily available,

(2) the geology and tectonic setting of the area is well known and similar to that found in the Soviet Union,

(3) the depths of the events in the area of study are fairly well known from network studies and aftershock surveys, and

(4) there are two broad-band three-component digital seismic stations in the vicinity: RSNY and SRNY. RSNY, part of the Regional Seismic Test Network (RSTN), is in northern New York and SRNY, operated by Rondout Associates, is in southeastern New York.

Having refined the techniques for depth determination in the well known region of the northeastern U.S., the methods were applied to a set of data obtained from the Ocean Sub-bottom Seismometer (OSS) installed off the Kuril trench in the north Pacific Ocean. Several events from the Kamchatka peninsula and the Kuril Islands were studied.

The most difficult problem associated with depth determination at local and regional distances using depth phases is identification. As the depth phases are usually buried in the coda, data processing plays a key role in identifying and picking them. Band-pass filtering and three-component polarization state filtering methods are used on the data in an attempt to isolate the depth phases and adaptive polarization analysis is used to help identify them.

Once the depth phases have been correctly identified and picked, the depth can be determined accurately if the source region velocity structure is known. However,

misidentification of phases can lead to severe errors in the depth estimates. To assess the potential depth errors resulting from these problems, synthetic seismogram depth sections have been generated for each of the events in the northeastern U.S. to compare to the identification and time picks made from the data. Of course, the depth of the event is not the only factor contributing to the character of the depth section; the velocity-depth structure used and the focal mechanism are also very important to the overall character of the section.

In the sections that follow, we briefly describe the analysis methods used on the data to isolate depth phases, review the set of earthquakes that we have selected for study, and show detailed analyses of the earthquakes.

SECTION II

EVENT DEPTH DETERMINATION

In this report we describe a method of depth determination that involves enhancing the suspected depth phases at the beginning of the P coda using advanced polarization methods on three-component broad-band data. Single station techniques were emphasized as, in a realistic test ban monitoring situation, it is likely that only one station will record many of the suspect events. The particular techniques used to enhance the depth phases were adaptive polarization analysis, a method that adaptively rotates the horizontal components to the direction of maximum and minimum energy propagation, and polarization state filtering (Samson and Olsen, 1981), an adaptive frequency filtering technique that passes only those frequencies in a specified polarization state (e.g. rectilinear). These techniques successfully enhance polarized energy relative to the scattered component of the coda, which typically complicates the interpretation of local and regional seismograms. We note, however, that our research has concentrated primarily on events with signal-to-noise ratios of one or better, and studies on the effectiveness of the polarization state filter have shown that its effectiveness deteriorates below this level. Therefore, if depth phases are to be used to determine depth on very small magnitude events, then either better methods of enhancing the depth phases must be found or receiver sites must have low noise characteristics.

The next phase of the processing scheme is to identify the individual depth phases either through experience, synthetic seismogram comparison, or some other method. Because the depth phases all have the same phase velocity and polarization characteristics, identification of the phases cannot be made on these parameters alone. Additional information such as relative arrival times and amplitudes must be used. Whatever scheme is used to identify the arrivals, it is generally assumed that the source is a simple point mechanism within the frequency band being studied. For events at local and regional distances, this assumption is not always valid.

Polarization State Filtering

Polarization analysis of a three-component wavefield is used to determine the vector particle motion characteristics such as the degree of polarization, direction of propagation and ellipticity. This information can then be used to design filters that emphasize or eliminate waves having specific polarization properties. In seismology, this method has been applied to analyze and filter waves coming from certain directions, or having rectilinear or elliptical particle motion, and to discriminate against isotropic noise (Sutton and Pomeroy, 1963; White, 1964; Archambeau et al., 1965) .

Polarized arrivals can be enhanced, their wave type identified, and their direction of propagation, as well as their phase velocity for body waves and ellipticity for Rayleigh waves, determined. This information can then be used for phase identification, epicentral location, source depth determination, earth structure studies, ...etc. Data filtered for

polarized signal are more amenable to comparison with synthetic seismograms, providing a better determination of relevant parameters.

The polarization state method was proposed by Samson (1977) for the analysis and filtering of seismograms. It makes use of the spectral matrix, which is the frequency domain equivalent of the cross-correlation matrix of the data, smoothed over a frequency window. Various spectral estimators can be obtained from the spectral matrix, such as the degree of polarization, the degree of rectilinear polarization, a detector for signal in a specific "pure state" (i.e. completely polarized) or with specific polarization characteristics. Such estimators can then be used to filter the data in order to discriminate against unpolarized noise or to enhance signal in some specific polarization state (Samson and Olson, 1981). Since the polarization characteristics of seismograms continuously change with time, such filters have to be data-adaptive: a sliding time window of data is analyzed and a filter is specifically designed for that window. Polarization properties are determined and used not only as a function of time, but also as a function of frequency, since the processing is done in the frequency domain. This is an advantage that methods which operate purely in the time domain do not have.

To enhance depth phases pP and sP we take advantage of the three-component polarization state filter's ability to pass frequencies that contain rectilinearly polarized motion and reject frequencies that do not.

After the data have been state filtered for rectilinear motion, they are processed with an adaptive polarization method. The horizontal components are adaptively rotated to the time varying radial and transverse directions and the time variable azimuth and apparent angle of incidence are given. This process helps in the identification of phases. Also, the synthetic seismogram components are the radial and vertical so rotating the horizontal data to the adaptive radial and transverse components facilitates comparison.

Adaptive Polarization Analysis

In the Adaptive Polarization Analysis method developed at RAI, the horizontal components are adaptively rotated to the time varying radial and transverse directions and the time variable azimuth and apparent angle of incidence are given. This process helps in the identification of phases. Below we present the theory behind this method assuming rectilinear motion at a constant azimuth and angle of incidence. Later in the discussion, we will consider simultaneous arrivals from different directions.

We seek to determine the azimuth and angle of incidence over a small time window; one that is at least as long as one or two cycles of the predominant frequency. The azimuth is determined by examining the zero lag cross covariance between the two horizontal components as a function of azimuth angle. One of the angles at which this function is zero is the azimuth of the predominant particle motion. The horizontal components of motion as functions of the north (N) and east (E) horizontals and the azimuth (θ) are written:

$$H_1(t) = N(t)\cos\theta + E(t)\sin\theta$$
$$H_2(t) = E(t)\cos\theta - N(t)\sin\theta \tag{1}$$

and, the cross-covariance between H_1 and H_2 at zero lag is:

$$ccv_0 = \frac{1}{n}\sum_{i=0}^{n}\bar{H}_1(t+i\Delta t)\bar{H}_2(t+i\Delta t) \tag{2}$$

where $\bar{H}(t) = H(t) - \mu_H$, μ_H is the mean value of $H(t)$ over the interval, and Δt is the sampling interval. In terms of $\bar{N}$ and $\bar{E}$:

$$ccv_0(\theta) = a\cos 2\theta + b\sin 2\theta \tag{3}$$

where

$$a = \frac{1}{n}\sum_{i=0}^{n}\bar{N}(t + i\Delta t)\bar{E}(t + i\Delta t)$$

$$b = \frac{1}{n}\sum_{i=0}^{n}[\bar{E}^2(t + i\Delta t) - \bar{N}^2(t + i\Delta t)]/2$$

Solving for θ at $ccv_0\theta = 0$:

$$\theta = \tan^{-1}(-a/b)/2 \tag{4}$$

    The azimuth θ obtained from (4) will be between -45° and 45° and could represent any one of four directions; the direction of particle motion, its supplement, its transverse, or the transverse supplement. Without using the vertical component, the direction obtained from (4) can be determined with a 180° ambiguity by examining the behavior of (3). The zero lag cross-covariance as a function of azimuth given by (3) is a sinusoid. Suppose that the θ determined from (4) aligns the H_2 component with the direction of maximum particle motion. Increasing this θ in (3) will place the direction of particle motion between the H_1 and H_2 components and the value of ccv_0 will increase. Conversely, if H_1 is aligned with the direction of particle motion by (4) then increasing θ in (3) will decrease ccv_0. Thus, when the slope of the sinusoid given by (3) at the azimuth determined in (4) is positive, then θ is transverse to the direction of particle motion (or its supplement) and when the slope of the sinusoid given by (3) at the azimuth determined in (4) is negative, then θ is the direction of particle motion (or its supplement). Rather than computing the slope from the derivative of (3) with respect to θ, we can find its sign by examining (3) at $\theta = 0$ where $ccv_0(0) = a$. If the signs of a and the θ found from (4) are similar (i.e. both have the same sign), then the slope is negative and θ is the direction of particle motion or its supplement. If the signs are dissimilar, then the slope is positive and the direction of particle motion is at either $\theta + 90°$ or $\theta - 90°$. The direction of particle motion can be either longitudinal or transverse to the propagation direction depending on whether the particle motion is *P/SV* or *SH*. If the azimuth from the event to the station is known, then particle motion between ± 45° of that azimuth

can be considered radial and between 45° and 135° or −45° and −135° can be considered transverse. The azimuth obtained from (4) together with the assumed azimuth to the event can be used to rotate the horizontal components to the radial and transverse directions at the center of the window. The window is then advanced one sample and the process repeated. The radial and transverse traces separate the $P/SV/$Rayleigh motion from the $SH/$Love motion.

The apparent angle of incidence is calculated in much the same manner as the azimuth. For this measurement, the adapted radial and vertical components are used as the orthogonal components from which the angle of incidence is determined. The distinctive particle motions of P, SV, and Rayleigh waves are distinguished using the apparent angle of incidence. P motion gives a positive value, SV a negative one and Rayleigh a rotating angle of incidence.

An estimate of the relative accuracy of the azimuth and angle of incidence measurements is obtained through the maximum value of the zero lag cross-correlation function. At its maximum value, where the predominant direction of motion bisects H_1 and H_2, the zero lag cross-correlation function $(\mathrm{ccf}_0(\theta + 45°))$ will be between 0 and 1, inclusive. A large value is indicative of strong rectilinear motion over the window and a small value indicates the lack thereof. Where there is little or no rectilinear motion, confidence in the results obtained is also small and we expect the error to be close to 90°. Conversely, a large value for $\mathrm{ccf}_0(\theta + 45°)$ indicates strong rectilinear motion and should have an error close to 0°. This subjective error evaluation can be written:

$$\text{error} = 90° \left(1 - \mathrm{ccf}_0(\theta + 45°)\right). \tag{5}$$

Error determined in this manner is not an absolute quantity but rather a relative measure of the accuracy of the value.

Because the method presented here relies on the determination of the predominant direction of motion, the question arises; "What angle would be determined if two uncorrelated signals arrived at the station at the same time from different directions?". Let the two uncorrelated signals be $x(t)$ and $y(t)$ where the standard deviations of x and y are equal and define the north and east components of motion as

$$\begin{aligned} N(t) &= jx(t) + ky(t) \\ E(t) &= rx(t) + sy(t) \end{aligned} \tag{6}$$

j, k, r, and s are scaling factors that can be set to simulate any combination of direction and amplitude for x and y. Substituting the values for N and E in (6) into equation (4)

$$\theta = \frac{1}{2}\tan^{-1}\left\{\frac{\sum[(jx + ky)(rx + sy)]}{\sum[(r^2x^2 + s^2y^2 + 2rsxy - j^2x^2 - k^2y^2 - 2jkxy)]/2}\right\} \qquad (7)$$

Because x and y are not correlated, the xy terms tend to zero as the length of the series gets large. Rewriting (7) eliminating these terms

$$\theta = \frac{1}{2}\tan^{-1}\left\{\frac{\sum 2(rjx^2 + ksy^2)}{\sum[(j^2 - r^2)x^2 + (k^2 - s^2)y^2]}\right\} \qquad (8)$$

Equation (8) may be used to predict θ for two time series passing a station at different azimuths. The worst case occurs when the two wavetrains are traveling at azimuths 45° apart, for when one of the signals is showing no correlation at its azimuth, the other will be at a maximum. If the two signals are orthogonal, then the proper azimuth would be chosen.

The above analysis is valid only in the case that the two signals are not coherent. When the two signals are perfectly coherent then the azimuth determined will be that of the vector sum of the two signals. Partial coherency would result in some combination of the completely non-coherent result and the perfectly coherent result.

In Figure 1, we show synthetic vertical and horizontal components to be used as the input to the polarization program. The modulated arrivals on the horizontal components represent a constant amplitude signal that rotates smoothly in azimuth. A constant amplitude vertical component maintains an unchanging angle of incidence. The results of processing this data with the polarization program, assuming that the signal contains longitudinal motion exclusively, are shown in Figure 2A. There are six output traces; the vertical, adapted radial, and adapted transverse components of motion, the product of the radial and vertical traces, and the azimuth and apparent angle of incidence traces plotted with error bars. The radial trace exhibits a constant amplitude and the transverse component shows very little motion at all. Thus, the radial follows the predominant direction of motion. In the case of a short duration arrival, the RZ trace would help to identify the first arrival and its direction but in this case, where the signal is continuous, RZ has little use. The azimuth trace tracks the motion of the rotating arrival quite well and shows very little error. The same is true of the apparent angle of incidence trace where there is no change throughout the duration of the analysis. When a propagation direction is assumed in the polarization program (Figure 2b), the particle motion jumps between the radial and transverse components as the azimuth rotates from one direction to the other. The RZ and apparent angle of incidence traces help to identify the type of motion. When positive, the motion is P type; when negative, SV; and when zero, SH. Rayleigh waves produce a rotation in the RZ and angle of
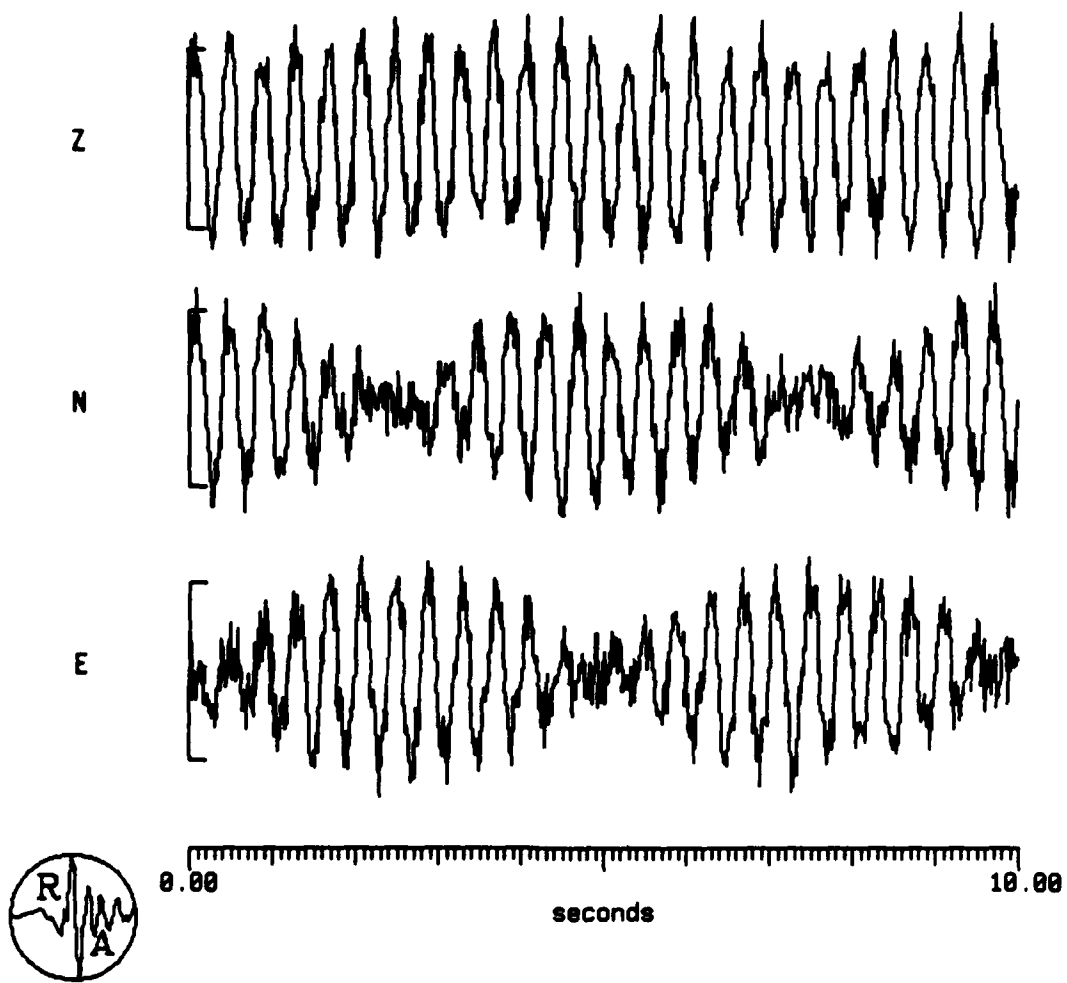
Figure 1. Vertical, North-South, and East-West components of motion for a signal sweeping 360° of azimuth plus noise.
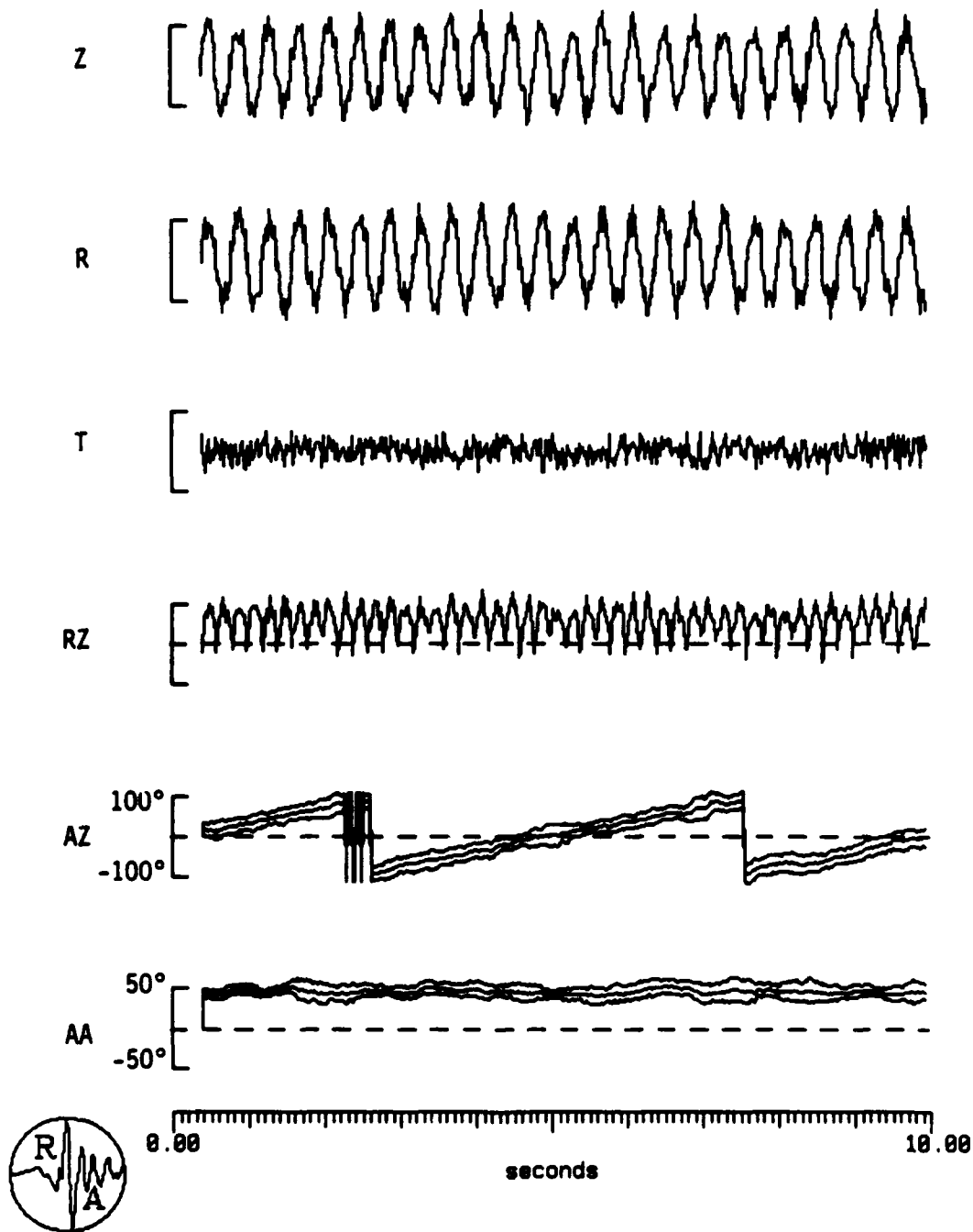
Figure 2A. Adaptive polarization analysis of the data in Figure 1 assuming no azimuth. Z=vertical; R=radial; T=transverse; RZ=sign (RZ) $\sqrt{RZ}$; AZ=azimuth with relative error bars; AA=angle of incidence with error bars. The radial trace tracks the direction of particle motion around the circle.

9
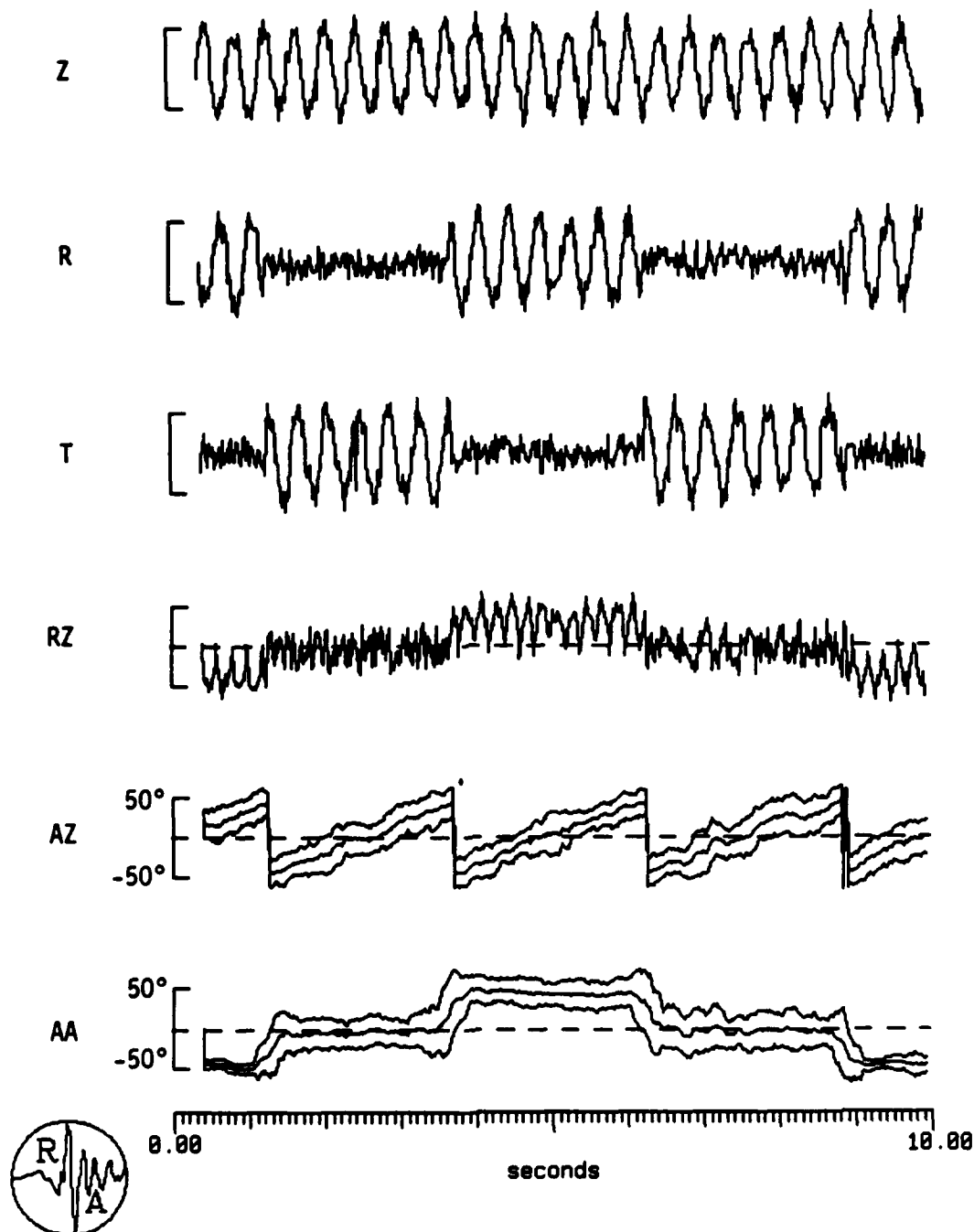
Figure 2B. Same as Figure 2A. but assuming an azimuth of 0°. The motion changes from radial to transverse and back as the azimuth moves around the circle. Positive values of RZ and AA indicate *P* type motion; zero values indicate *SH* motion; and negative values, *SV* motion.

10

incidence traces. Note that the azimuth trace jumps from +45° to −45° as the assumed phase changes from SV to SH to P etc. This occurs because the propagation azimuth for SH motion is set to be + or − 90° from the particle motion.

For the second example, two independent samples of random noise were combined on the N, E and Z components of motion to simulate one set of arrivals traveling at 0° azimuth, 72° angle of incidence with an amplitude of 1000 and another set of arrivals traveling N45°E, 55° angle of incidence and amplitude 548 (amplitudes are relative). In terms of the independent non-coherent time series $x(t)$ and $y(t)$:

$$N(t) = 3.0x(t) + y(t)$$

$$E(t) = y(t) \tag{9}$$

$$Z(t) = x(t) + y(t)$$

Using these numbers in equation (8), we obtain values of 6° for the azimuth and 67° for the angle of incidence (assuming an azimuth of 6° for the radial trace). The results of the polarization analysis are shown in Figure 3. The azimuth trace is centered about 6° over the length of the trace in excellent agreement with the theory. Error for the azimuth is large and is due to the fact that the two arrival sets are traveling at azimuths 45° apart; the worst possible case. For the apparent angle of incidence, the measured value of 67° is also in excellent agreement with theory and in this case the error is very small. The small error arises because the two arrival groups are traveling at a similar angle of incidence in the vertical plane at 6° azimuth.

The adaptive polarization analysis program is a useful tool for locating earthquakes when only a single three-component data set is available. The azimuth from the initial P-wave, where presumably the error will be smallest and no conflicting arrivals are present, combined with the distance obtained from the S-P time gives a fairly accurate location.

Synthetic Seismograms

The synthetic seismograms were computed using the locked mode method (Harvey, 1981) at frequencies from 0 to 5 Hz. Regional geology in the Northeast required that two different velocity/attenuation models be used for the computation; a New England model for the events in New England and southern New York, and a Grenville model for events within the Grenville province (Figure 4, Table 1). The New England velocity model was derived by Taylor et al., (1980) using regional travel times of P and S waves recorded across the Northeastern United States Seismic Network operated by several academic, governmental and private institutions in the northeast. The Grenville model was from unpublished refraction results. The frequency and depth dependent Q model for the New England model was adapted from work by Mitchell (1981) and a simple frequency dependent Q was used for the Grenville model. Although there are significant differences in the Q models, there is little effect on the synthetics because the frequencies and ranges at which they are being computed are relatively small.
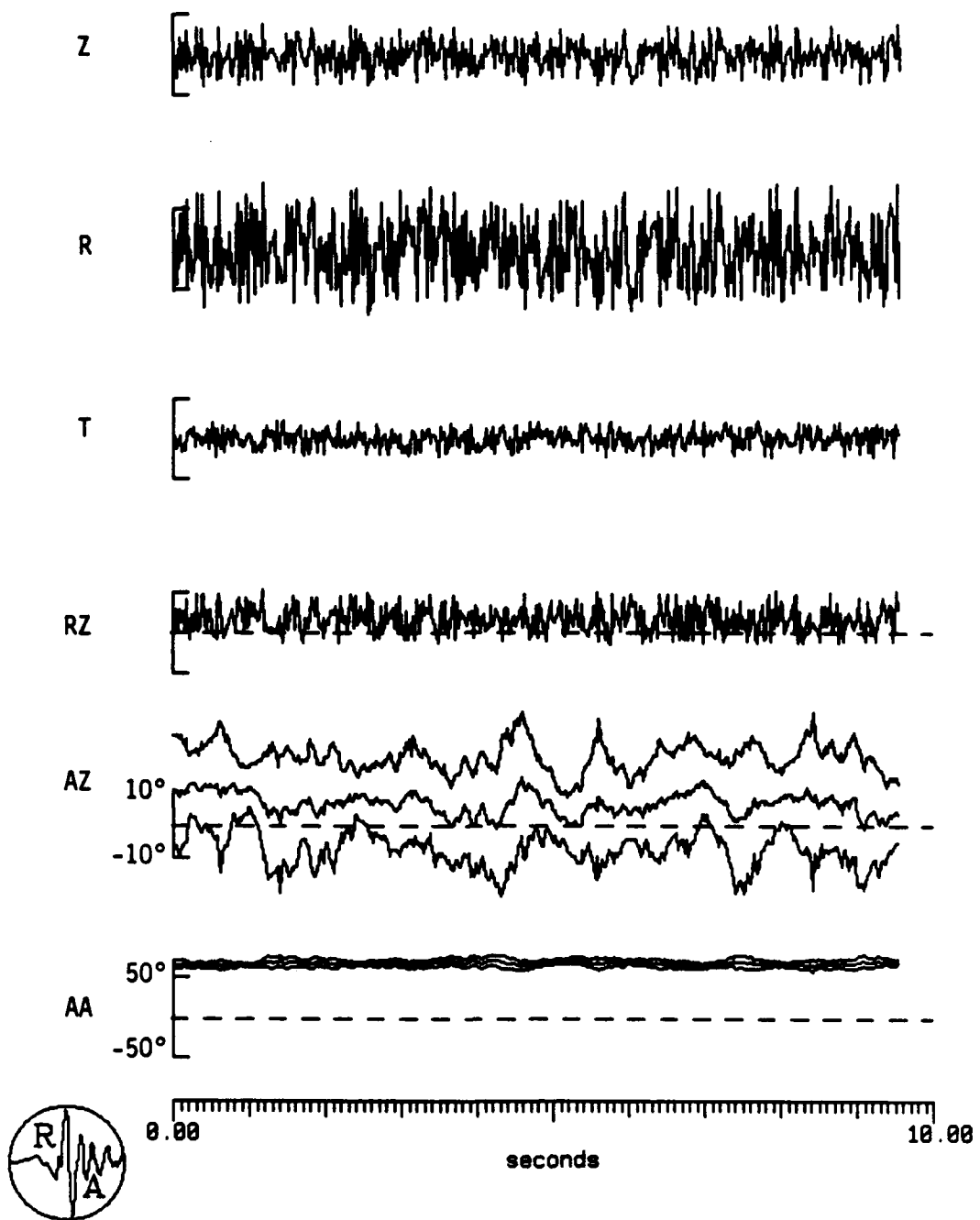
Figure 3. Results of trying to track two different sets of random noise traveling in different directions. One set is traveling to the northeast; the other is traveling due north and is almost twice the amplitude of the first.
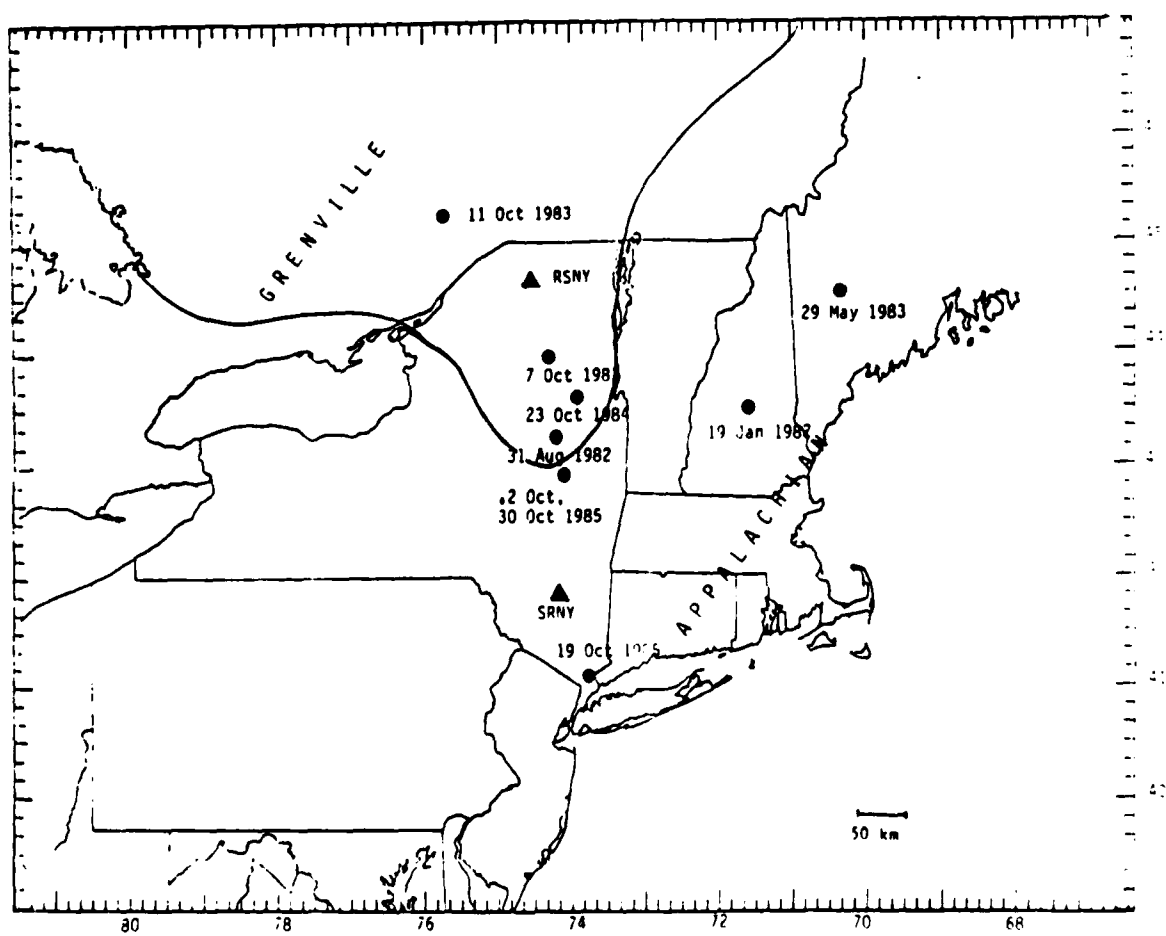
Figure 4. Location of northeastern events and stations used in this study. Events are indicated by circles and a date. The two stations, RSNY and SRNY are indicated by triangles.

13

Synthetics were computed for each event at several depths with the reported focal mechanism listed in Table 2. The instrument response was convolved with the synthetics for comparison to the data.

Station RSNY lies within the Grenville structure close to the boundary with the New England Structure. While the travel paths to RSNY from New England events must pass through both structures, the majority of the path is within the New England structure and so the New England structure is a good approximation to the true path.

Throughout this report, only the first 20 or so seconds of the synthetic depth sections are shown as we wish to emphasize the characteristics of the depth phases with focal mechanism, depth, range, and velocity model. Some of the phases are identified in the synthetic sections with labeled lines. Reflections off of the 13 km discontinuity in the New England model and the 4 km discontinuity in the Grenville model are indicated with an i (e.g. PiP). Mantle reflections are indicated by an m. The depth phases are characterized by progressively later arrivals with increased depth and the primary phases by either very little change in arrival time with depth for the direct arrivals or progressively earlier arrivals with increased depth. In some of the sections, the depth phases dominate, while in others, the primary phases dominate. This is a function of the theoretical radiation pattern predicted by the input focal mechanism. Because the input velocity structure will influence the take-off angle of each phase and hence its position on the focal sphere, both focal mechanism and velocity model contribute to the relative amplitudes of primary and depth phases.

TABLE 1					
New England Velocity/Q Model (Taylor *et al.*, 1980)					
Thickness (km)	V_P (km/sec)	V_s (km/sec)	ρ (gm/cm^3)	Q_α	Q_β
2 13 25	6.0 6.1 7.0 8.1	3.5 3.6 4.1 4.7	2.5 2.6 2.9 3.2	$9Q_\beta/5$	$250f^{0.2}$ $500f^{0.2}$ $1000f^{0.2}$ $3000f^{0.2}$
Grenville Velocity/Q Model					
Thickness (km)	V_p (km/sec)	V_s (km/sec)	ρ (gm/cm^3)	Q_α	Q_β
4 31	6.1 6.6 8.1	3.5 3.7 4.6	2.5 2.7 3.2	$1100+150\,f$	$5Q_\alpha/9$

The success of determining focal depth using depth phases and comparing them to synthetics depends largely on:

(1) good approximations of crustal velocity structure, and

(2) recovery and correct identification of the phases in the data.

Here we use one earthquake to illustrate how the synthetic seismograms are affected by 2 different velocity models and focal mechanisms.

The earthquake chosen is the Gaza, N.H., magnitude 4.5 event of January 19, 1982. Since the source is in the Appalachian Province and the receiver (RSNY) is in the Grenville Province (see Figure 4) we calculated separate synthetics using the two velocity models (Table 1) to test which is more appropriate.

Figure 5 shows radial and vertical components for the initial 15 seconds of the synthetic seismograms calculated for two velocity models. RSNY is the theoretical receiver, a distance of 267 km and an azimuth of 295° from the New Hampshire source. The velocity models and Moho reflections are shown schematically for comparison. The focal mechanism is given by: strike = 280°, dip = 75° and rake = -11°. The input focal depths are comparable.

As expected, the prominent phases and their arrival times are different for the two different velocity models. The Pn phase is nodal for the radiation pattern, despite small differences in take-off angles for the two models. It is simply indicated at the appropriate arrival time. For the New England model, PmP is small relative to $sPmP$. They both arrive before the intra-crustal reflections PiP and $sPiP$. For depths greater than 10 km, however, PiP arrives before $sPmP$. PiP and $sPiP$ are sharp arrivals because of the large velocity contrast at 15 km in the crustal model. V_p increases from 6.1 km/sec to 7.0 km/sec at this boundary.

For the Grenville model, Pg precedes the Moho reflections (for a source depth of 7 km). The amplitude of $sPmP$ relative to PmP is smaller for the Grenville model than for the New England model because the upgoing $sPmP$ is crossing a fairly sharp internal discontinuity near the source while the downgoing PmP only crosses this boundary once, near the receiver. In the case of New England structure, the sharp discontinuity is below the source, instead of above it. In addition, PmP is close to a nodal plane and small differences in take-off angle, resulting from differences in the velocity structures, may be contributing to the difference in the amplitudes of PmP.

Even though the two velocity models produce strikingly different synthetic seismograms, it is important to note that for the depths and models shown, the time between the arrivals of the downgoing and upgoing Moho reflections is the same. Thus, if one can independently identify these two phases in the actual data, a match (ignoring absolute travel times) to the Grenville synthetic would suggest a depth of 7 km and a match to the New England synthetic would suggest a depth of 6 km. Given this time difference between the two arrivals, the choice of velocity model has had only a small effect on depth determination. If, however, one uses the computed phase travel times to help identify depth phases in the real data, the variation in travel time with velocity model could lead to misinterpretations of the real data.

Next, in Figure 6 we show 15 seconds of synthetics calculated for 2 different focal mechanisms. The mechanism shown at the bottom was determined from P-wave first motion data, mainly from the Northeast United States Seismic Network (Pulli *et al.*,

1983). The mechanism at the top of the figure differs mainly in the quadrants of dilatation and compression. The azimuth to station RSNY is very close to a nodal plane in both instances, so there is not a great difference in radiation pattern. Thus, the same initial phases appear on both sets of seismograms, but the amplitudes of these phases are different. If theoretical radiation patterns can be used to predict actual phases in the data, then it will be helpful to have independently determined fault plane solutions.

New England Model

Grenville Model
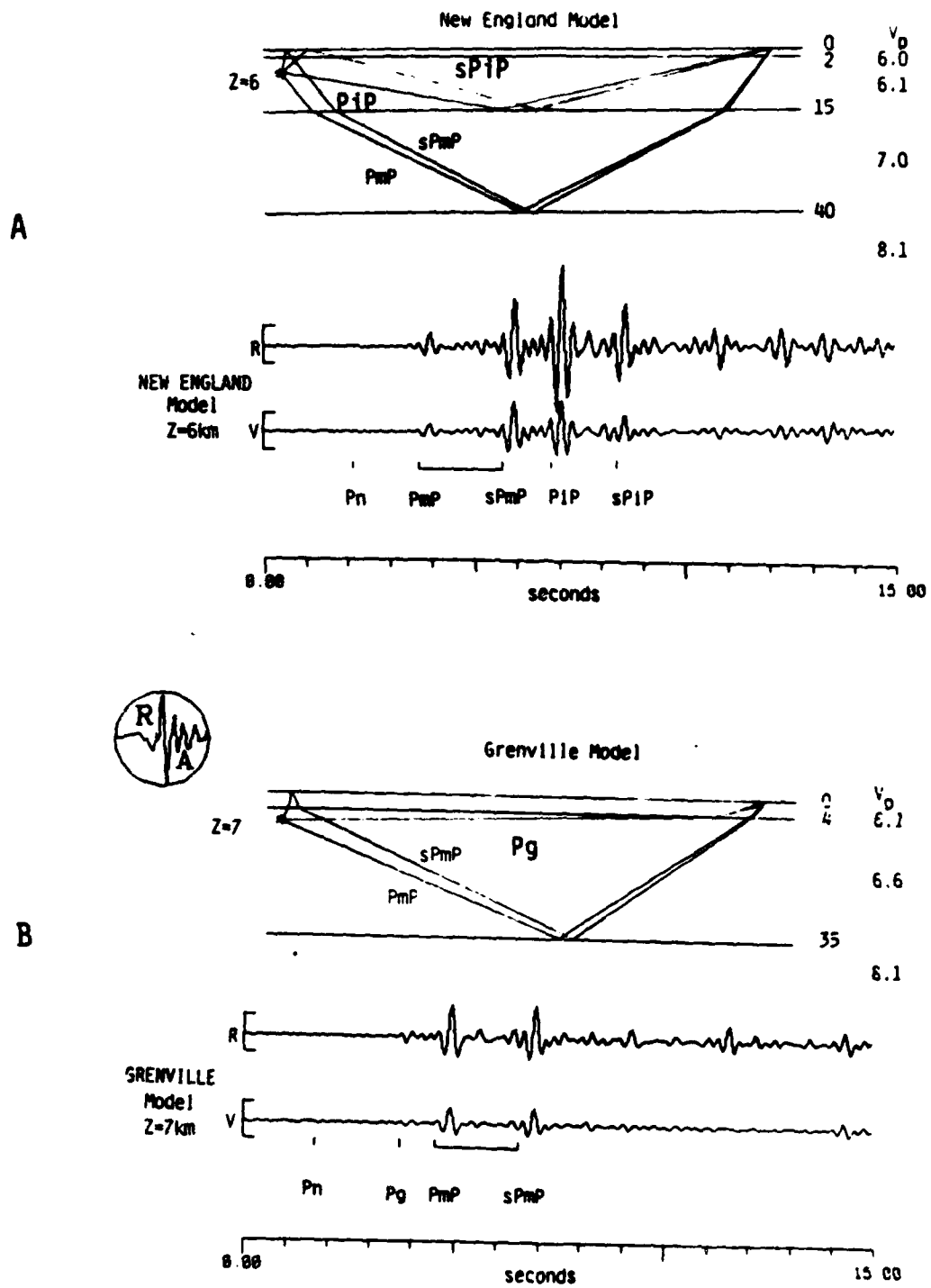
January 19, 1982, Δ= 267 Km, Azimuth= 295.

Figure 5. Two velocity models and resulting synthetic seismograms.
A) New England Model, source depth=6 km. Source-to-receiver Moho, reflections shown schematically. 15 seconds of radial and vertical component synthetics, with phases identified. *PiP* and *sPiP* are internal reflections at the 15 km boundary.
B) Grenville model, source depth=7 km. Source-to-receiver Moho, reflections shown schematically. 15 seconds of radial and vertical component synthetics with phases identified.
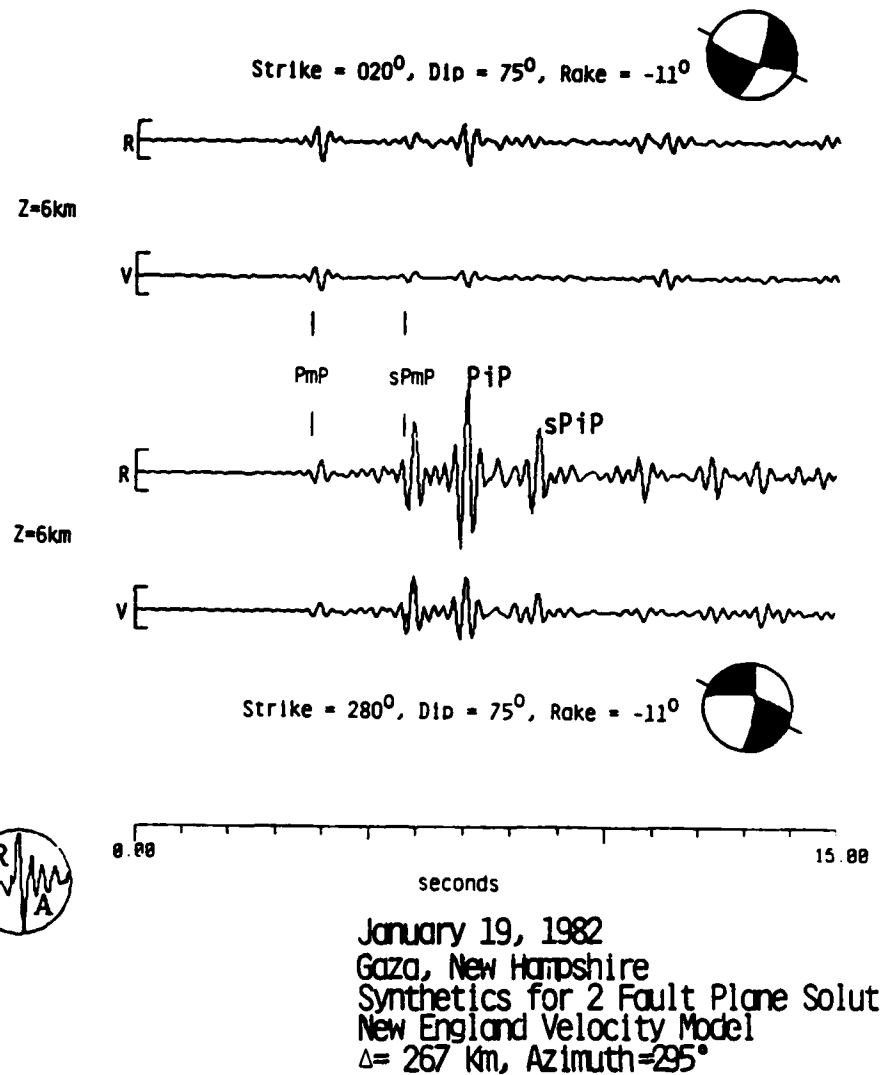
Figure 6. Two fault plane solutions and resulting synthetic seismograms. Fifteen seconds of the radial and vertical components are shown for each of the two different input solutions. The azimuth to RSNY is indicated by a line on the fault plane solution, a lower hemisphere projection with compressional quadrants filled in.

18

SECTION III

DATA

In the northeastern United States and Ontario, Canada, eight local and regional earthquakes and one quarry blast were selected for study. The events were chosen for their size, location, and availability of data. A list of these events is given in Table 2 along with location, depth, magnitude, strike, dip, and rake of the focal mechanism, the region (either New England or Grenville), and references for the focal parameters. The event and station locations are plotted in Figure 4, showing their spatial distribution. Many of the earthquakes in Table 2 have been studied by others and, for some, the focal depths and focal mechanisms are well determined and will provide an excellent base for comparison.

In addition to reviewing the literature, we examined phase data from local seismic networks originally used to invert for hypocentral location. In three cases the estimated error on focal depth was so large that to use the reported depth would be misleading. For these we indicate (Table 2) an unknown depth.

Most of the data were recorded by RSNY, in northern New York, at 44.55 ° N, 74.53 ° W. Several of the recent events were also recorded by SRNY, a very-broad-band seismic station operated by Rondout Associates in Stone Ridge, New York, at 41.85 ° N, 74.15 ° W.

Data for the Kuril/Kamchatka portion of this study were recorded by the fourth Ocean Sub-bottom Seismometer (OSS-IV) emplaced 380 m below the sea floor at the bottom of DSDP hole 581C (44 ° N, 160 ° E). The data spanned the period from September 12 to November 16, 1982 and the events selected for study are listed in Table 3. The closest event to OSS-IV in 574 km away and the furthest 1307 km. The large distances make the computation of synthetic seismograms using the locked mode method unreasonable.

Crosstalk and skew problems hamper analyses of the OSS-IV data. The skew was easily corrected but the amount of crosstalk is difficult to judge. Theoretically the crosstalk problem effects only the azimuth and apparent angle of incidence determinations and not the isolation of the depth phases needed for depth determination. Relative amplitudes of the phases may not be correct, but the polarization state filter does not preserve absolute amplitudes anyway, so the point is unimportant; it is only mentioned here for the sake of completeness.

A map of the event locations in Table 3 and OSS-IV is given in Figure 7. The events were classified as being either excellent, good or bad for depth determination based on the signal-to-noise ratio and impulsiveness of the records. Recordings that were emergent and unlikely to show clear depth phases without a great deal of processing were classified as bad. The excellent (*) and good (x) data seem to be associated with the downgoing Pacific plate and the bad (o) data with the shallow events within the accretionary wedge of the Kamchatka peninsula. The number of events studied is too small

Table 2

LIST OF EVENTS AND EVENT PARAMETERS

Date	Time	Lat	Lon	Depth(km)	M	Strike	Dip	Rake	Reg	Refs
Jan 19, 1982	00:14:42.00	43.49	-71.59	3 - 11	4.5 M_b	280	75	-11	NE	1,2,3,4
Aug 31, 1982	10:16:58.10	43.21	-74.20	?	2.6 M_n	173	60	110*	G	1,5
May 29, 1983	05:45:49.80	44.50	-70.41	2	4.2 M_b	355	52	78	NE	1,6
Oct 07, 1983	10:18:46.10	43.94	-74.26	7-12	5.2 M_b	173	60	110	G	1,5,7,8,9
Oct 11, 1983	04:10:55.00	45.21	-75.77	12	4.1 M_{bLg}	071	75	98	G	1,10
Oct 23, 1984	06:26:21.71	43.59	-73.94	?	3.4 M_c	353	60	17*	G	1,5
Oct 02, 1985	21:10	42.90	-74.14	0	2.3 M_c	Chem	Ex		App(NE)	
Oct 19, 1985	10:07:40.30	40.98	-73.83	5	4.0 M_L	022	90	180	App(NE)	1,11
Oct 30, 1985	03:42:49.68	42.93	-74.11	<10	2.7 M_c	018	60	156**	App(NE)	5,12

* Generic Adirondack Fault Plane Solution (from 7)
** Generic Mid-Hudson Fault Plane Solution (from 12)

References:
1. Preliminary Determination of Epicenters
2. Pulli et al., 1983
3. Brown and Ebel, 1985
4. Barstow et al., 1986
5. Regional Seismicity Bulletin of Lamont-Doherty Seismic Network
6. Ebel and McCaffrey, 1984
7. Suarez et al., 1984
8. Seeber et al., 1984a
9. Seeber et al., 1984b
10. Wahlstrom, 1983
11. Seeber et al., 1986
12. Houlday et al., 1984
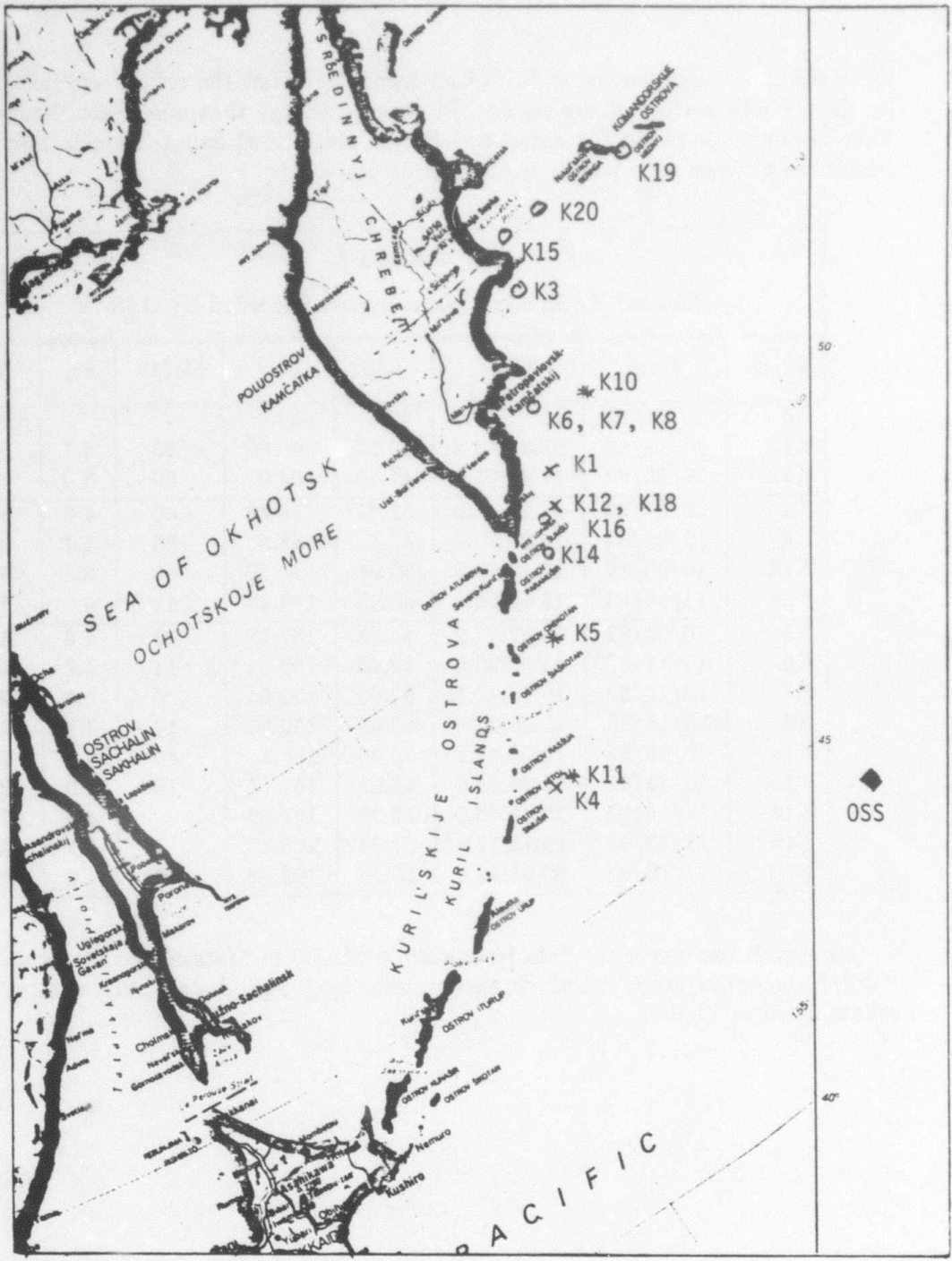
Figure 7. Location of OSS-IV and the Kuril/Kamchatka events used in this study. * = excellent events, x = good events, o = bad events.

to attach much significance to this observation; however, the results are easily explained by the tectonic setting of the region. In general, energy that must pass through the tectonic boundary between the Asian and Pacific plates is attenuated much more than that which has a travel path wholly in the Pacific plate.

TABLE 3							
Selected Kuril/Kamchatka Events Recorded By OSS-IV							
Event	Date	Time	Lat	Lon	Depth	m_b	Δ
K5	10/05/82	11:04:57.0	49.3	155.9	-	-	668
K10	10/11/82	22:27:43.2	52.15	160.89	23	4.7	918
K11	10/23/82	11:41:01.0	47.10	154.0	30	5.0	574
K1	09/21/82	21:29:44.9	51.63	158.68	40	4.8	861
K4	10/03/82	14:05:39.0	47.1	153.5	120	4.7	605
K12	10/23/82	23:19:25.5	50.98	158.10	40	4.6	795
K13	11/15/82	18:53:06.8	50.93	158.18	42	4.5	788
K3	10/03/82	00:32:57.2	54.28	161.37	33	4.8	1157
K6	10/11/82	15:31:26.9	52.45	159.61	14	4.7	948
K7	10/11/82	15:33:22.5	52.46	159.55	6	4.8	949
K8	10/11/82	15:35:22.6	52.43	159.66	14	4.7	946
K14	10/25/82	12:05:47.3	50.46	157.2	40	4.7	753
K15	10/25/82	15:38:58.6	55.15	162.18	10	4.8	1260
K16	11/13/82	19:58:46.0	50.95	157.69	-	4.7	797
K19	11/15/82	19:18:17.1	54.84	166.52	4	5.1	1307
K20	11/16/82	00:51:12.6	55.25	163.76	6	4.6	1291

A search was made for data from station MAJO in Matsushiro, Japan to aid in the Kuril/Kamchatka study. Unfortunately, only long period data was available for the events listed in Table 3.

SECTION IV.

DATA ANALYSIS

In this section we show how we estimate source depths of the earthquakes presented in the previous section. First, the northeast North American events are compared to synthetic seismogram depth sections and a best-fit depth is selected. This is followed by a brief presentation of the Kuril/Kamchatka OSS data, which turns out to be ill-suited for depth determination.

New Hampshire, January 19, 1982

It would be very difficult to compare the raw data recorded at RSNY to the synthetic seismograms (compare the top of Figure 8 with the synthetics in Figure 9). With the polarization filtering, however, we have been able to recover polarized phases (bottom of Figure 8) that were all but lost in the P-coda of the unfiltered seismograms. After polarization filtering, we low-pass filter the data to remove frequencies greater than 5 Hz, which are not modeled by the synthetics.

The following figures show comparisons of the vertical-component RSNY processed data to the vertical-component synthetic depth section calculated for the New England model. Twenty seconds are shown. We began by inserting the data at a depth of about 9 km (Figure 10). There are several arrivals in the data that match predicted arrivals. These are, in order, PmP, $sPmP$, the dual arrivals PiP and Pg, and finally an upgoing phase arriving toward the end of this time window. Clearly, the match is not perfect. Signal arrives in the data later than the appropriate time for $sPiP$, and, subsequently, until the late phase (in the data, about 14 seconds after the initial P), there is not a good correlation between data and synthetics. A comparison of travel times for the first arriving phase in the data and synthetics suggests that they may not be the same phase. The travel time of synthetic PmP at a source depth of 9 km (with the given input velocity model) is 40.40 seconds, whereas the travel time of the first phase in the data is 38.59 seconds. Allowing for uncertainties in the actual origin time of the earthquake and for uncertainties in crustal structure, they could be the same phase. If, however, we assume that the origin time and velocity model are appropriate, we can match several early P-phases by aligning the data at a depth of approximately 4.5 km as illustrated in Figure 11. Since the real-data travel time is more appropriate for Pn, the first arrival is now aligned with the predicted Pn arrival time (compare Figures 10 and 11). For this shallower depth, the data conform to predicted arrival times for Pn, PmP, $sPmP$ and for the late up-going phase. Again, the correlation among all phases, real and synthetic, is not perfect.

At this point, it is clear that a great deal depends on the correct identification of the arrivals in the data. In addition to travel times, the azimuth and apparent angles of incidence can be used to help identify phases. In Figure 12 we show the results of an
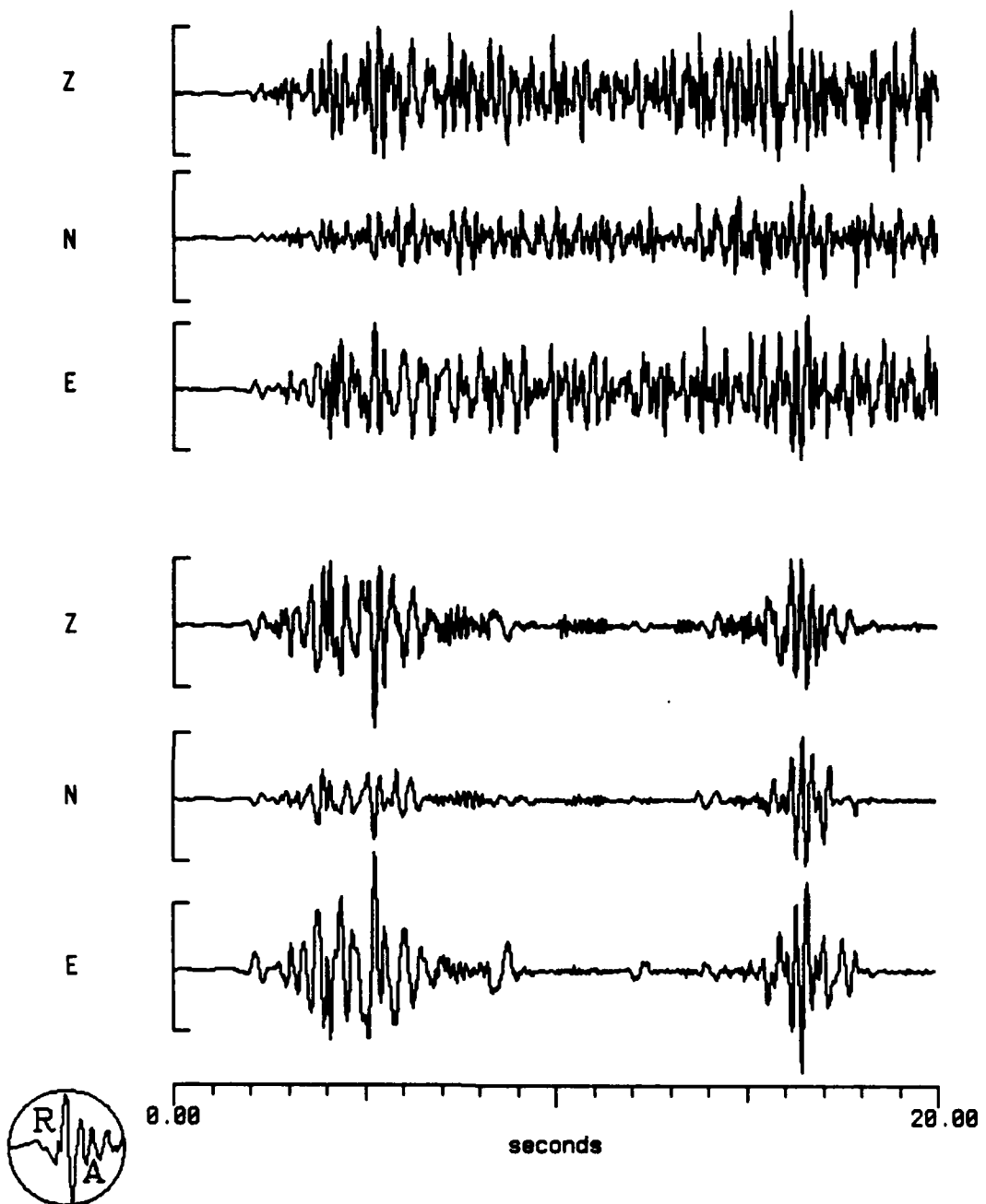
Figure 8. Seismograms recorded at RSNY of the January 19, 1982, New Hampshire earthquake, Δ=267 km. The top three traces are the vertical, north-south, and east-west components, unfiltered. The bottom three traces are the three components after state-filtering for rectilinear particle motion.
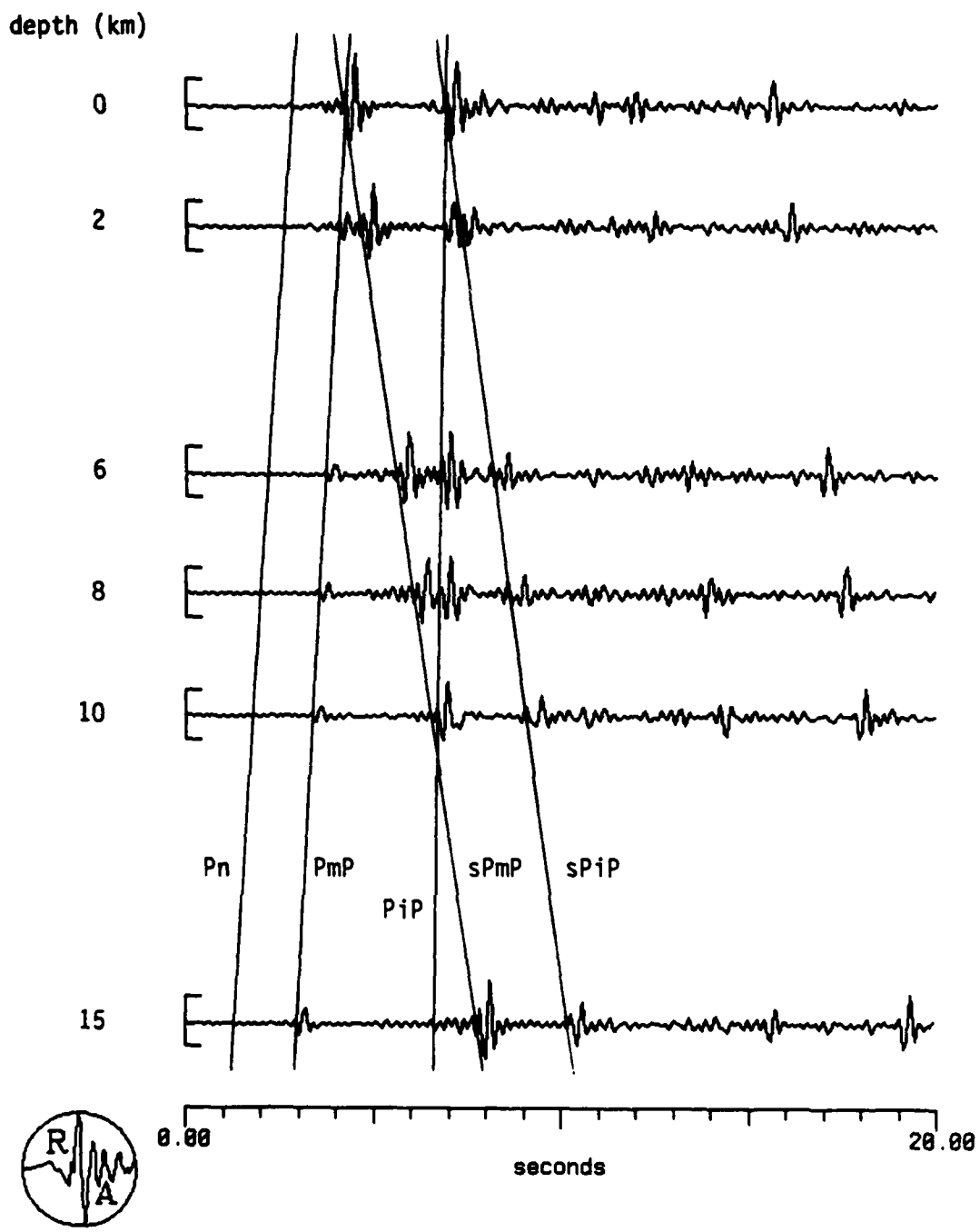
Figure 9. Synthetic seismograms calculated for a suite of depths. Source=January 19, 1982, earthquake. Strike=280, Dip=75, Rake=−11. Receiver response=RSNY short period (sp). Azimuth=295. *PiP* is reflected within the crust, and *PmP* is reflected at the Moho.

25
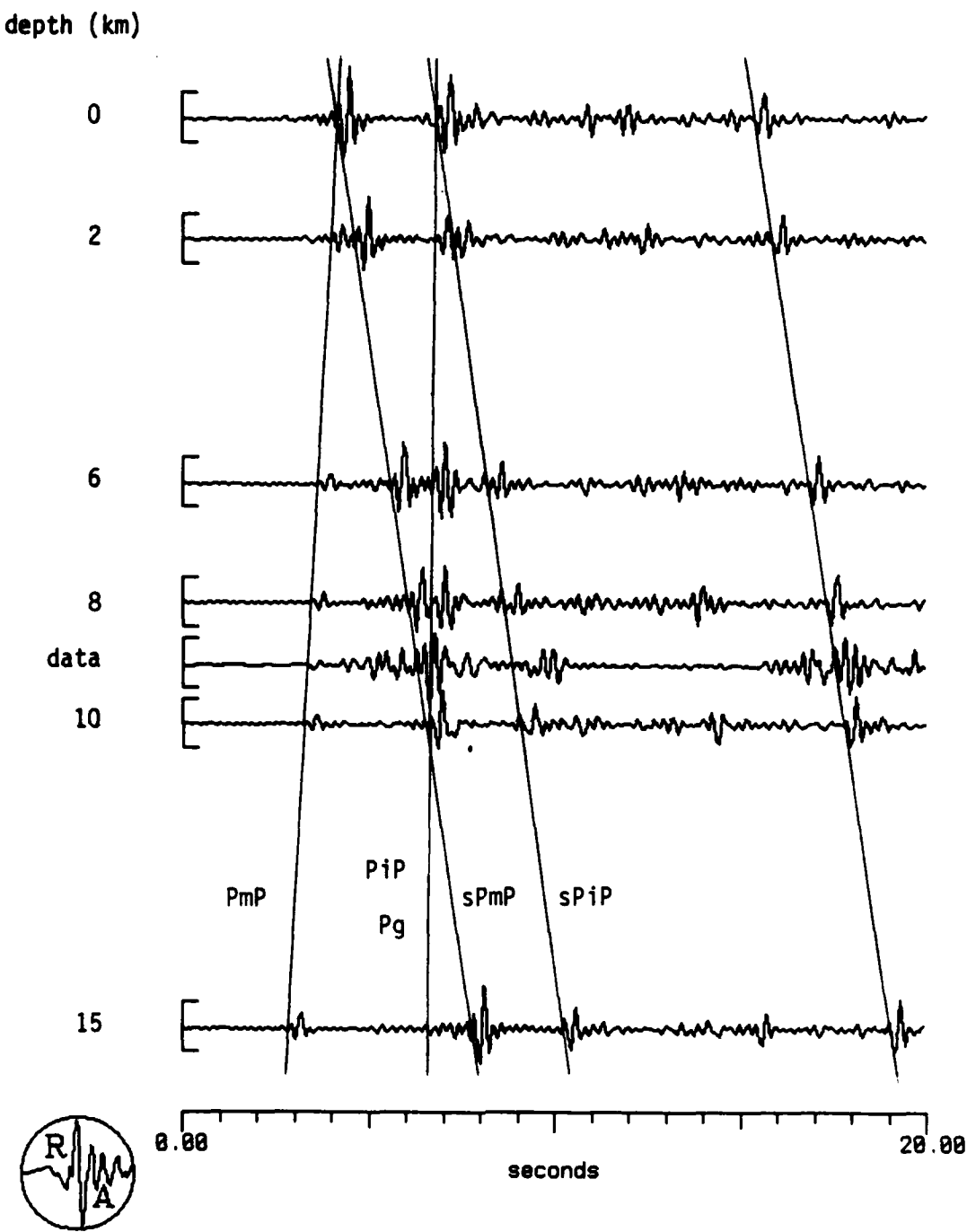
Figure 10. Same as Figure 9 except the real data are included in the depth section at a depth of about 9 km. See text for discussion.
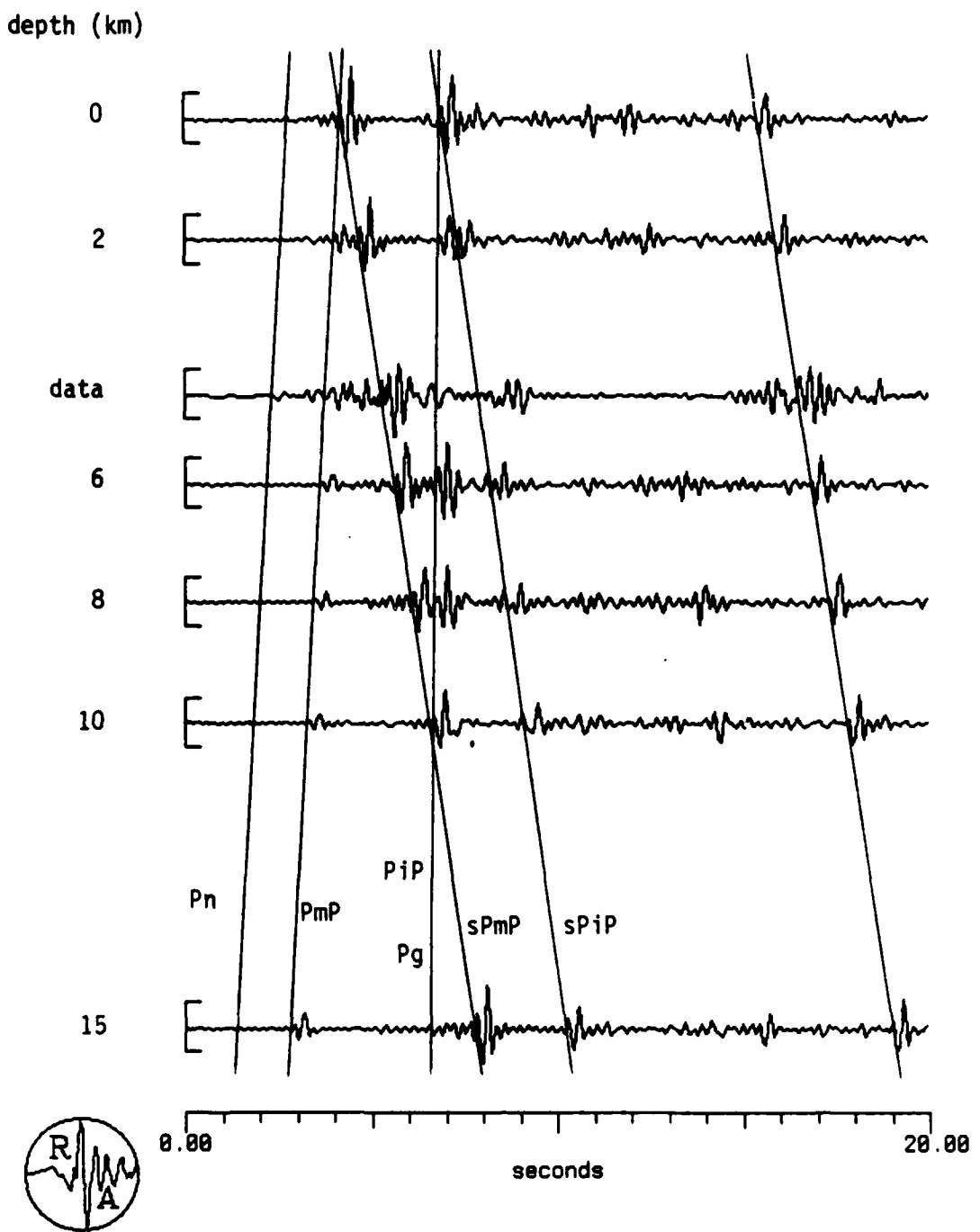
Figure 11. Like Figure 10 except notice that the real data
are plotted at a depth of about 4.5 km. See text
for discussion.
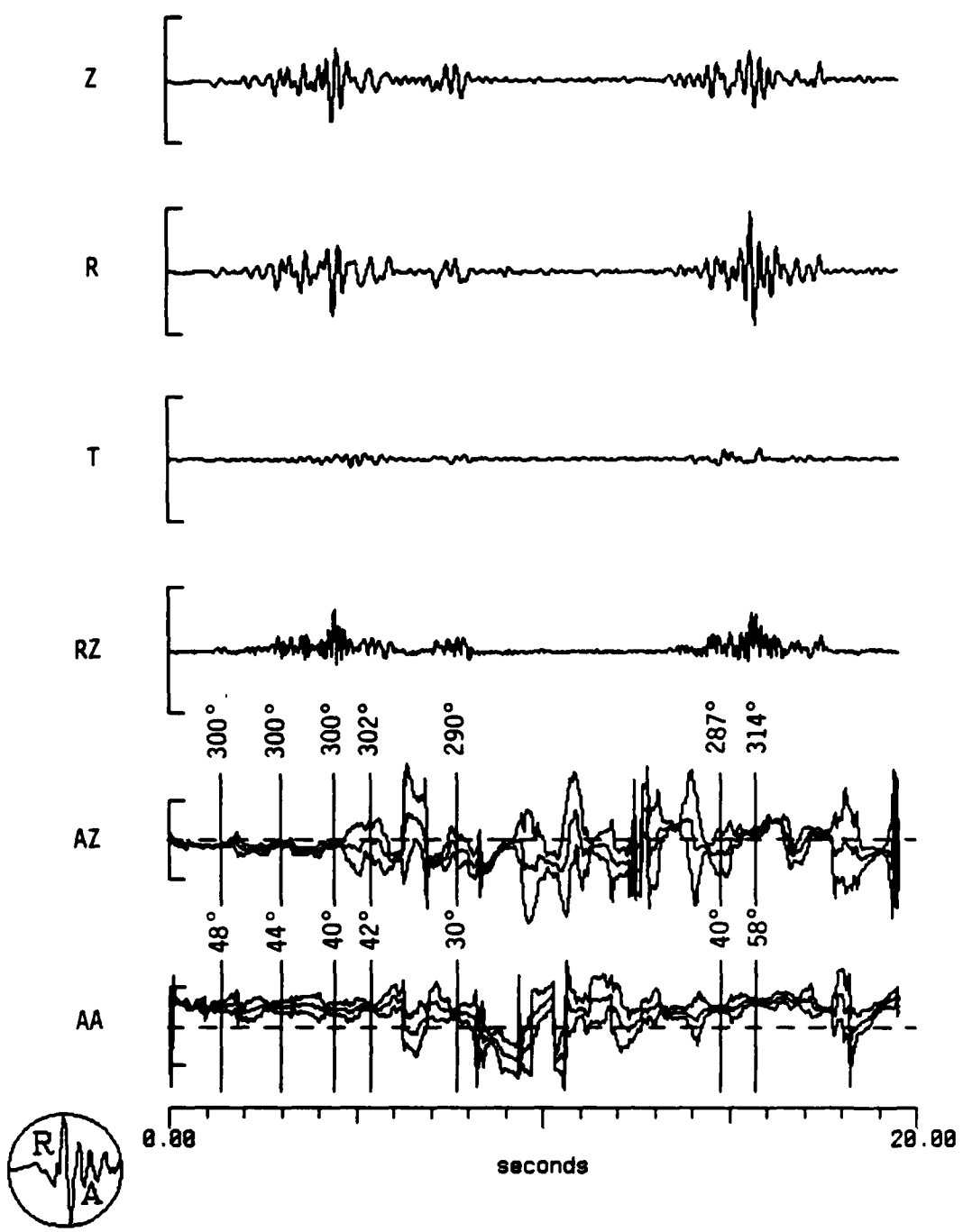
Figure 12. Adaptive polarization of state-filtered seismogram recorded at RSNY. The values of azimuth and apparent angle of incidence are given with estimated errors.

28

adaptive polarization analysis of the first 20 seconds of the same state-filtered seismograms that we have been comparing to the synthetics. The first three traces in the figure are the vertical, and the adaptive radial and transverse horizontal components. The direction of maximum signal strength as a function of time represented by the azimuth and apparent angle of incidence, is indicated (with error estimates) below the RZ product trace in Figure 12. The positive values for the product of the radial and vertical components indicate that all phases shown are arriving at the receiver as P-waves. Adaptive polarization analysis of the synthetic seismograms (not shown here) indicates the same thing; thus, at the very least, we know that the last conversions were to P-waves for both the real and synthetic data.

Interestingly, we noted that the last arrival, which had matched a predicted phase in the synthetics at both the 4.5 and 9 km depth positions, is probably not even modeled by the synthetics. Though highly polarized and hence a prominent phase in the data, it is fourteen degrees off the correct azimuth from the source. Unlike the two other out-of-line azimuths (see Figure 12), the error estimate is small and does not allow enough uncertainty to put it in line. Furthermore, this late phase is approaching the receiver at a shallower angle than any other arrival (see the angles of incidence), yet the late phase in the synthetic seismograms approaches the receiver at the steepest angle in the same 20 second time window. A steep, late arrival would be consistent with a multiply-reflected phase.

| TABLE 4		
Depth Estimates for the Gaza, New Hampshire, Earthquake January 19, 1982		
Depth Estimate (km)	Method	Reference
3	local network	Pulli *et al.*, 1983
3.5	teleseismic body wave modeling	Pulli *et al.*, 1983
9	relative relocations using aftershocks*	Brown and Ebel, 1985
4-11	regional, surface wave modeling	Hermann, pers. Communication

*Depth range of larger aftershocks recorded by portable instruments is 2.7-4.7km.

In the data, the phase immediately preceeding the last phase (by almost 1 second) is more consistent with the synthetics because it approaches at a steeper angle. Using that information, a different match can be obtained by inserting the data at a depth of 6 km (Figure 13). Here, the first arrival is a predicted *PmP* and there are phases matching
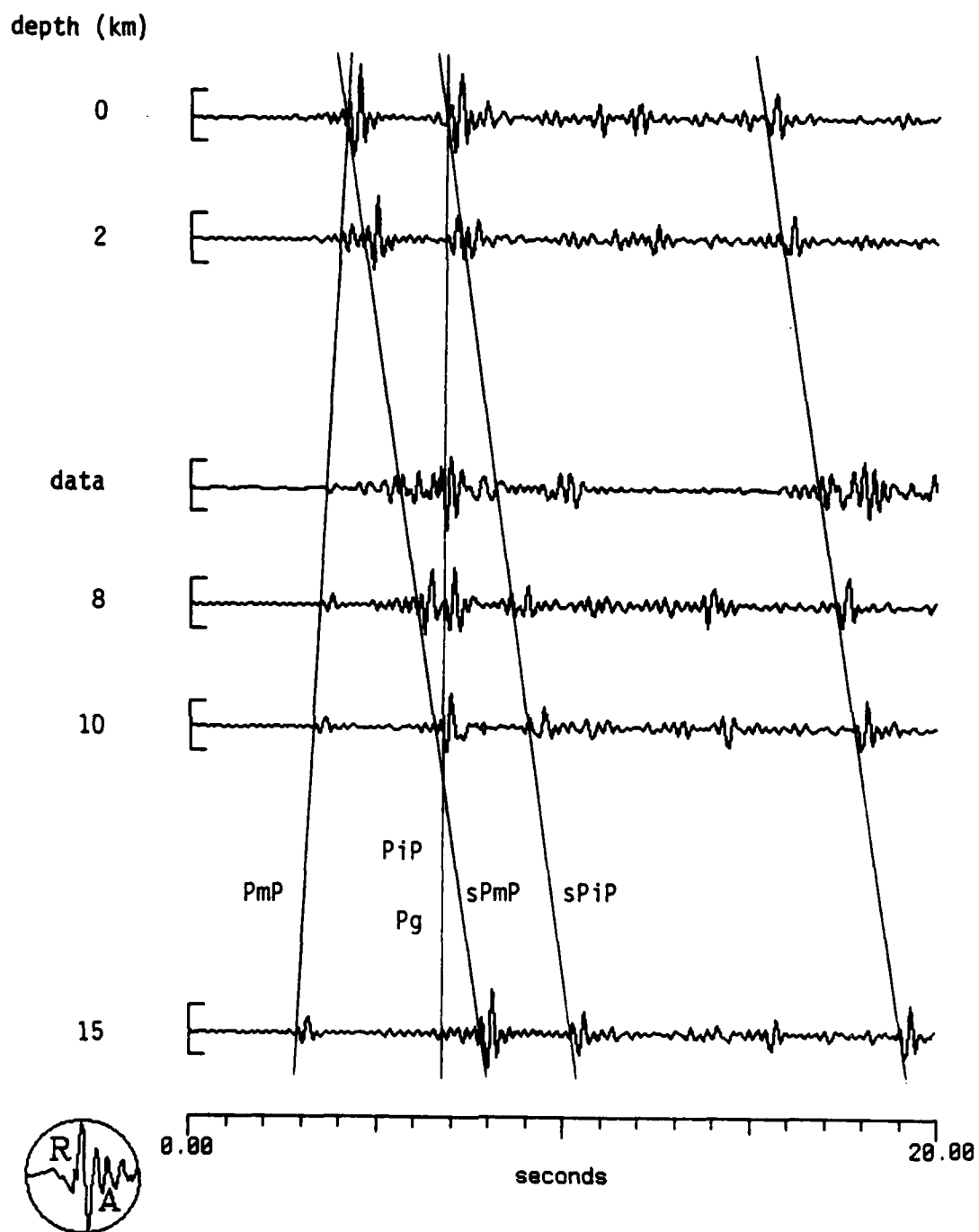
Figure 13. Like Figures 10 and 11 except the real data are plotted at a depth of 6 km in the depth section. See text for discussion.

the predicted *sPmP* and the dual arrival of *Pg* and *PiP*, as well as the late multiply-reflected phase. This interpretation, however, gives the largest mismatch in travel times.

One can see that it is not easy to choose among the above interpretations, because several are possible yet none provides a perfect match. The difficulties of identifying and correlating phases from a single set of three-component data are well-illustrated by this example. Evidently, this particular earthquake is difficult to pin down as the range of estimates for its focal depth is 3-11 km, using a variety of approaches (see Table 4).

Adirondack Mountains, August 31, 1982

No depth has been reported in the literature for the 31 August, 1982, Adirondack event. Its location is 156 km from RSNY at a station to event azimuth of 170°. Depth phases would be very difficult to identify if just the band pass filtered data rotated to the vertical, radial, and transverse directions of motion were examined (Figure 14, top). In this case, the polarization state filter was used effectively to pass only rectilinear motion and help in the depth phase identification (Figure 14, bottom).

The synthetic seismogram depth section computed for this event exhibits a strong *sPmP* phase, well defined *SmP*, *pSmP*, and *sPmS* phases and a weak *Pg* phase (Figure 15). The strike, dip, and rake for this event have not been published and a generic fault plane solution for this area based on other Adirondack events was used in the synthetic program. Thus, the relative amplitudes of the phases do not match the data (Figure 16). The state filtered data trace in Figure 16 has been aligned with the synthetics in absolute time. In other words, no movement of the data trace with respect to the synthetics along the time axis was allowed. With this constraint, the large first arrival in the data trace is identified as the *Pg* arrival and the second arrival is the *sPmP* arrival. The small arrival at about 10 seconds on the data trace may be the *pSmP* arrival.

The best fit of the data to the synthetics is at 7 km depth. We note however, that if amplitudes are ignored (as they should be in this case) the fit of the data to the synthetics is nearly as good for any depth between 7 and 13 km.

Maine, May 29, 1983

The reported hypocenter of the Maine event is at 44.50° N, 70.41° W, at a depth of 2 km. This location is 328 km due east of RSNY, the largest distance to any of the northeast U.S. events studied. The data are characterized by a small *Pn* phase arriving 46 seconds after the rupture followed 5 seconds later by a rather large emergent *Pg*. The coda amplitude remains fairly constant from the *Pg* arrival to the *Lg* arrival 38 seconds later (Figure 17). Synthetic seismograms computed for this event show large amplitude *sPmP*, *PiP* and *sPiP* phases and several unidentified depth phases (Figure 18). The coda of the *Pg* arrival in the data is not well matched by the synthetics for a 2 km source depth. Of more importance is the mismatch of amplitudes of the *sPmP* arrival. The *sPmP* arrival in the data has the same small amplitude as the *PmP* arrival. A better fit of the data to the synthetics occurs at 12 km source depth (Figure 19). At this
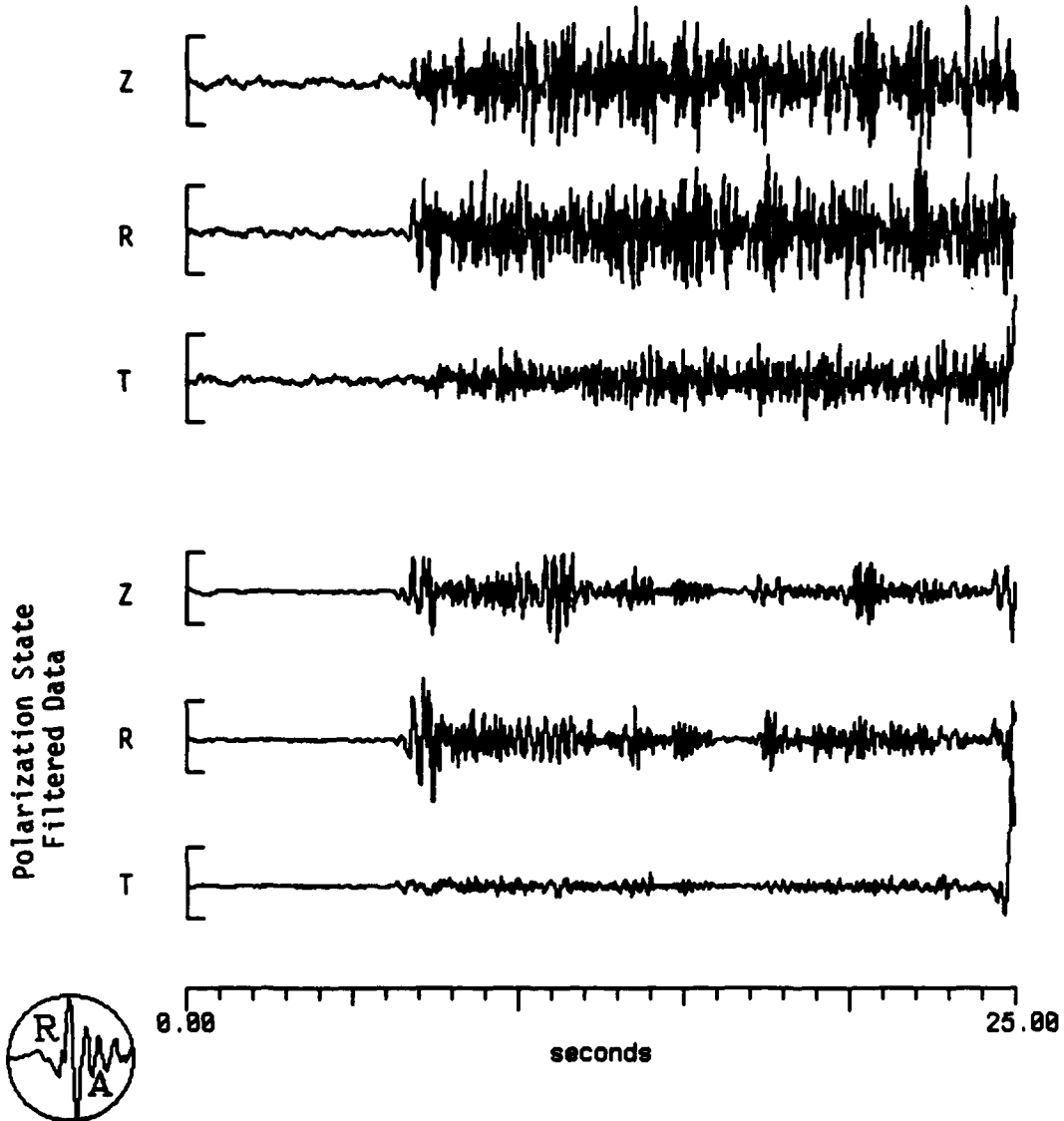
Figure 14. Vertical, radial, and transverse components of motion for the August 31, 1982, Adirondack earthquake as recorded at station RSNY, $\Delta=156$ km. Lower traces have been polarization state filtered for rectilinear motion to enhance the depth phases.

depth (km)
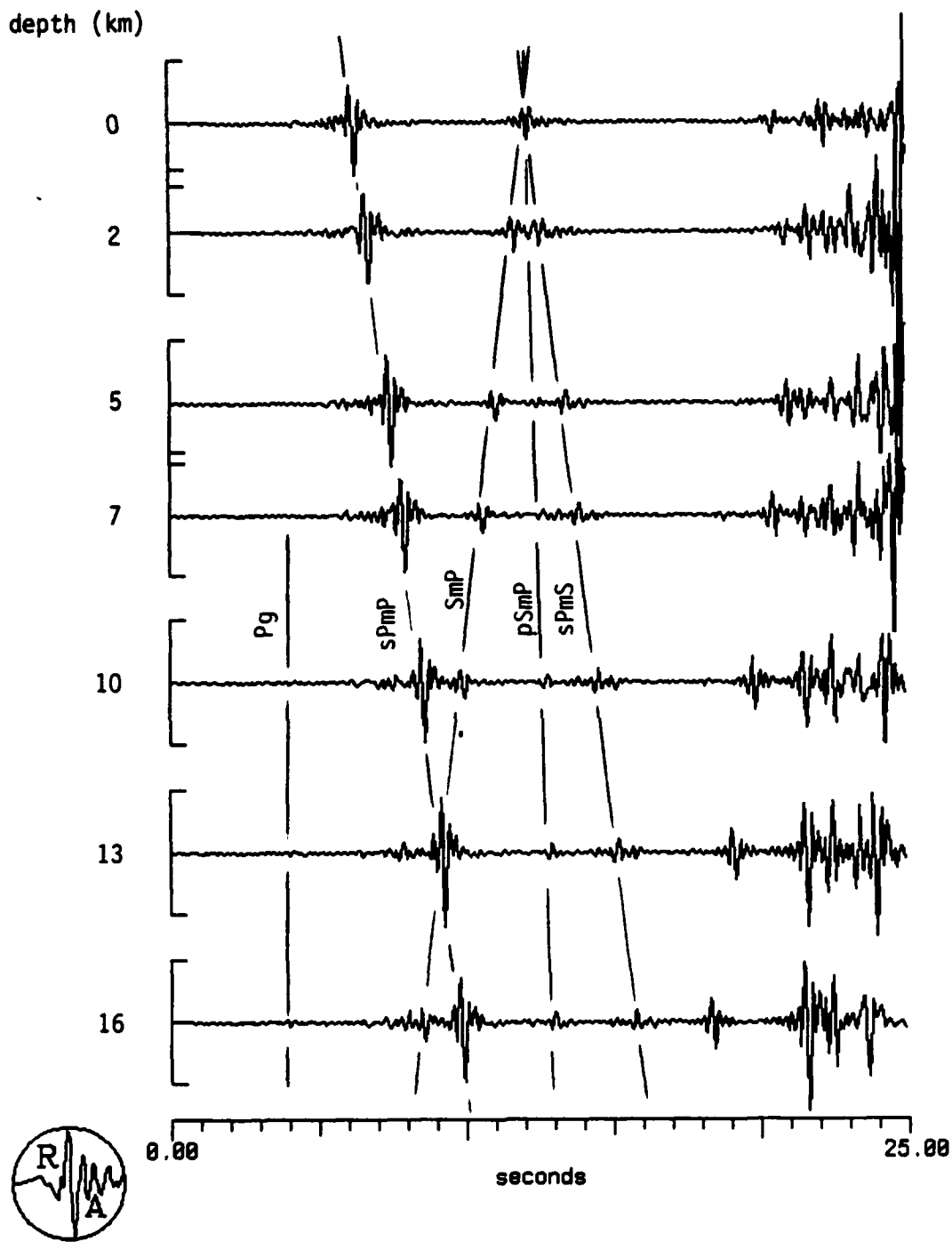
Figure 15. Synthetic seismogram depth section for the Adirondack earthquake. $\Delta = 156$ km, strike=173°, dip=60°, rake=110°, station to event azimuth=170°.

depth (km)

0.00   15.00

seconds
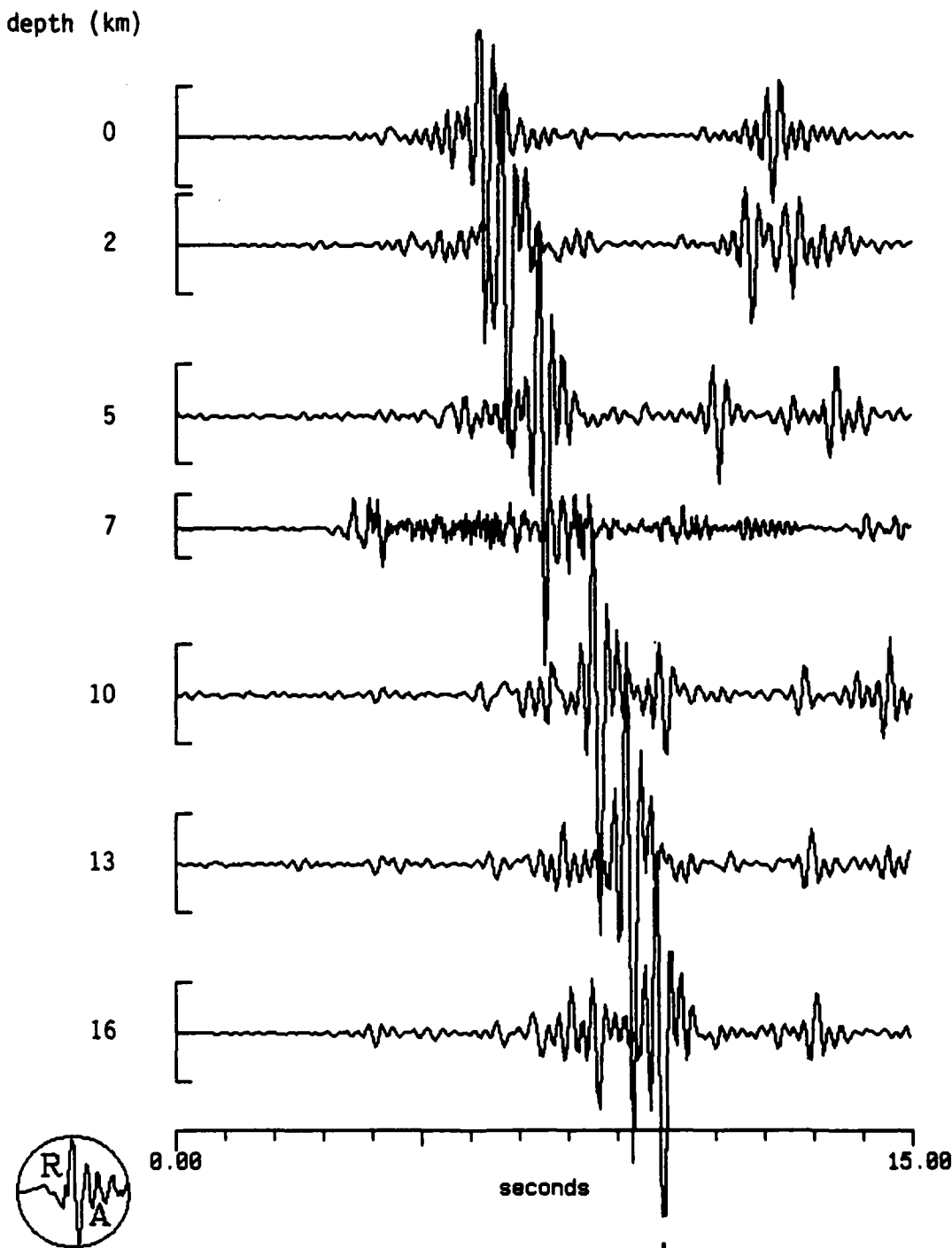
Figure 16. Best fit of the RSNY data to the synthetics for
the Adirondack earthquake (7 km). There has
been no published depth for this event. See Fig-
ure 15 for details of the synthetics.

34
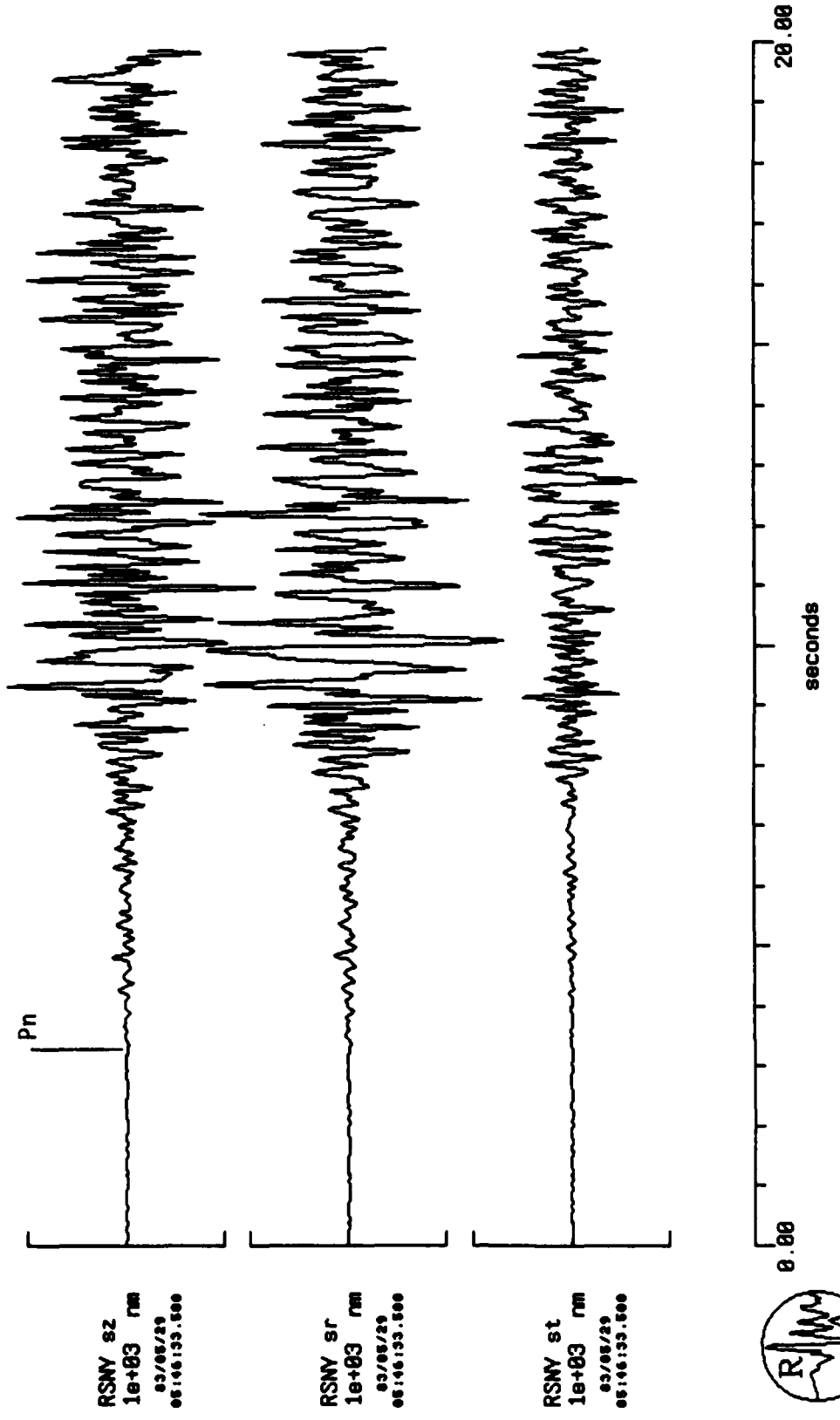
Figure 17. Vertical, radial, and transverse components of motion for the May 29, 1983 Maine earthquake as recorded at station RSNY, Δ=328 km. The *Pn* arrival is shown with a marker.
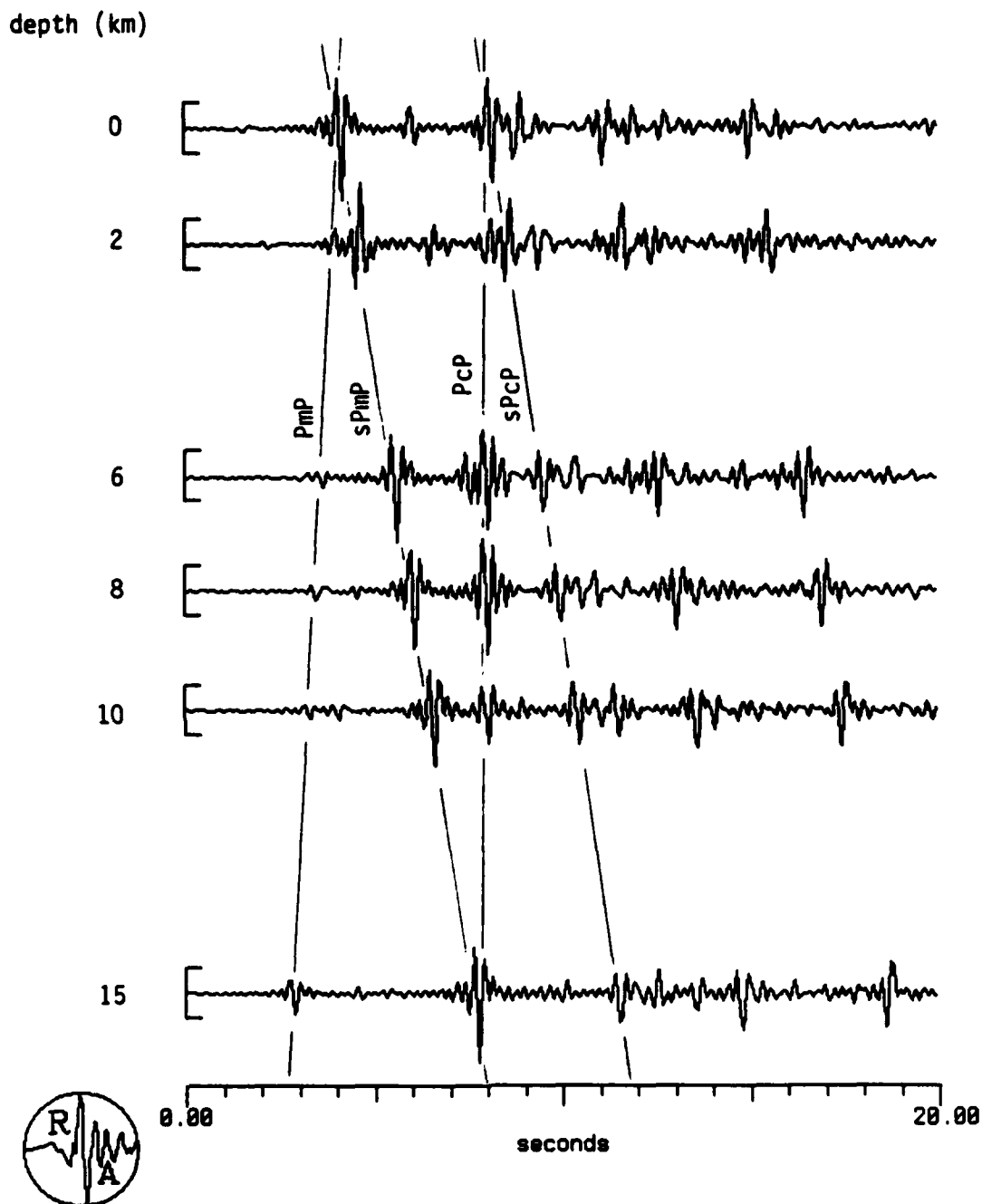
Figure 18. Synthetic seismogram depth section for the Maine earthquake $\Delta=328$ km, strike=355°, dip=52°, rake=78°, station to event azimuth=90°.

depth (km)
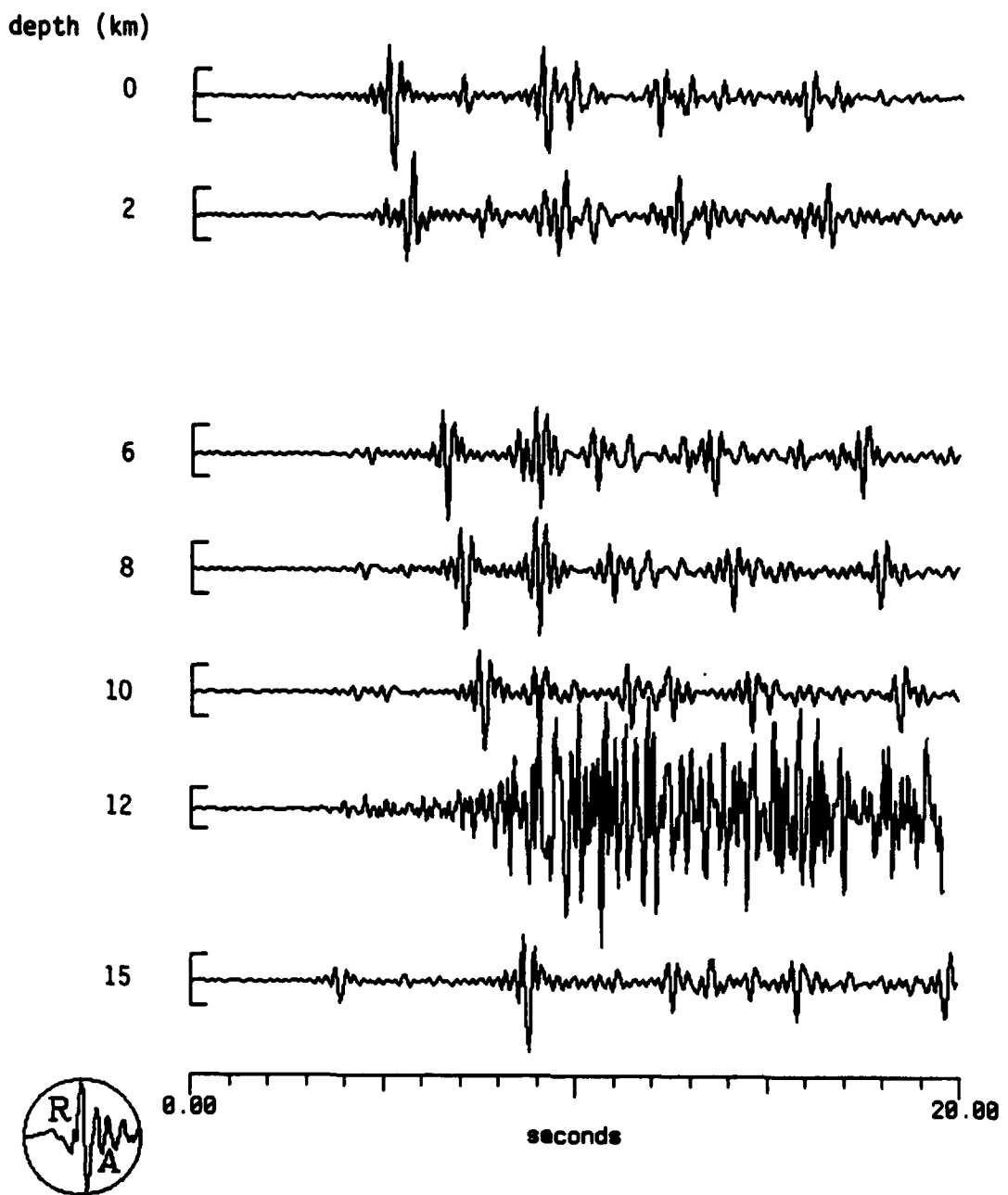
Figure 19. Best fit of the RSNY data to the synthetics for the Maine earthquake (12 km). The published depth based on an aftershock survey is 2 km. See Figure 18 for details of the synthetics.

depth the *sPmP* phase arrives in the *Pg* coda where the amplitudes are better matched and the arrival times of the distinct phases in the data are modeled well by the synthetics. Regional network data from 36 stations placed the depth of this event at 1.8 km. Support is lent to this depth by an aftershock survey conducted shortly after the main shock that obtained a well determined depth of 2.4 km for one of the aftershocks (Ebel and McCaffrey, 1984).

Goodnow, New York, October 7, 1983

The Goodnow sequence of earthquakes occurred in the central Adirondack mountains of New York on October 7, 1983. Following the m_b 5.3 main shock, there were nearly 100 aftershocks with magnitude 3.5 and lower that occurred over the next two months. Station RSNY, just 69 km from the event recorded the *P*-waves reliably but clipped in the *Lg* portion of the wavetrain. The strike, dip, and rake of the main shock from first motion data are 173°, 60°, and 110°. Station RSNY is at an azimuth of 162° and lies close to the intersection of the two nodal planes of the main shock. Thus, the record character for synthetics at RSNY is sensitive to small changes in focal mechanism.

The data shown in Figure 20 have been rotated to the vertical, radial, and transverse directions and has been band-pass filtered between .5 and 5 Hz for comparison to the synthetics. Several distinct phases are evident in the data.

Figure 21 shows the synthetic seismogram depth section for this event. The *Pg* arrival, strong when the source is deep, weakens significantly with foci near to the surface. The predominant phases are the *sPiP* and the *SmP* which exhibit strong amplitudes throughout the section.

A match of the data to the synthetics is shown in Figure 22. The initial *Pg* arrival in the data trace is about .5 seconds earlier than the same phase in the synthetic section and the second arrival is not matched at all by the synthetics. Beyond that however, the *sPcP*, *sScP*, *pPmP* and *SmP* phases are all matched well for a source depth of 10 km. Despite the sensitivity of the synthetics to small changes in the focal mechanism at this azimuth, the relative amplitudes of the phases are fairly well matched also.

Two depths have been reported for this event, one at 7 km ± 1 and one at 14 km ± 5. The shallow depth is based on aftershocks and on teleseismic observations of the main event, while the deeper depth is based on local travel times. The depth determined here lies between these two estimates. range of depths.

The large size of the Goodnow event (m_b = 5.3) raises the possibility of a complex source function. If this were the case, the complexities could be falsely identified as depth phases and an improper depth determined. At this point, we do not know whether or not source complexities have influenced the depth for the Goodnow event.
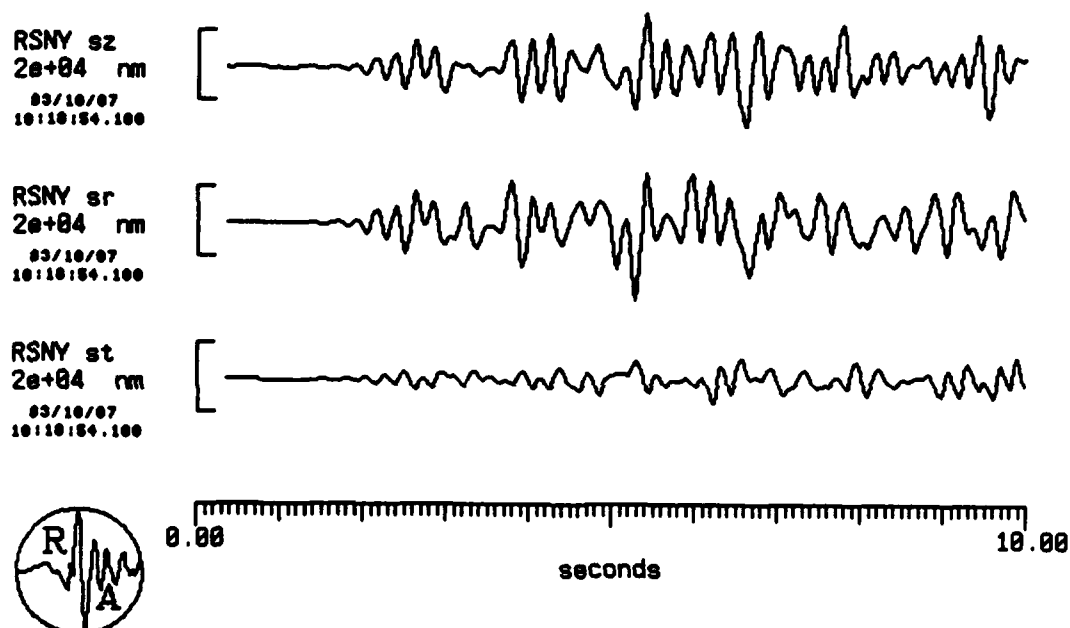
Figure 20. Vertical, radial, and transverse components of
motion for the October 7, 1983, Goodnow earth-
quake as recorded at station RSNY, Δ=69 km.
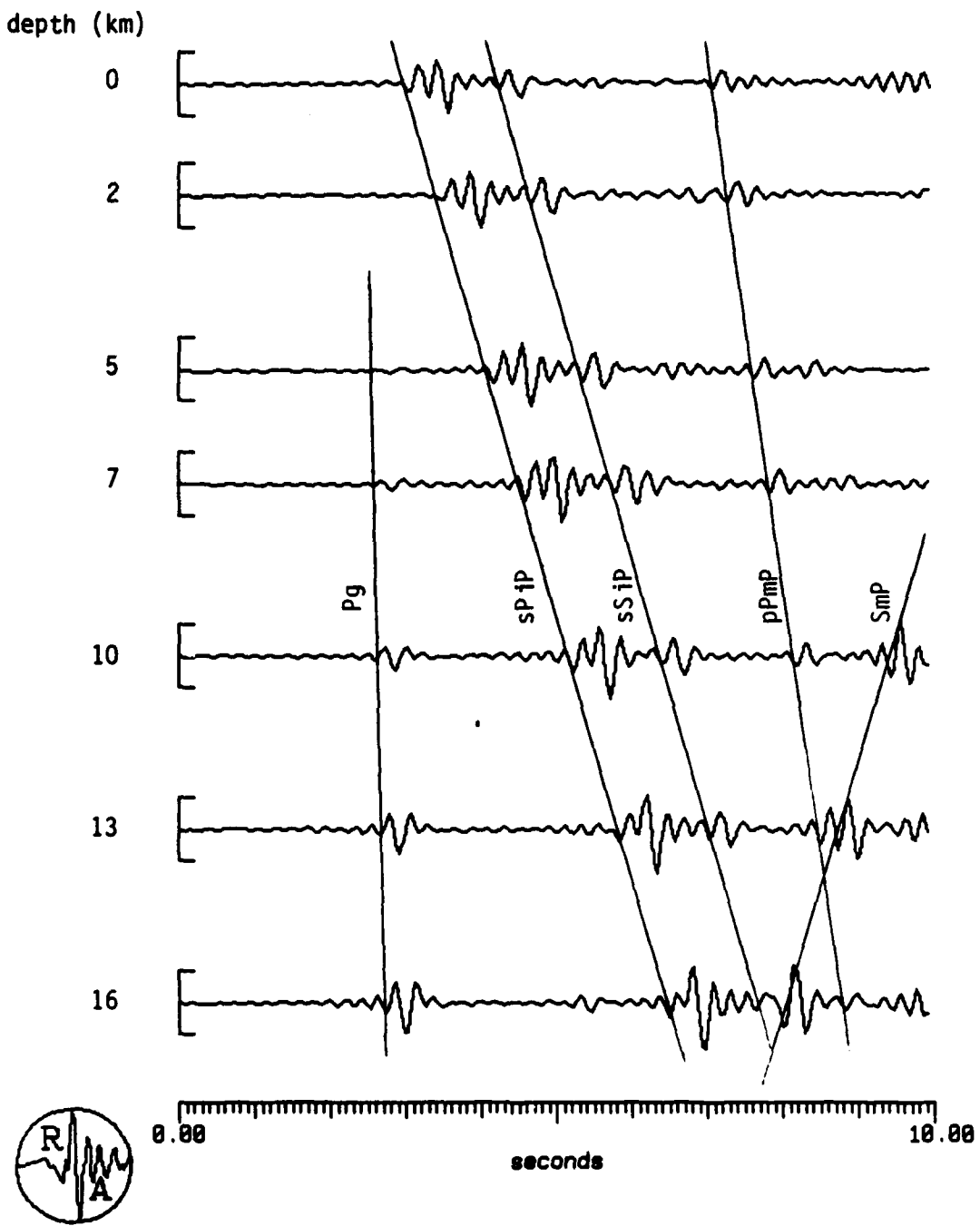
*Figure 21.* Synthetic seismogram depth section for the Goodnow earthquake. Δ=69 km, strike=173°, dip=60°, rake=110°, station to event azimuth=163°.
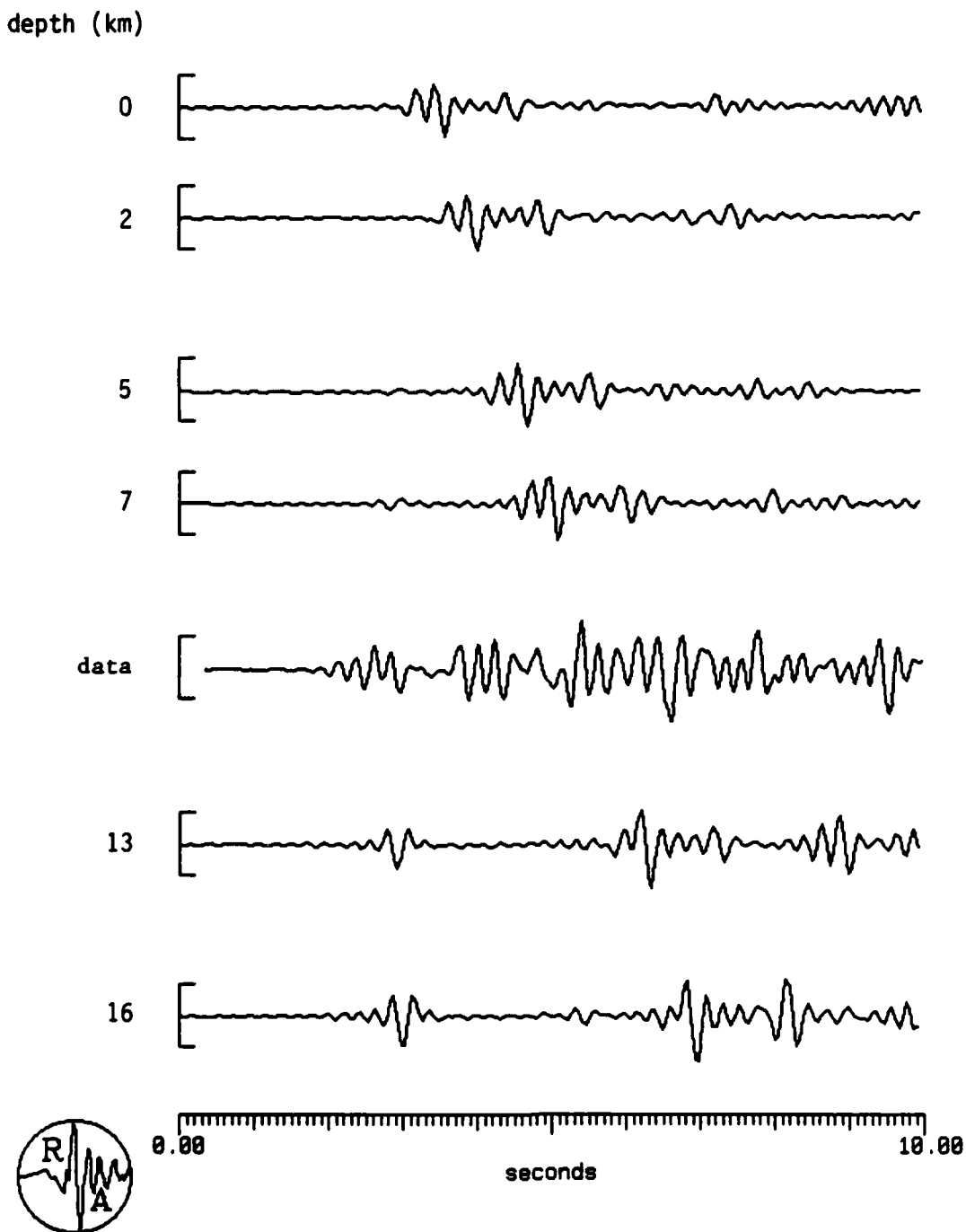
Figure 22. Best fit of the RSNY data to the synthetics for the Goodnow earthquake (10 km). The published depths range between 7 and 12 km. See Figure 21 for details of the synthetics.

41

Ontario, October 11, 1983

The Ontario event occurred 123 km from station RSNY. It was a magnitude 4.2 event and had a reported depth of 15 km. Although the travel path between the event and RSNY was wholly within the Grenville province (Figure 4), distinct phase are difficult to identify in the data. Figure 23 shows the data rotated to the vertical, radial, and transverse directions. From the initial *Pg* arrival, the coda gradually increases in amplitude for the next 4 seconds.

Synthetic seismograms for this event (Figure 24) have a small *Pg* phase followed by a large amplitude *PmP* phases a few seconds later. Well into the coda there is a well defined set of arrivals consisting of the *SmP*, *PmS*, *pSmP*, and *sPmS* phases

The fit of the data to the synthetics is poor (Figure 25). Neither the arrival times nor the amplitude characteristics are matched. The depth that we have assigned to this event (14 km) is based primarily upon the spacing of the (presumed) *Pg* and *PmP* phases.

Adirondack, New York, October 23, 1984

On October 23, 1984, a magnitude 3.4 earthquake occurred in the southwestern Adirondacks, near Johnsburg, New York. Because it was recorded by RSNY and SRNY, it afforded us the chance to model seismograms at two different receivers and thus increase our confidence in the interpretations. We estimate a source depth of 12 km and a strike, dip, and rake of 353°, 60°, and 17° for this earthquake based on the results described below. Neither the depth nor the fault plane solution could be determined by local network data, though many stations recorded the event and its epicentral location is fairly well constrained with an azimuthal gap of 43°. The nearest network station, however, is 52 km from the source.

Synthetics to both RSNY and SRNY were calculated with the Adirondack velocity model. Initially, we tried the fault-plane solution of the Goodnow earthquake because it is well constrained and is similar to many other Adirondack solutions (e.g. Yang and Aggarwal, 1981). Resulting vertical and radial synthetic depth sections are shown in Figures 26 and 27 along with RSNY band-pass filtered data plotted at a depth of 12 km. The data and synthetics, though aligned at the same time with respect to the origin time, do not look much alike. The lack of fit between data and synthetics, particularly for the relative amplitudes of different phases, suggests that the fault plane solution and hence radiation pattern of the synthetics is incorrect. A much better match is achieved using a different fault plane solution of strike = 353°, dip = 60°, rake = 17° (Figures 28 through 31). This mechanism has a greater strike-slip component and is not unlike several previously determined Adirondack mechanisms (Schlesinger - Miller, *et al.*, 1983). In Figures 28 and 29 RSNY vertical and radial seismograms are again plotted at a depth of 12 km where the arrival times and relative amplitudes, especially of *PmP* and *sPmP*, are well modeled by the synthetics. Furthermore, the polarity of the 3-cycle waveform, *sPmP*, is opposite that of *PmP* on both data and synthetics. *Pg* is nearly nodal for the theoretical seismograms and, in fact, no signal above noise was detected on

RSNY sz
1e+03 nm
83/18/11
84:11:12.888

RSNY sr
1e+03 nm
83/18/11
84:11:12.888

RSNY st
1e+03 nm
83/18/11
84:11:12.888

0.00   15.00

seconds
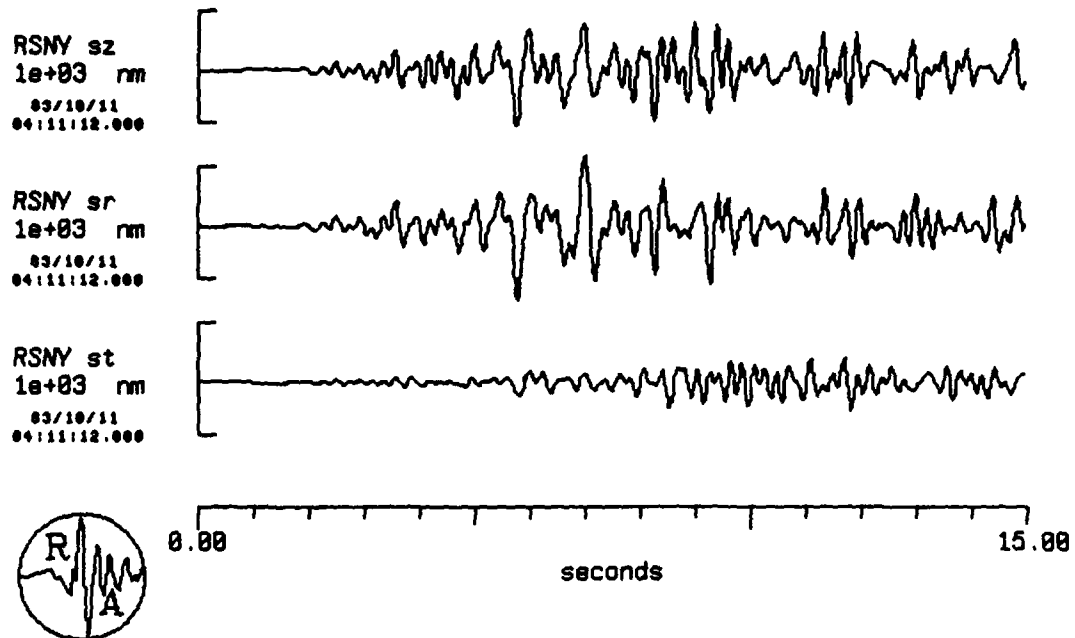
Figure 29.   Vertical, radial, and transverse components of
motion for the October 11, 1983, Ontario earth-
quake as recorded at station RSNY, $\Delta = 123$ km.

43
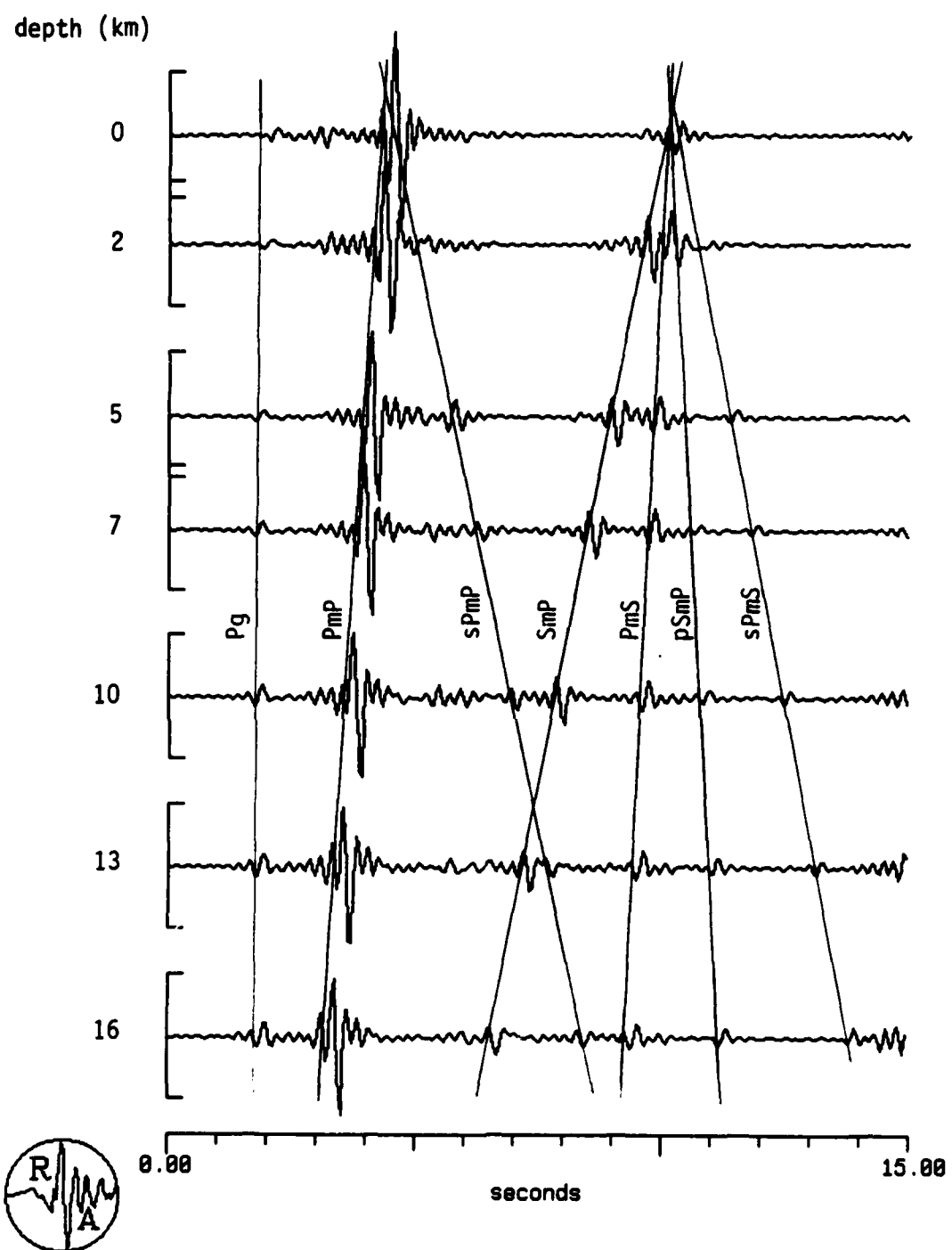
Figure 24. Synthetic seismogram depth section for the Ontario earthquake. Δ=123 km, strike=71°,
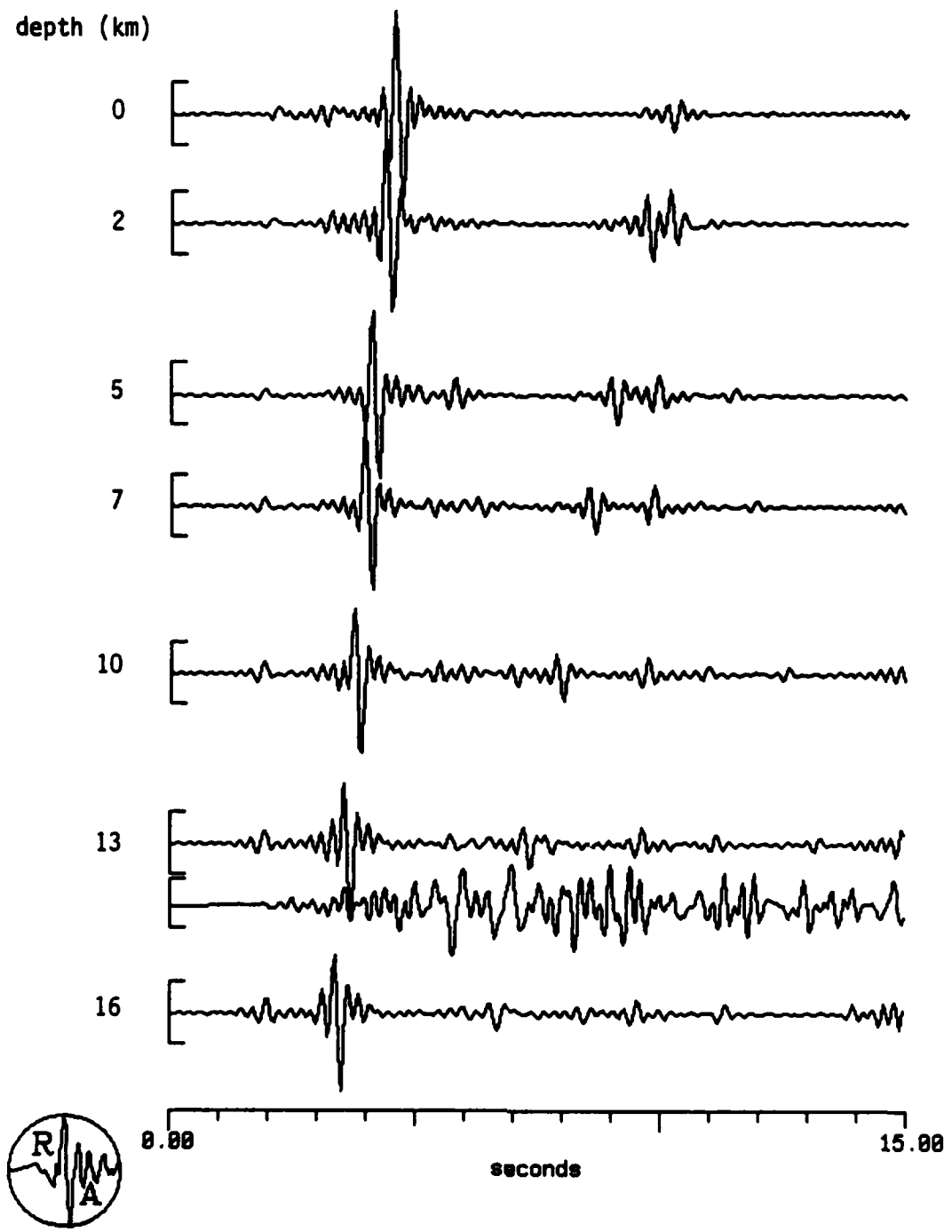
Figure 25. Best fit of the RSNY data to the synthetics for the Ontario earthquake (13 km). The published depth for this event is 15 km. See Figure 24 for details of the synthetics.

45

depth (km)
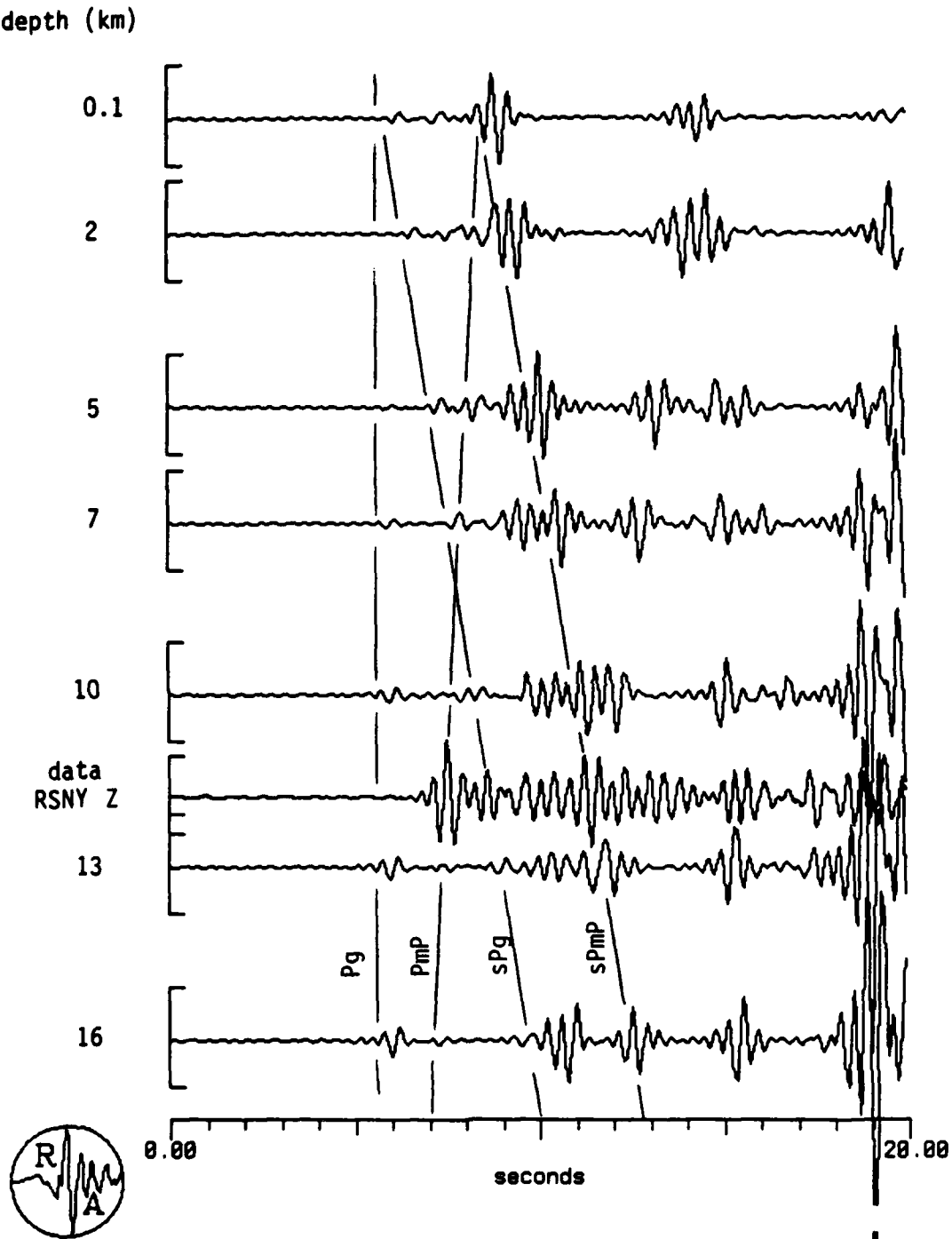
Figure 26. Vertical-component synthetic seismogram depth section for the October 23, 1984, earthquake with the RSNY vertical trace plotted at 12 km depth. Synthetics are low-pass filtered from 3 Hz. Data are band-pass filtered, 1-3 Hz. Strike=173°, dip=60°, rake=110°, Δ=115 km, azimuth=336°. Receiver response=RSNY short period.
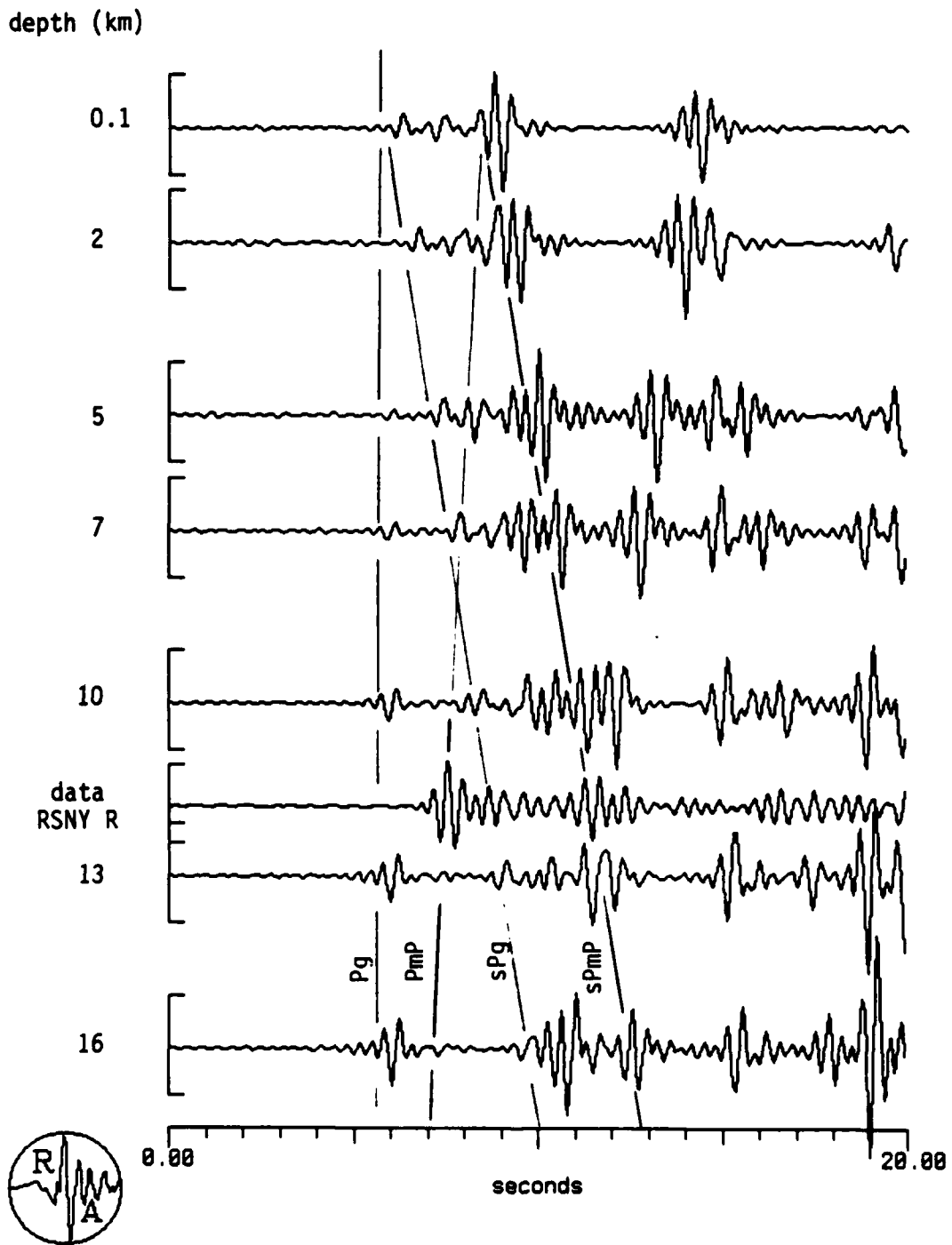
Figure 27. Radial-component synthetic seismogram depth section for the October 23, 1984, earthquake with the RSNY radial trace plotted at 12 km depth. Synthetics are low-pass filtered from 3 Hz. Data are band-pass filtered, 1-3 Hz. Strike=173°, dip=60°, rake=110°, Δ=115 km, azimuth=336°. Receiver response=RSNY short period.
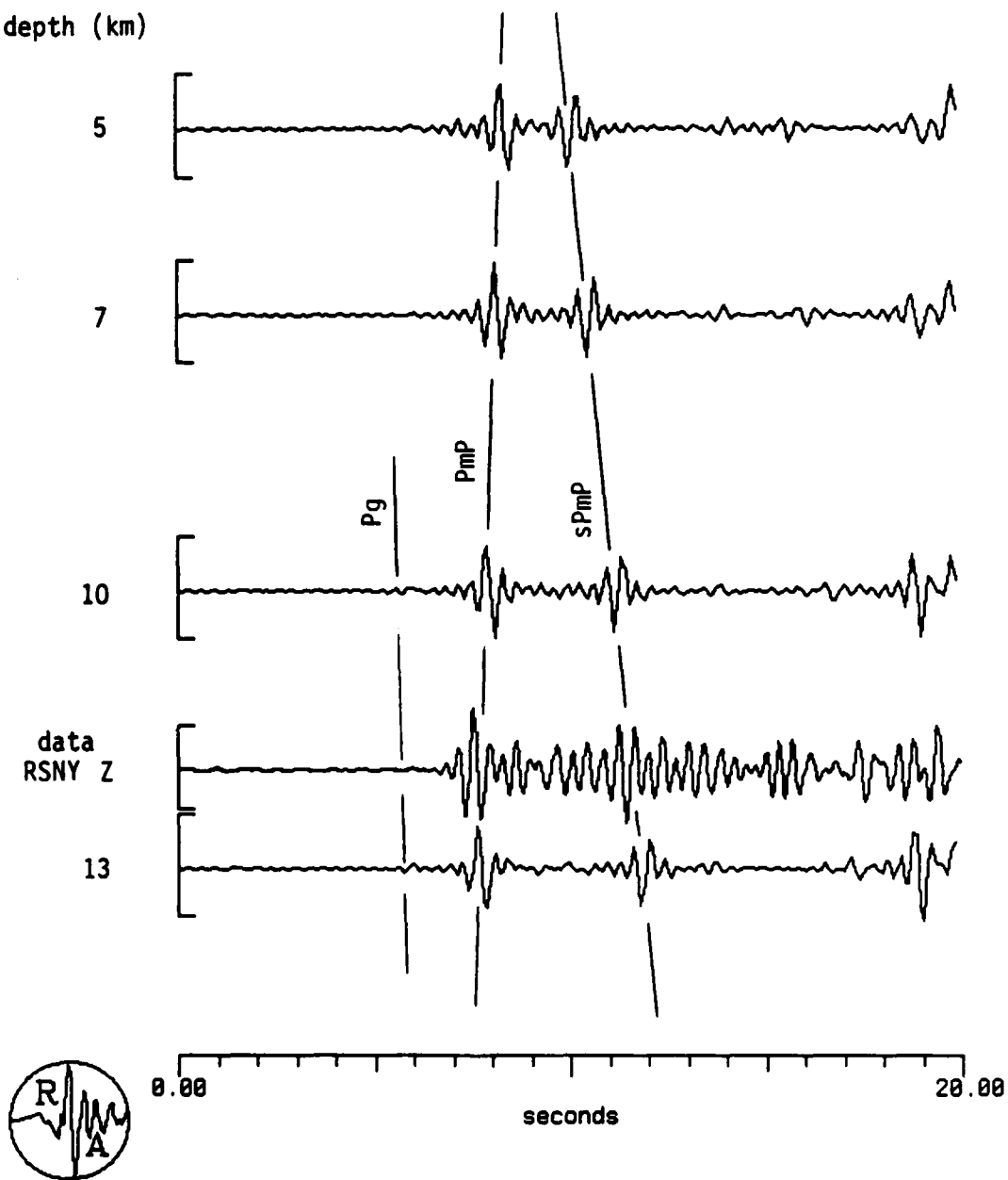
Figure 28. Vertical-component synthetic seismogram depth section for the October 23, 1984, earthquake with the RSNY vertical trace plotted at 12 km depth. Synthetics are low-pass filtered from 3 Hz. Data are band-pass filtered, 1-3 Hz. Strike=353°, dip=60°, rake=17°, Δ=115 km, azimuth=336°. Receiver response=RSNY short period.
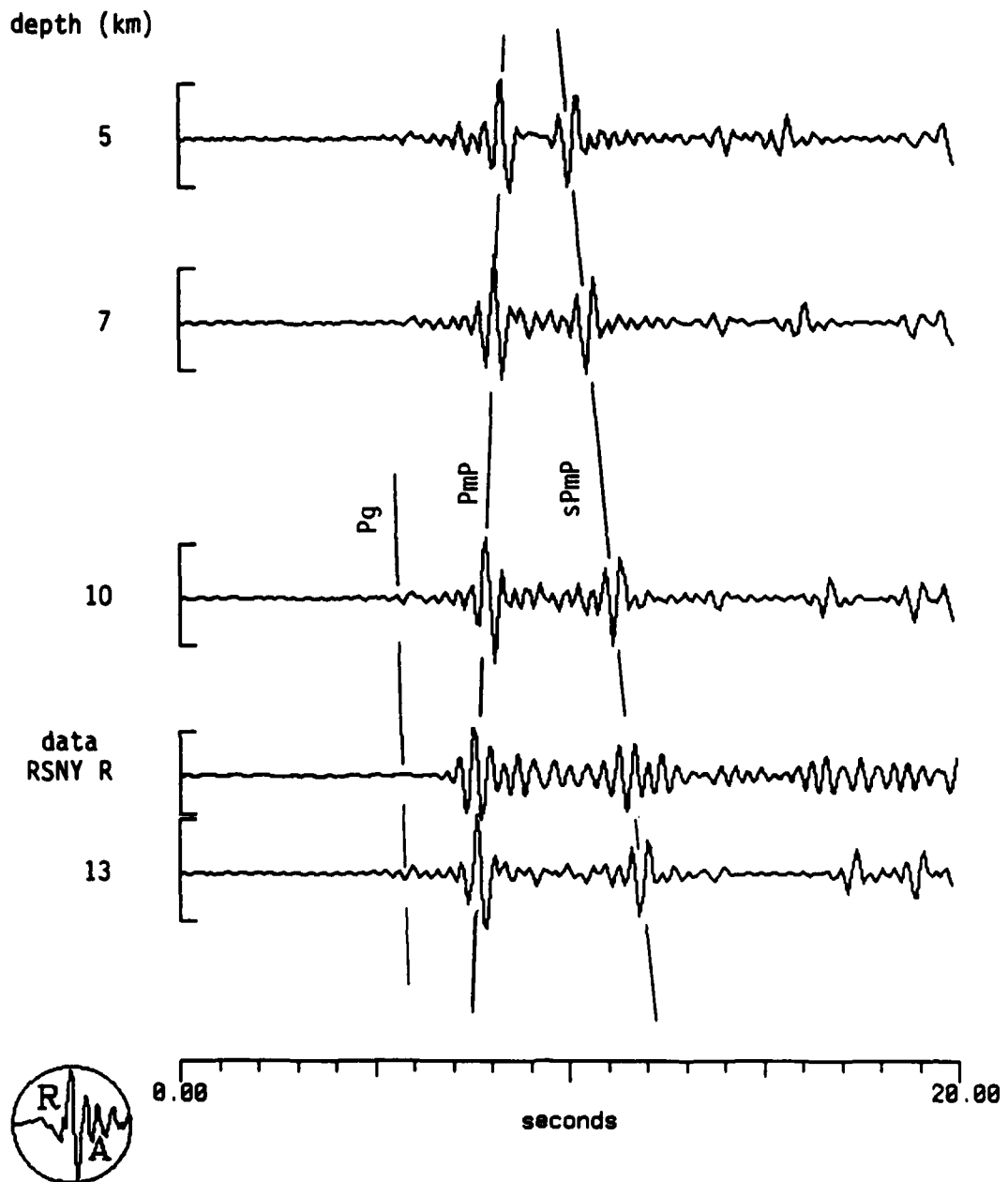
Figure 29. Radial-component synthetic seismogram depth section for the October 23, 1984, earthquake with the RSNY radial trace plotted at 12 km depth. Synthetics are low-pass filtered from 3 Hz. Data are band-pass filtered, 1-3 Hz. Strike=353°, dip=60°, rake=17°, Δ=115 km, azimuth=336°. Receiver response=RSNY short period.
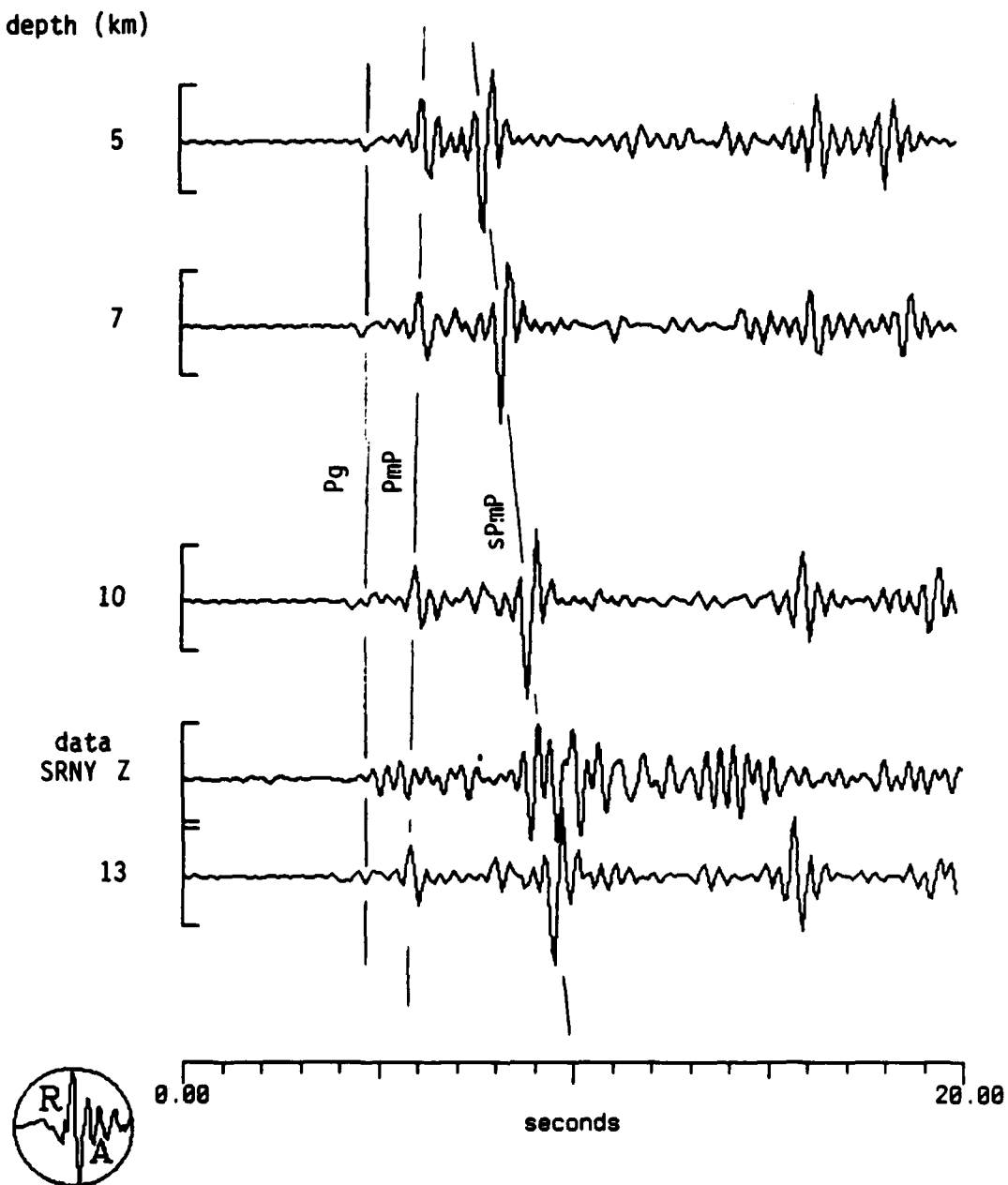
Figure 30. Vertical-component synthetic seismogram depth section for the October 23, 1984, earthquake with the SRNY vertical trace plotted at 12 km depth. Synthetics are low-pass filtered from 3 Hz. Data are band-pass filtered, 1-3 Hz. Strike=353°, dip=60°, rake=17°, Δ=195 km, azimuth=185°. Receiver response=SRNY broad band.
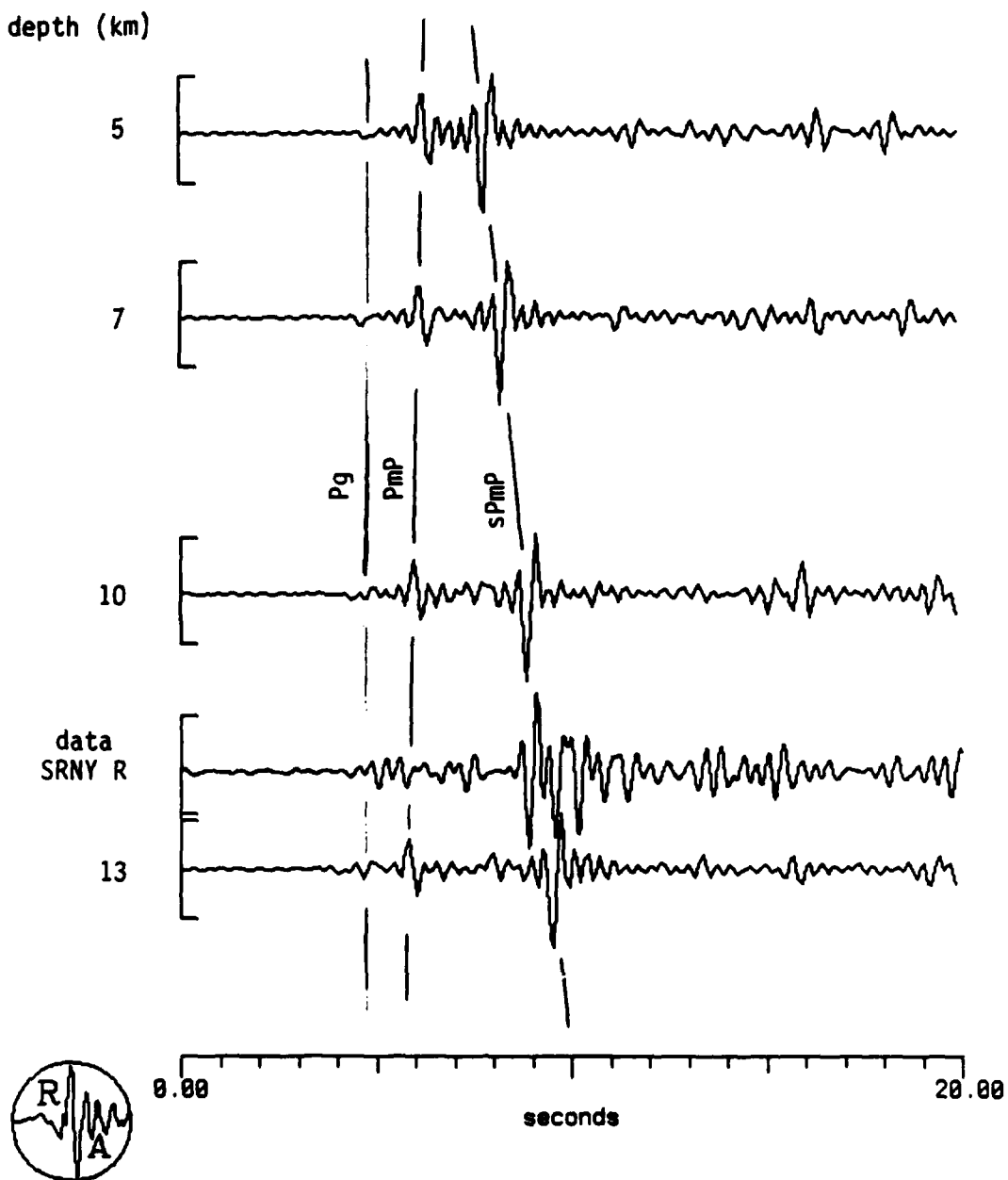
Figure 31. Radial-component synthetic seismogram depth section for the October 23, 1984, earthquake with the SRNY radial trace plotted at 12 km depth. Synthetics are low-pass filtered from 3 Hz. Data are band-pass filtered, 1-3 Hz. Strike=353°, dip=60°, rake=17°, Δ=195 km, azimuth=185°. Receiver response=SRNY broad band.

the observed seismogram. We are fairly confident of our interpretation of the first arrival at RSNY as PmP because its travel time and phase velocity, 6.8 km/sec, are both appropriate for PmP. Phase velocities are estimated using a V_p of 5.75 km/sec at the receiver (as reported in Taylor and Qualheim, 1983) and measuring observed angles of incidence.

Synthetics for the second fault plane solution also compare reasonably well with the data at SRNY for the same depth of 12 km (shown in Figures 30 and 31). Here the travel times and relative amplitudes of Pg and $sPmP$ are closely matched. On the other hand, PmP is not pronounced in the data. We do not, however, expect the fit to be as good because SRNY is farther from the source and lies in a different geologic province. Nonetheless, the results for both stations support the interpretation of the observed phases and a depth estimate of 12 km.

Mid-Hudson New York Earthquake and Quarry Blast

On October 30, 1985, a small earthquake occurred near Amsterdam, N.Y., only 4 km surface distance from an active quarry. This gave us a chance (rare in the eastern U.S.) to compare an earthquake to a blast source from nearly the same location. We attempted to model the earthquake and a blast to station SRNY, a distance of 120 km and 117 km from the respective sources. Several lines of evidence suggest the earthquake was shallow, but we caution against complete confidence in a one-station interpretation because:

1. the P-wave signal-to-noise ratio at SRNY is poor and

2. both the focal mechanism and the velocity model were unknowns.

A visual comparison of three-component seismograms (0.5-30 Hz) for the earthquake and for a large quarry blast that occurred earlier in October, 1985 (Figure 32), shows a difference in P and S/Lg coda shape, even though the records are obviously noisy. One-to-five Hz band-pass filtered data are shown in Figure 33 to illustrate that, despite differences in the seismograms, there appear to be S and Lg phases for both events. Unfortunately, we don't know the origin time of this particular blast, and, because the first P-wave arrivals are so unclear for both events, it is not obvious how the blast should be aligned relative to the earthquake or to synthetics. The time alignment illustrated in the Figure is based on a visual match of large amplitudes on the vertical components, and it looks sensible, but is it meaningful?

We subsequently examined digital seismograms of network stations run by Woodward-Clyde Consultants. Because those records also showed similarities in relative timing of arrivals between the earthquake and blasts at the same receiver, we concluded that blast phases and earthquake phases have the same travel-times. We still do not understand what an "S-wave" from the blast actually is, but with the 3-component SRNY data we were able to observe the particle motion and *neither* the earthquake nor the blast exhibit S-type motion for the relatively strong arrival that has a group velocity of 3.6 km/sec. Nevertheless, the interpretation of "matching phases" shown by the alignment of the time series in Figure 33 is what we will use to compare SRNY data to
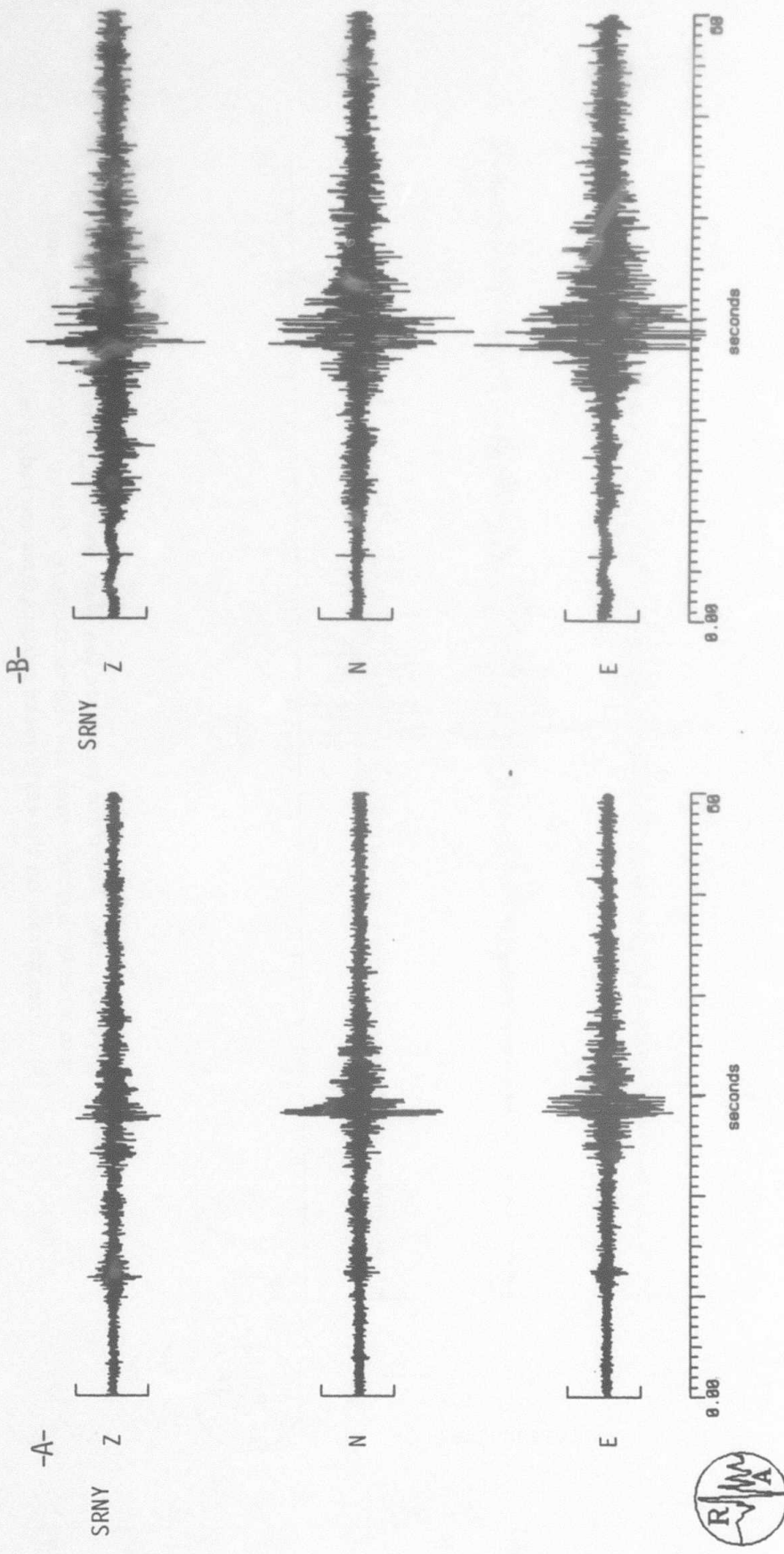
Figure 32. High-pass filtered 3-component data (> 0.5 Hz) A) Quarry blast near Amsterdam, NY, at SRNY, Δ=117 km. B) Earthquake near Amsterdam, NY, at SRNY. Δ=120 km, M = 2.7. The surface distance between the two sources is 4 km.
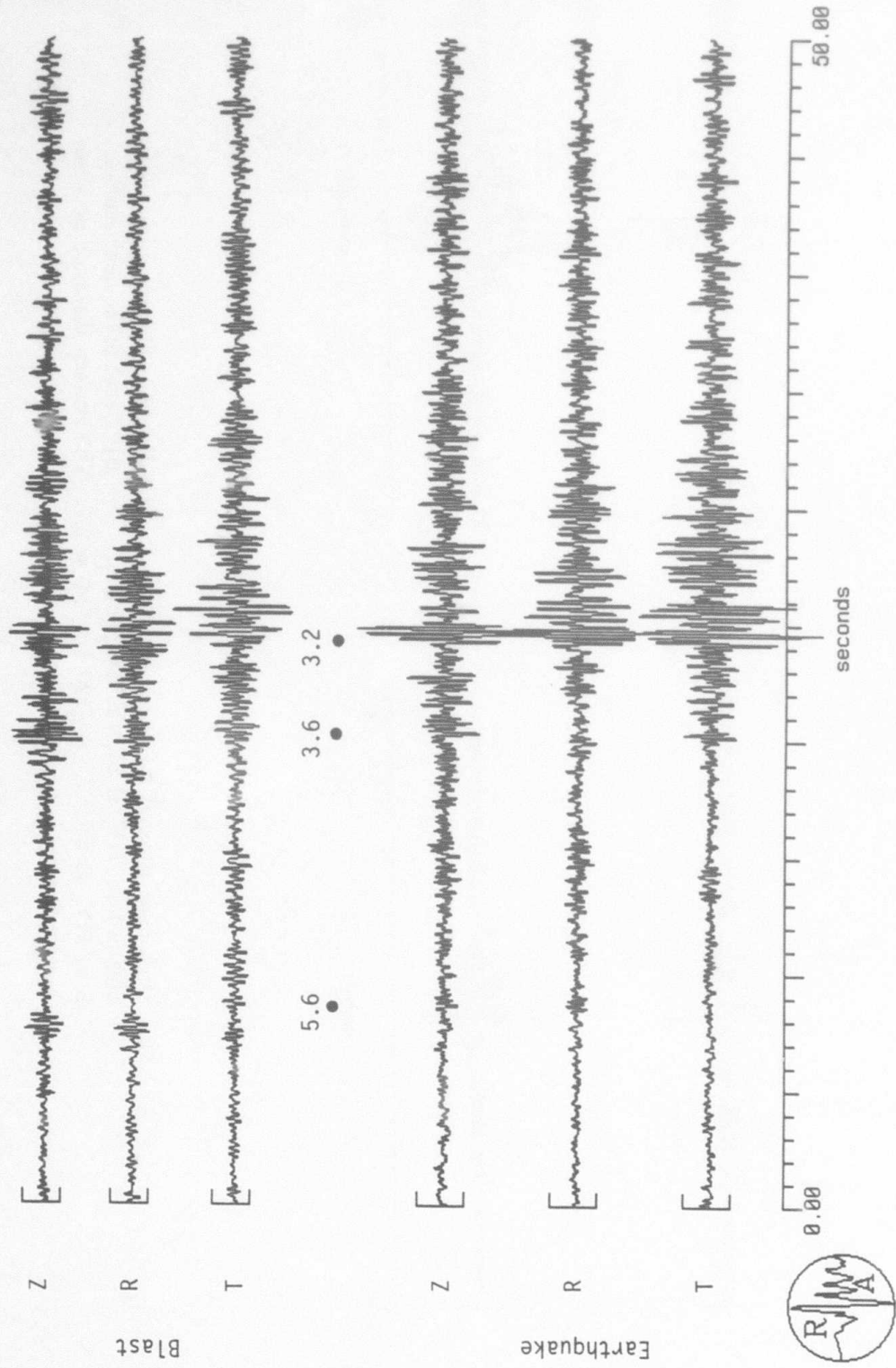
Figure 33. 1 - 5 Hz data. Top three traces are the blast, vertical, radial, and transverse components; bottom three are the earthquake. Group velocities determined for three phases on the earthquake seismograms are indicated.

54
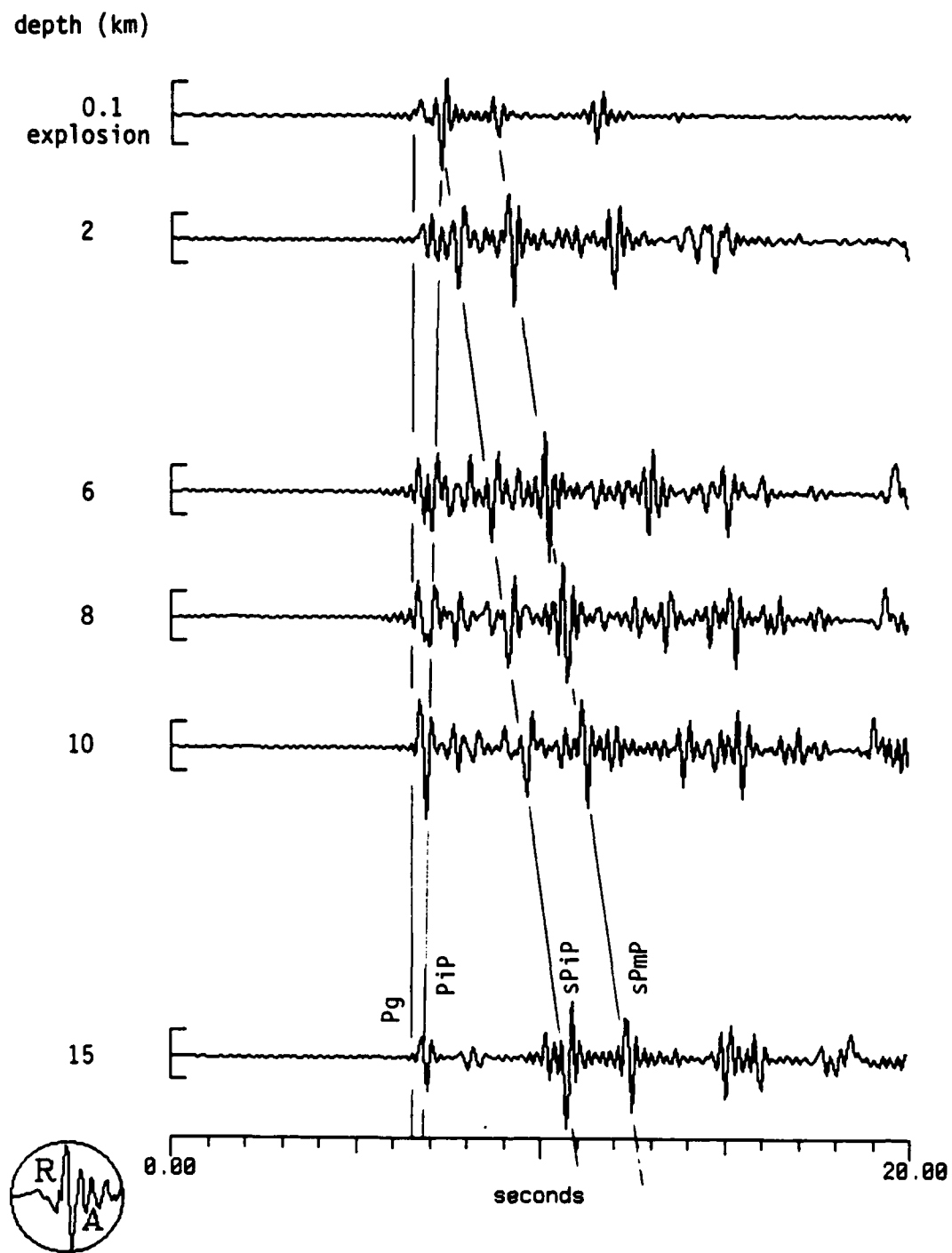
Figure 34. Vertical-component synthetic seismogram depth section for the October 30, 1985, earthquake and an explosion source at the surface. For the earthquake strike=018°, dip=60°, rake=156°. Receiver response=SRNY.
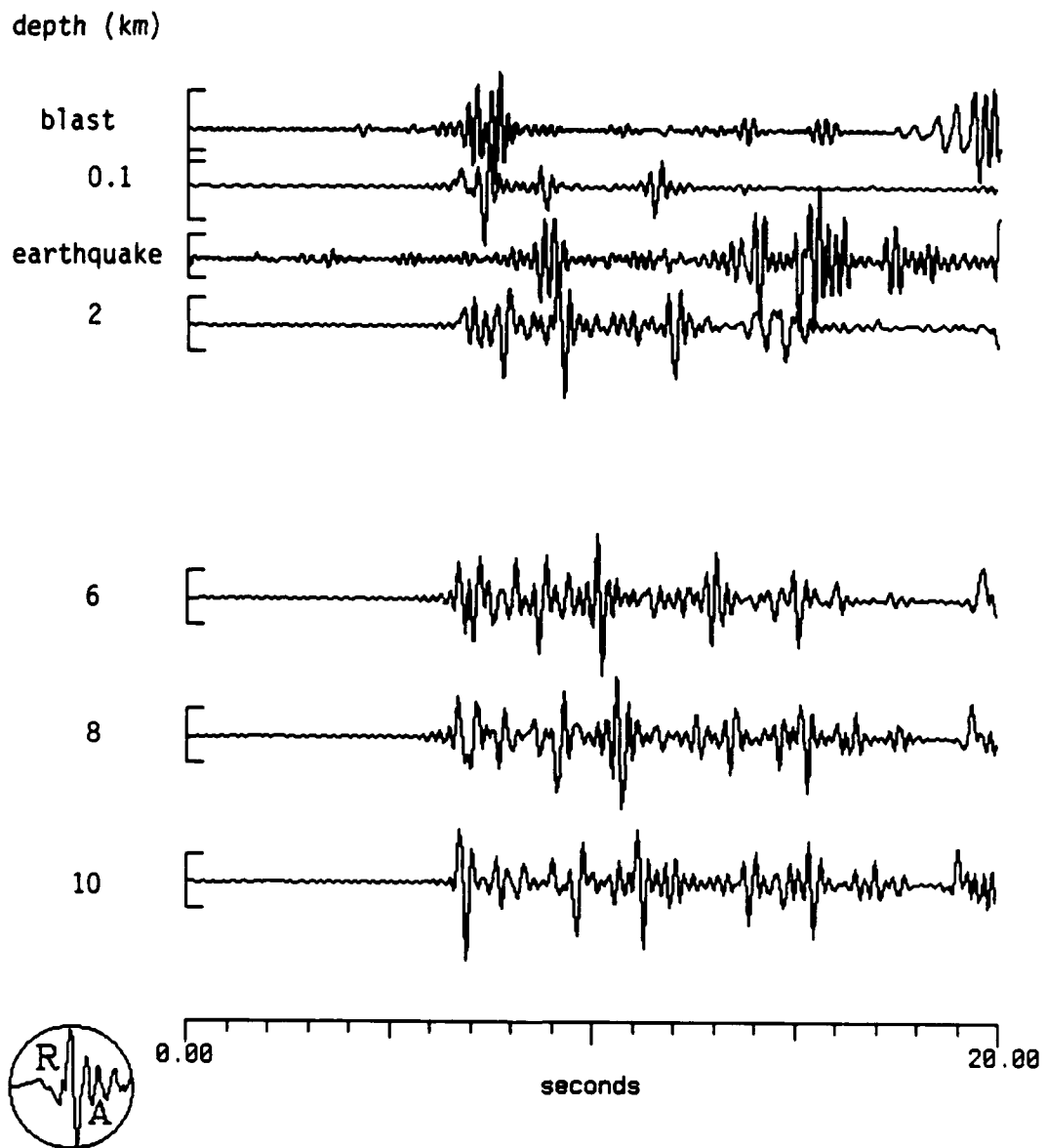
Figure 35. Vertical-component synthetic depth section compared to state-filtered seismograms recorded at SRNY. Top trace is quarry blast. Third from top is the earthquake. For details of the synthetics, see Figure 34.

synthetics. Notice that the first visible *P*-wave is later on the earthquake and has a group velocity of 5.6 km/sec. The earthquake's first *P*-pick at a nearby regional station (WPNY of Lamont-Doherty Geological Observatory's network), however, yields a group velocity of 6.1 km/sec, suggesting that an earlier arrival at SRNY may be masked by noise. Polarization filtering of SRNY data (as seen in Figure 35 with synthetics) improves the strength of rectilinearly polarized signal, but doesn't reveal a clear *P*-arrival earlier than the one with a group velocity of 5.6 km/sec.

A depth-section of vertical synthetic seismograms is shown in Figure 34. The surface (actually 0.1 km) depth was modeled as an explosion, while the remaining depths were modeled as a double-couple mechanism with strike = 018°, dip = 60°, rake = 156°. As mentioned above, no fault-plane solution could be determined from network first motions for the 30 October, 1985 event, so we used a generic mid-Hudson solution that is based on well-constrained data for earthquakes approximately 34 km south of Amsterdam, N.Y. (Houlday *et al.*, 1984). Also, we don't have a velocity model appropriate for travel paths between Amsterdam and Stone Ridge, N.Y. We used the New England model, rather than the Adirondack model, because geologically it is an Appalachian path.

Prominent early arrivals on the synthetic seismograms are *Pg*, *PiP*, *sPiP*, and *sPmP*. Though the synthetics do not match the data in detail, a plausible interpretation is presented in Figure 35. The blast, which, we verified with the quarry, must be a surface source, and the travel times we interpreted in Figure 33 are close to those of the initial two *P*-pulses modeled as a surface explosion. As expected, the blast phase with estimated group velocity = 3.6 km/sec is not accounted for by theory. The first detectable *P*-wave from the earthquake can be interpreted as a depth phase, given its group velocity. If it is *sPmP*, then the earthquake is very shallow. If it is *sPiP*, then, from its travel times, the quake is about 7 km deep. We prefer the shallow depth interpretation (shown in Figure 35) for at least two reasons. First, the nearest network station, ROTD, has a 2 Hz, large-amplitude arrival with a group velocity of approximately 2.8 km/sec. It is probably a fundamental-mode Rayleigh wave, indicative of a shallow source. Second, the depth estimate given by the network hypocentral location is 4 ± 44 km, yet the nearest station is only 20 km away. Such runaway error estimates can arise when the true depth is small relative to epicentral distance to the nearest station. Finally, the earthquake (*Mc* = 2.7) was felt locally by many people (Nottis, personal communication), suggesting a shallow source. Admittedly, more details of intensity effects would be required to discriminate a very shallow focus from a 7 km focus.

There is enough evidence to conclude that the Amsterdam earthquake is shallow, but given uncertainties in faulting mechanism and velocity model, along with a poor signal-to-noise ratio at SRNY, the identification of a depth phase is a bit shaky.

Ardsley, New York, October 19, 1985

The Ardsley earthquake (*M* = 4.0) of October 19, 1985 occurred in southern New York state at 40.98° N, 73.83° W at a depth of 5 km (Figure 4). It was felt in many

areas of New York, New Jersey, Connecticut, as well as Pennsylvania, Massachusetts, and Rhode Island. The largest aftershock ($M = 3.0$) occurred two days later, also at a depth of 5 km. Both the main shock and the aftershock were recorded by station SRNY, 100 km away at 41.85° N, 74.15° W. SRNY is a three-component broadband digital station with a sample rate of 60 samples/second.

A comparison of the main shock and aftershock seismograms from station SRNY (Figure 36) shows a remarkable similarity. The traces have been lined up with the first motion of the aftershock occurring .72 seconds after the first motion of the main shock. The traces match nearly wiggle for wiggle on all three components. The aftershock matches so well with arrivals well into the main shock coda that the main shock must be a complex event with at least one large impulse occurring after the initial impulse.

It is well known that the rupture history of a large seismic event can be extremely complex. Studies of teleseismic body waves have identified multiple ruptures (e.g. Kanamori and Stewart, 1978; Trifunac and Brune, 1970), Doppler shifts (Douglas et al., 1981), body wave directivity functions (Khattri, 1978) and other phenomena as contributors to the complexity of the wavetrain. In contrast, there are relatively few studies (Bakun et al., 1978) that have identified these same complexities in smaller events. In fact, much research has been devoted to understanding the complexity of large events by assuming that small events in the same area, usually aftershocks of the large event, were generated by simple point sources (e.g. Hartzell, 1978; Kanamori, 1979; Frankel and Kanamori, 1983; Mueller, 1985).

We have capitalized on the point-like source behavior below 12 Hz of the aftershock from the 19 October 1985 Ardsley earthquake to deconvolve the main shock using the aftershock as an empirical Green's function. By assuming that the aftershock is a point-source Green's function, the effect of propagation path, recording-site response, and instrument response are eliminated as sources of major error.

The method of using small aftershocks as empirical Green's functions to deconvolve larger events is based on the assumption that the smaller event is a simple source compared to the larger event. The closer the small event source function is to an impulse in time and space, the closer the event approximates the true Green's function.

The main shock displacement can be written as a convolution of the source, path, receiver, and instrument responses at a particular source/receiver geometry.

$$D(t) = S(t) * P(t) * R(t) * I(t) \qquad (10)$$

where * denotes convolution. The Green's function for the same source/receiver geometry is written:

$$G(t) = P(t) * R(t) * I(t) \qquad (11)$$

Thus, by deconvolving (10) with (11), $S(t)$, the far field displacement time history for the source in (10) is obtained.
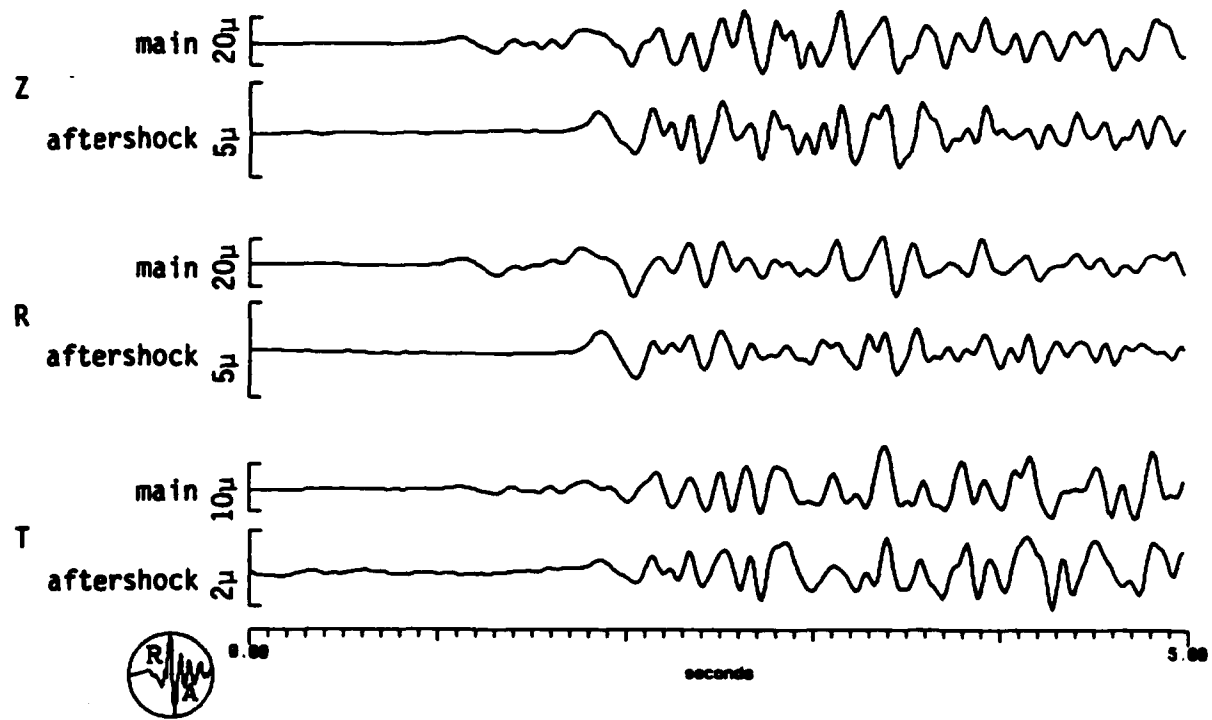
Figure 36. Ardsley, NY, main shock and aftershock. Bandpass filtered 0.5 to 12 Hz and rotated to radial (R) and transverse (T) directions relative to station SRNY, Δ=100 km.

The information gained from a single station can be used in conjunction with the focal mechanism to place some broad constraints upon the fault dimensions. To obtain a complete record of the large fault displacement time history, data from at least three stations are needed. From the time difference between the first and last asperity arrivals, Δt_{tot} a maximum fault dimension (L_{max}) can be determined by assuming fault propagation in the direction of the receiver. The minimum fault dimension (L_{min}) is found from the maximum time difference between two successive asperity arrivals Δt_{max}.

$$L_{min} = \frac{\Delta t_{max}}{V_s^{-1} + V_p^{-1}}$$

$$L_{max} = \frac{\Delta t_{tot}}{V_s^{-1} - V_p^{-1}}$$

(12)

if failure propagation is less than S-wave velocity the use of equations (12) will give larger than the actual dimension.

The assumptions made in this analysis purposely oversimplify the faulting mechanism so that a simple solution may be obtained. The results presented in this report using the above methods agree well with the theoretical fault dimensions calculated using empirical formulas for m_b vs fault dimension derived by Kanamori and Anderson (1975), and with the fault dimension determined by aftershock studies.

Very little processing was necessary to obtain excellent results for the Ardsley events. The data were band pass filtered between 0.5 and 12 Hz with a phase-free filter and then the horizontal components were rotated to the radial and transverse directions for station SRNY before deconvolving. The data were also processed using the adaptive polarization analysis method and the polarization state filter and gave valuable information about the polarization stability of the coda. However, the additional polarization processing did not change the results.

In Figure 37 we show the result of deconvolving the first few seconds of P-wave of the Ardsley earthquake using the 21 October aftershock. The top trace in the plot is the signal from the main shock, the middle trace is from the aftershock and the bottom trace is the deconvolution result. The alignment of the main shock and aftershock traces in the plots is shown as a marker in the deconvolution result.

There are three distinct peaks in this result separated by times of .57 and .15 seconds. The first peak (at −0.75 seconds) corresponds to the alignment of the first arrivals from both events and the third peak corresponds to the best visual alignment of the traces shown in Figure 36. The second peak cannot be easily seen by aligning the traces visually.

Because only one station was used in the analysis presented here, relative locations of the three asperities cannot be determined. However, using equations (12) we obtain
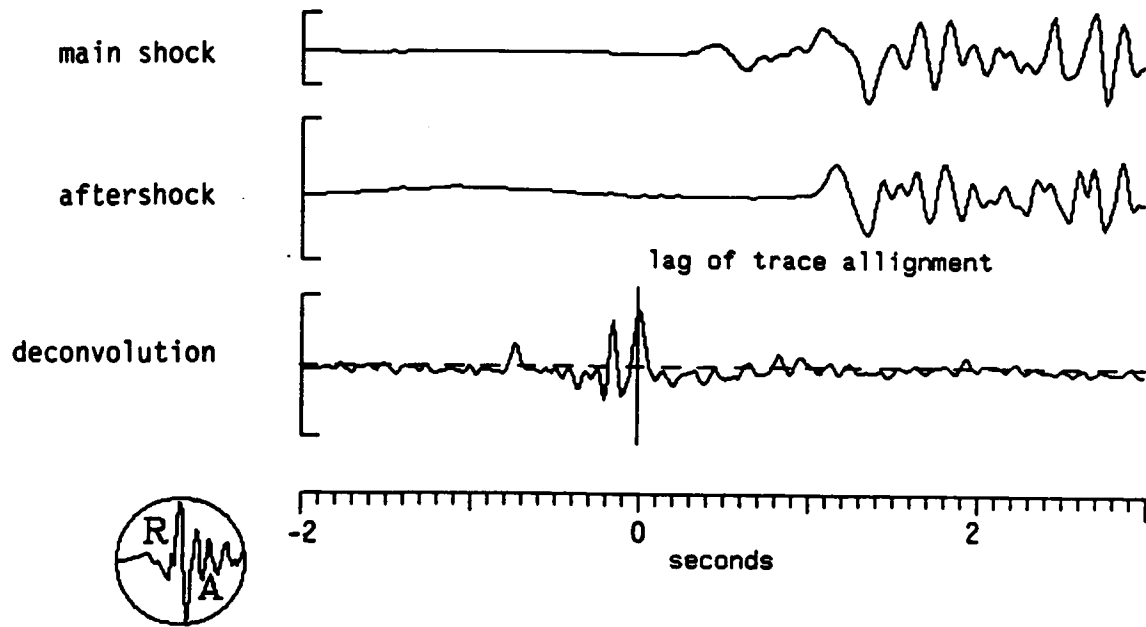
Figure 37. Deconvolution of the Ardsley main shock by its
largest aftershock. The first two arrivals (*Pg*
and *PiP*) as well as the depth phase *sPiP* are
included in the deconvolution operator.
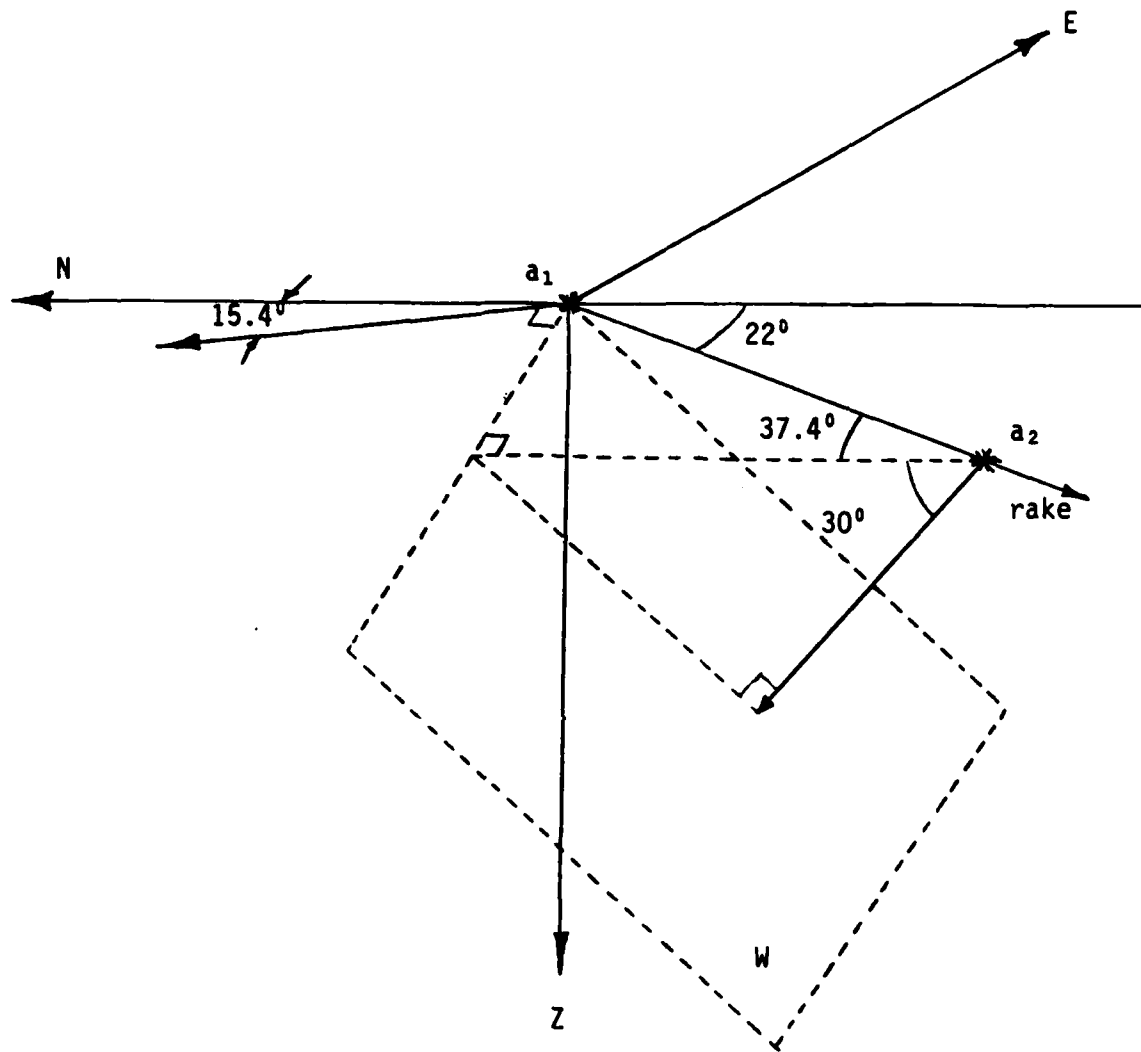
Figure 38. Fault geometry for the Ardsley earthquake.

values of 1.3 and 5.9 km for the minimum and maximum fault dimensions assuming fault propagation at the shear wave velocity. Better estimates of the fault dimension limits can be obtained by using the focal mechanism and assuming that the asperities lie in a line along the direction of the rake. The strike, dip, and rake of the event were reported as 22°, 90°, and 180° respectively by the Lamont Doherty Geological Observatory (Seeber, personal communication). Station SRNY is 0.9 degrees away at an azimuth of −15.4°. At this distance, the wavefront plane dips at about 60°. In Figure 38, the geometry of the fault and wavefront planes are shown. We have assumed that the asperities must all lie along the line of the rake and have let the wavefront plane contain the first asperity. Thus, the distance from the first asperity to the others and then to the wavefront plane divided by the appropriate velocities must equal the time differences between spikes on the deconvolution result. From Figure 38 and equations (12) the minimum and maximum fault dimensions are given by:

$$L_{min/max} = \frac{\Delta t_{max/tot}}{V_s^{-1} \pm \cos(37.4°) \cos(30°) V_p^{-1}} \tag{13}$$

Using $V_p = 6$ km/sec, $V_s = 3.46$ km/sec, and $\Delta t_{max} = 0.57$ sec, the minimum fault dimension is $L_{min} = 1.4$ km and the maximum fault dimension is $L_{max} = 4.1$ km.

Using aftershock hypocentral locations, Seeber et al., (1986) suggest a small source area centered at a depth of 4.5 km and about 1 km in the largest dimension.

Kanamori and Anderson, (1975), provided a theoretical basis for associating the m_b of a small event to the fault length (L).

$$3 \log L \approx m_b - 4.0 \tag{14}$$

From (14) we obtain a fault length of ≈.74 km. The differences in the three fault-length estimates can probably be attributed to the assumptions inherent in the different methods.

Having defined the source time function of the Ardsley main shock with respect to its largest aftershock we now turn to the problem of generating synthetic seismograms for the event.

A suite of synthetic seismograms has been generated for the Ardsley event at the distance and azimuth of station SRNY for comparison to the recorded data. Records were synthesized at source depths of 0, 2, 6, 8 and 10 km up to a frequency of 5 Hz. The New England velocity model (Taylor et al., 1980) and Q structure (Mitchell, 1981) were used.

Because the main shock appears to be the superposition of three sub-events (asperity ruptures) separated in time, it is not appropriate to compare the main shock directly to the suite of synthetics, which were generated assuming a simple Green's function. We

therefore compare the aftershock seismogram to the synthetics. To match the 5 Hz high frequency limit of the synthetics and eliminate microseismic noise, the data were band pass filtered between .5 and 5 Hz prior to the comparison.

The vertical component traces are shown in Figure 39 with the appropriate data trace placed at a depth of 4.5 km. The first three phases to arrive are the Pg, PiP, and $sPiP$ phases illustrated in Figure 40. Phases that are initially downgoing such as PiP arrive earlier as the source depth increases and phases that are initially upgoing, especially depth phases such as $sPiP$, arrive later as the source depth increases. The match of the synthetics to the first three arrivals of the data is quite good although the amplitudes are not well matched. In addition, approximately 3.5 secs after Pg there is a clear phase on the data trace. Most likely it is $sPmP$, though this is not a prominent arrival in the synthetics and synthetic $sPmP$ arrives slightly later for a source depth of 4.5 km.

Station RSNY at 44.548° N 74.530° W is 400 km from the epicenter of the Ardsley event and at nearly the same azimuth as station SRNY (−15.4° vs. −8.0°). It recorded both the main shock and the aftershock discussed above but at a much lower signal-to-noise ratio. Because the synthetic match at station SRNY was excellent and we have a good model for the far field displacement time history along this azimuth, we have attempted to model the data at station RSNY.

A summary of the depth estimates for northeastern events is presented below in Table 5.

TABLE 5				
Source Depths of Northeast U.S. Earthquakes				
Date	Event	Magnitude	Reported Depth	This Study
Oct 07, 1983	Goodnow	5.2 m_b	7,14	10
Jan 19, 1982	New Hampshire	4.5 m_b	3 - 11	6
Oct 11, 1983	Ontario	4.1 m_{bLg}	12	14
Oct 19, 1985	Ardsley	4.0 m_l	5	4.5
Oct 02, 1985	Quarry	2.3 m_c	0	0
Aug 31, 1982	Adirondack	2.6 m_n	?	7
Oct 23, 1984	Adirondack	3.4 m_c	?	12
Oct 30, 1985	Amsterdam	2.7 m_c	?	1
May 29, 1983	Maine	4.2 m_b	2	12

The suite of synthetics for RSNY were generated using a point source at depths of 0, 2, 4, 6, 8, 10 and 12 km. The results were then convolved with an approximation to the far field displacement time history so that a comparison could be made with the data (Figure 41). The vertical data recorded at RSNY in Figure 41 are placed at the depth
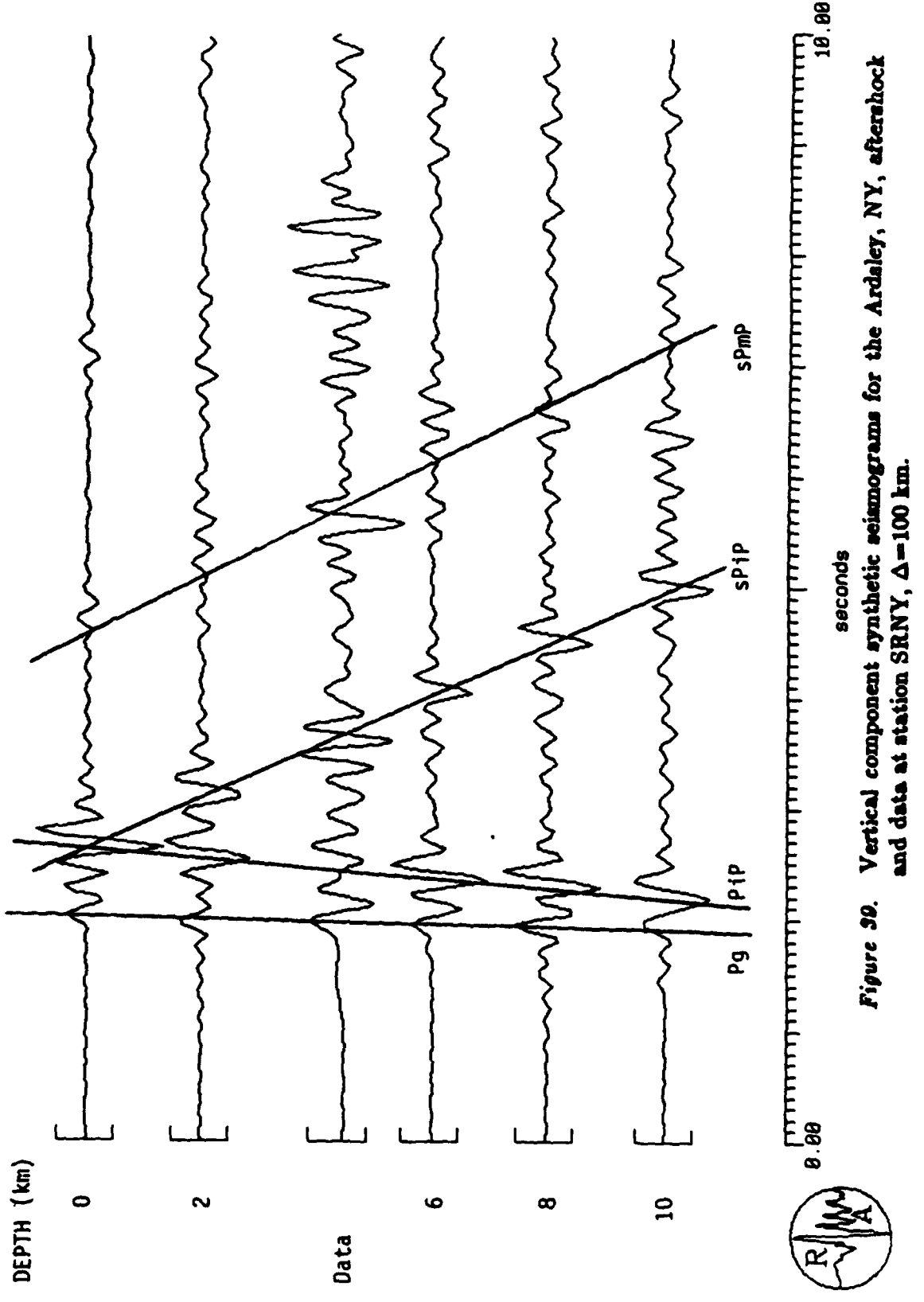
Figure 59. Vertical component synthetic seismograms for the Ardsley, NY, aftershock and data at station SRNY, Δ=100 km.

65
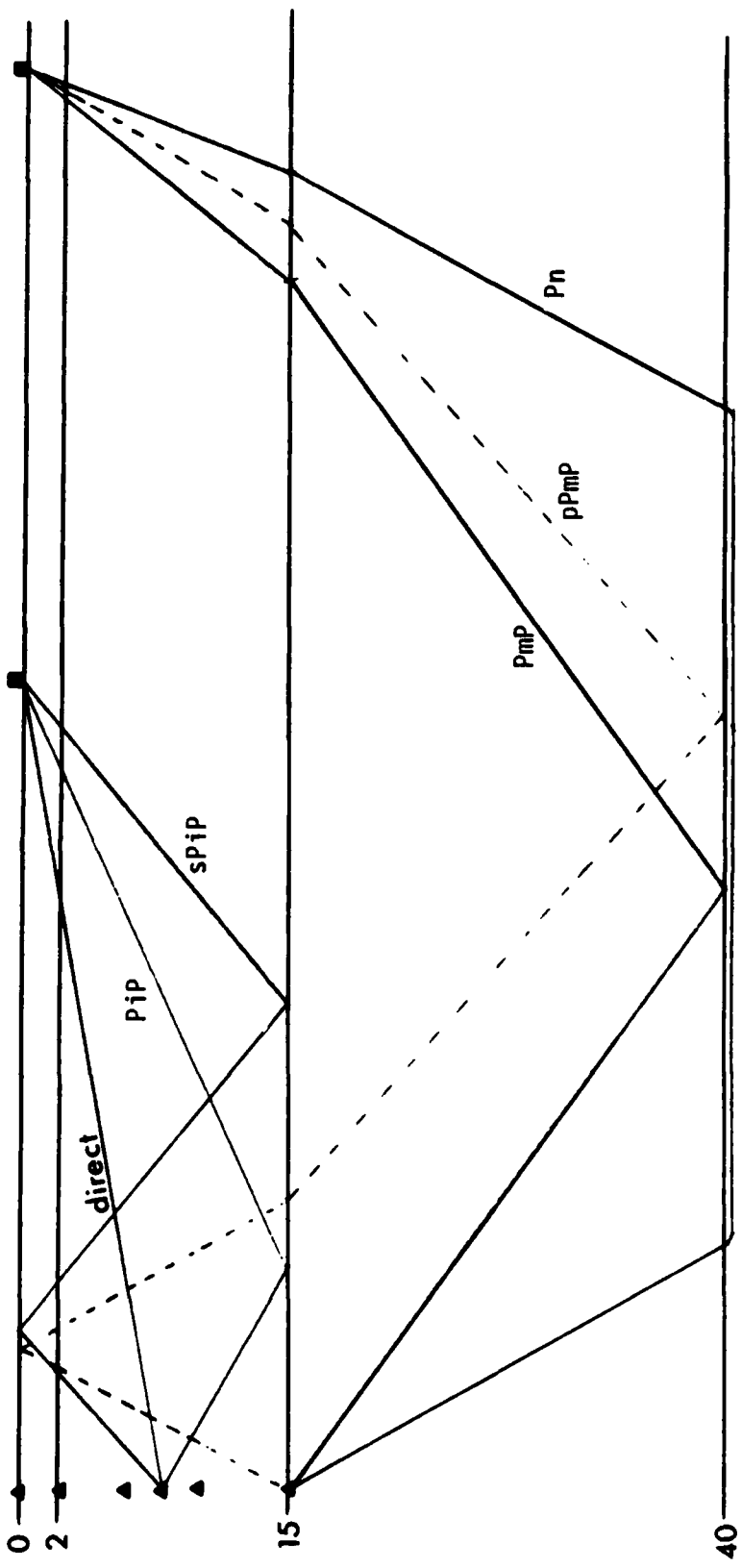
Figure 40. Ray paths of the primary and depth phases.
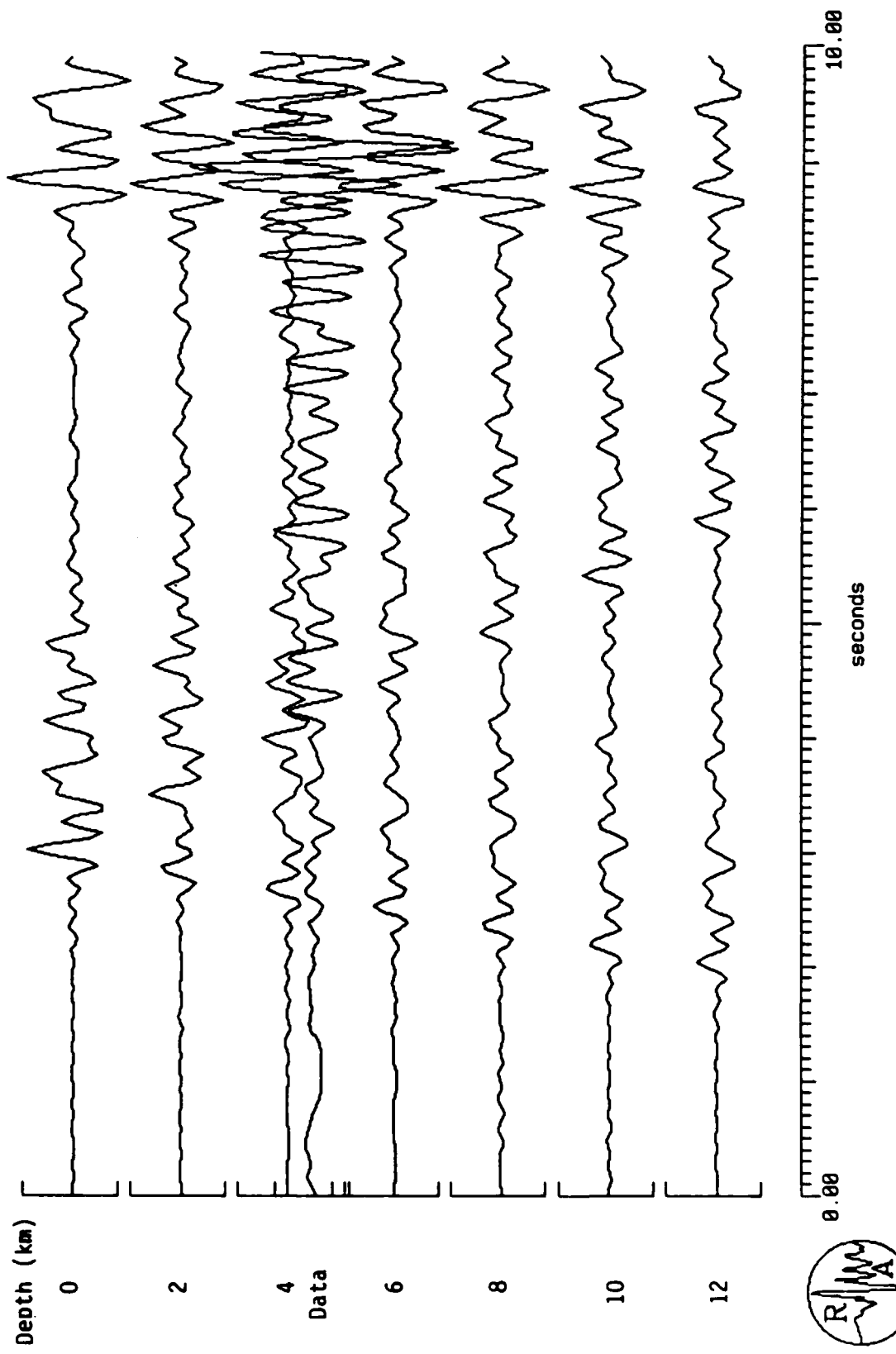
Figure 41. Vertical component synthetic seismograms for the Ardsley, NY, main shock at station RSNY, Δ=400 km.

determined from comparison of the synthetics and data at SRNY (4.5 km). Although noisy, the fit of the data to the synthetics is good. The depth phases are very well matched between seconds two and five as is the arrival at second nine. What has not been modeled is the high amplitude coda between these two sets of arrivals. This may be the effect of scattering, multipathing, or the simplicity of the synthetic model.

Kuril/Kamchatka Data

The Kuril/Kamchatka data will be discussed collectively rather than event by event as was done for the northeast U.S. data. The event and OSS-IV locations are shown in Figure 7. Sixteen events were studied, of which fourteen were assigned depths (Table 3). All of the events are above magnitude 4.5 and range in distance from 574 km to 1307 km from OSS-IV.

The OSS instrument was emplaced 380 m below the sea floor in 5467 m deep ocean. The primary motivations for placing the instrument in a borehole are to enhance the coupling of the instrument and to remove the sensors from the noisy sea-bottom environment. Soft sediments at the ocean bottom have strong shear-wave velocity gradients, which trap shear-wave energy close to the sea-floor interface. By installing the sensors well below the sea floor, the shear wave noise is avoided. Unfortunately, being well below the sea floor interface can complicate the receiver site effects. At typical compressional wave sediment velocities (2.0 km/sec) the travel time from the instrument to the sea-floor interface and back is 0.38 seconds. The two-way travel time for the sea-surface reflection is 7.7 seconds. The sea-surface reflection is the strongest of the two (Figure 42-59). As seen from the data, the prominent sea-surface reflection would make any depth phase arriving near 7.7 seconds difficult to identify. A pP phase arriving at 7.7 seconds corresponds to an event depth of about 23 km.

For the northeastern U.S. data, adaptive polarization analysis was used to help identify phases. The apparent angle of incidence trace identified arrivals with similar phase velocities and the RZ trace helped identify true arrivals. The unusual location of OSS-IV, beneath the sea floor, makes use of adaptive polarization analysis suspect. A strong sea-bottom reflection adds downgoing arrivals to the usual upgoing waves. The apparent angle of incidence trace would then become useless and the RZ trace would indicate both P and SV type motion. Event K1 (Figure 43 and 44) is an example of this type of event. During the initial arrivals, the RZ trace is both positive and negative (usually a sign of Rayleigh type motion) and the apparent angle of incidence trace is confused. In contrast, the sea-surface reflection, which does not include the sea-bottom reflections, has stable negative apparent angle of incidence and RZ trace.

Events with a large signal-to-noise ratio, K1, K3, K4, K5, K6, K7, K10, K11, and K18 all exhibit a common character in the first part of the wavetrain. The first arrival is generally small and is followed by three or more arrivals with increasingly large amplitudes in the next two seconds. The later arrivals could be either depth phases (pP, sP), source effects, or receiver site effects. The reported depths of the events eliminates depth phases as the source of these arrivals for all but the K7 event (6 km depth). If the

arrivals are due to source effects then a remarkably consistent source mechanism would be required for all of these events. Although source effects are certainly present in the data, the regularity of the arrivals over so many events strongly suggests that they are caused by site effects. The additional arrivals are also present in the sea-surface reflection.

Uncertainty in the amount of skew correction, problems associated with the location of the OSS and lack of good long range synthetics made depth determination for this data set extremely difficult. Four different seismologists with varying degrees of observational experience independently evaluated the data for depth and obtained consistent picks for only one of the 16 events (Table 6). Ironically, that event, K5, has no published depth. The depth determined by the observers for K5 was about 16 km.

TABLE 6
Differences in Travel Times Between the First Arrival and the First Identifiable Depth Phase as Picked by Four Analysts for the Kuril/Kamchatka Data

Event	Analyst #1	Analyst #2	Analyst #3	Analyst #4
K1	4.7	2.9	11.8	11.9
K3	3.5	3.6	5.0	7.4
K4	3.2	5.4	14.0	10.0
K5	5/5.5	5.4	5.7	5.4
K6	3.8	2.9	13.0	3.0
K7	3.5	2.9	13.0	13.0
K8	2.2	5.4	13.0	1.25
K10	3.2/5.3	4.6	2/3.9	10.7
K11	4.0	2.1/14.6	6.9	13.9
K12	5.5	5.7	2.1/3	2.2
K14	8.0	5.7	.8/9/16.2	4.1
K15	5.5	4.6	4.8	3.9
K16	4.8	4.6	9.5/10.6	11.3
K18	8.0	5.4	2.3/11	6.6
K19	4.7	3.2	5.6	9.0
K20	2.9	2.9	?	5.2
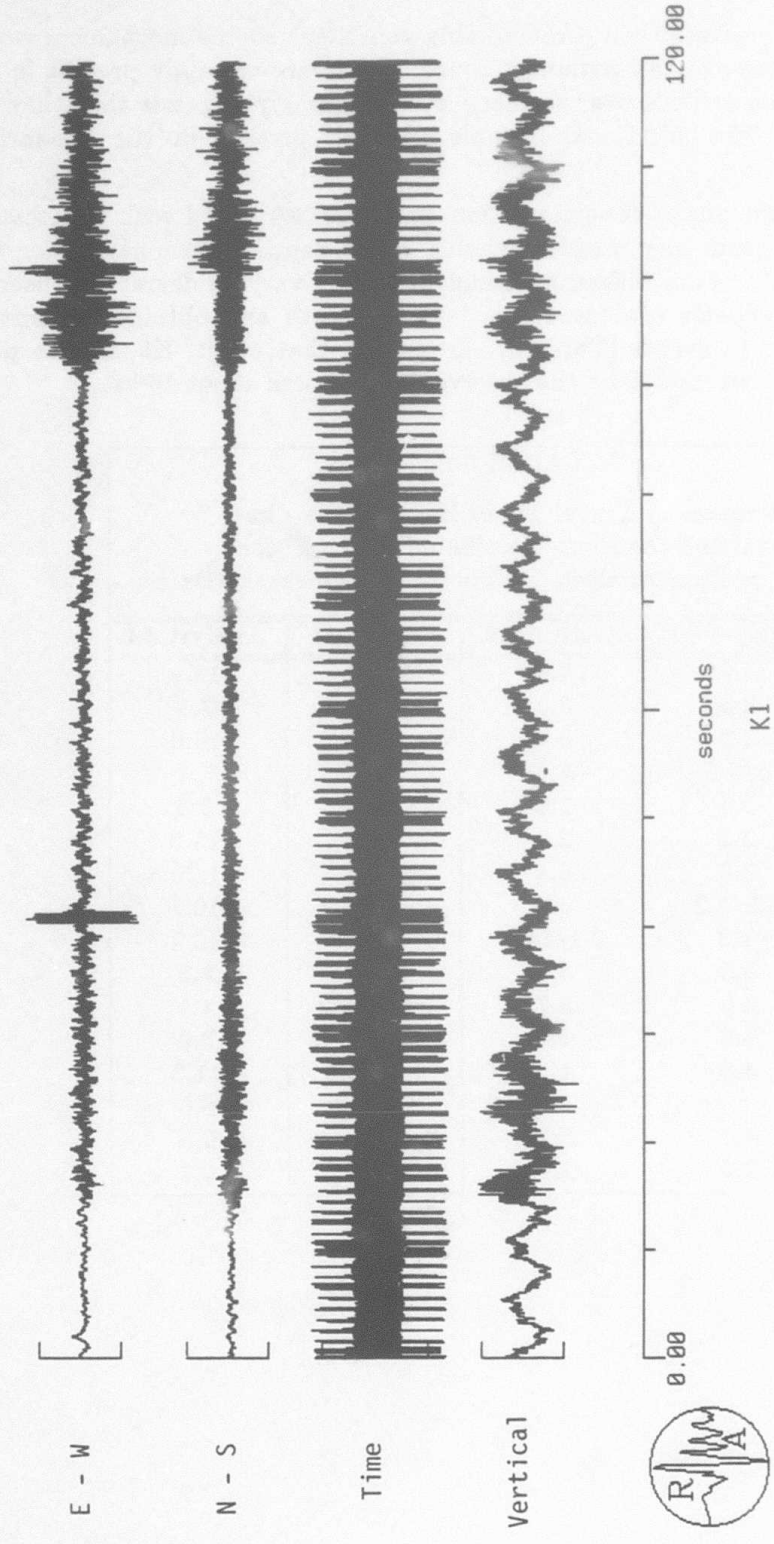
Figure 42. 120 seconds of unfiltered data from OSS-IV for event K1, Δ=861 km. Large bursts on the East-West trace at seconds 40 and 100 are minute marks that are used for skew correction.
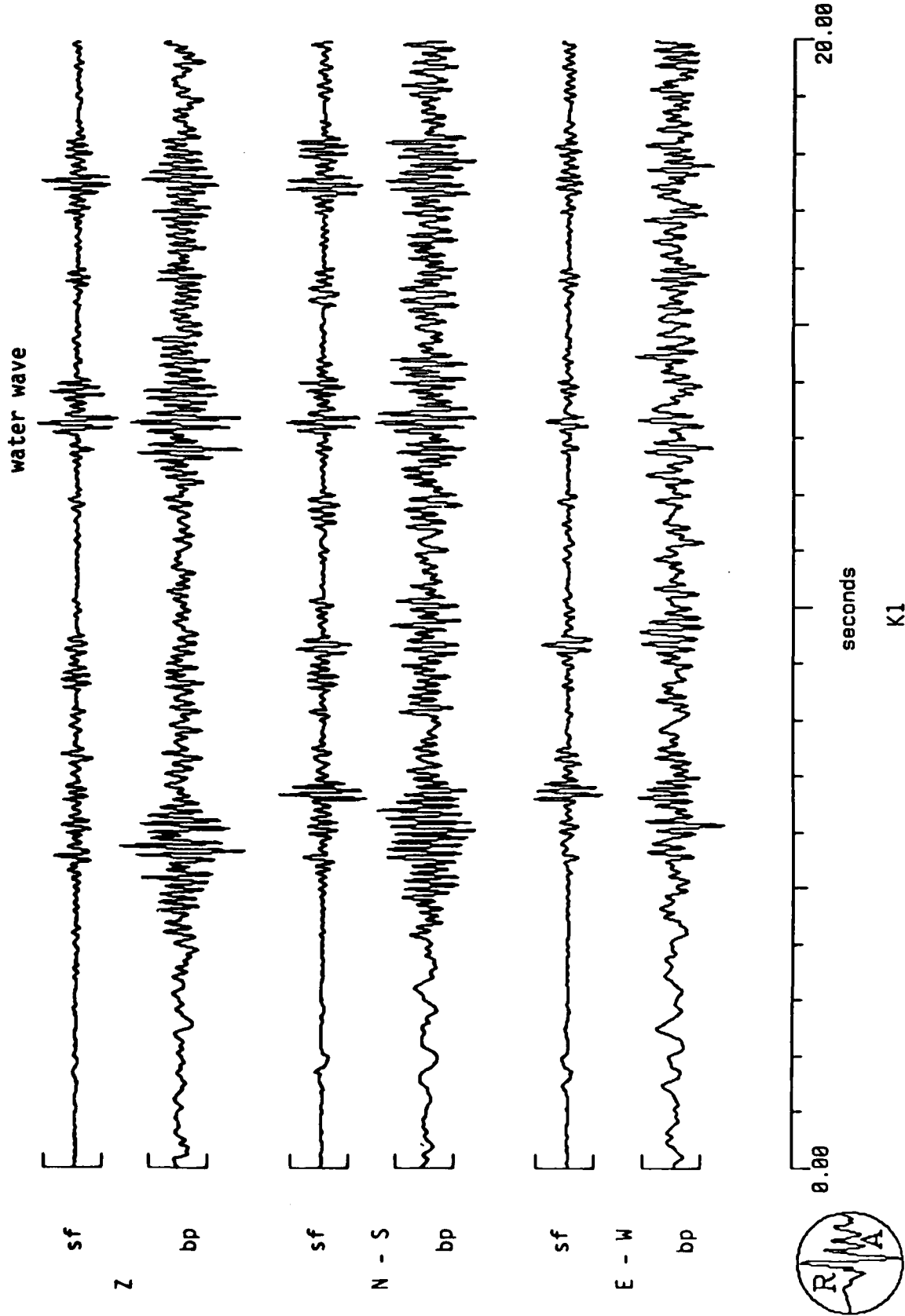
Figure 48. State filtered (sf) and band-pass filtered (bp) *P*-wave data for event K1, Δ=861 km. The band-pass filter passed frequencies between 2 and 15 Hz. The polarization state filter was applied to the band-passed data and passed rectilinear motion.
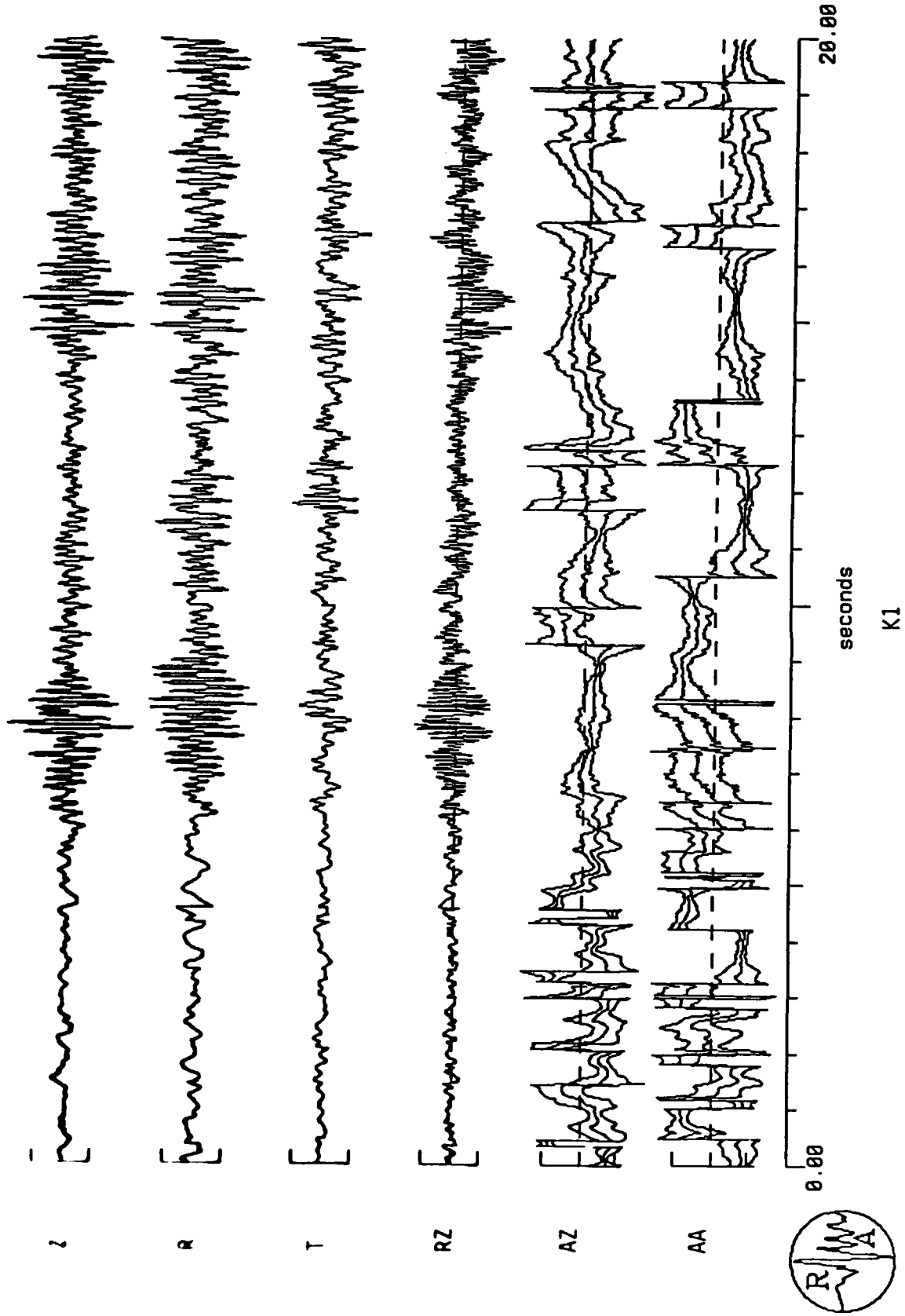
Figure 44. Adaptive polarization analysis of event K1, Δ=861 km. The rapid change in sign of the RZ trace for the first arrival group indicates both up- and downgoing waves. In the water wave arrival (beginning at second 14) the sign is negative indicating downgoing waves. The downgoing waves in the first arrival group are from the sea-bottom reflection.
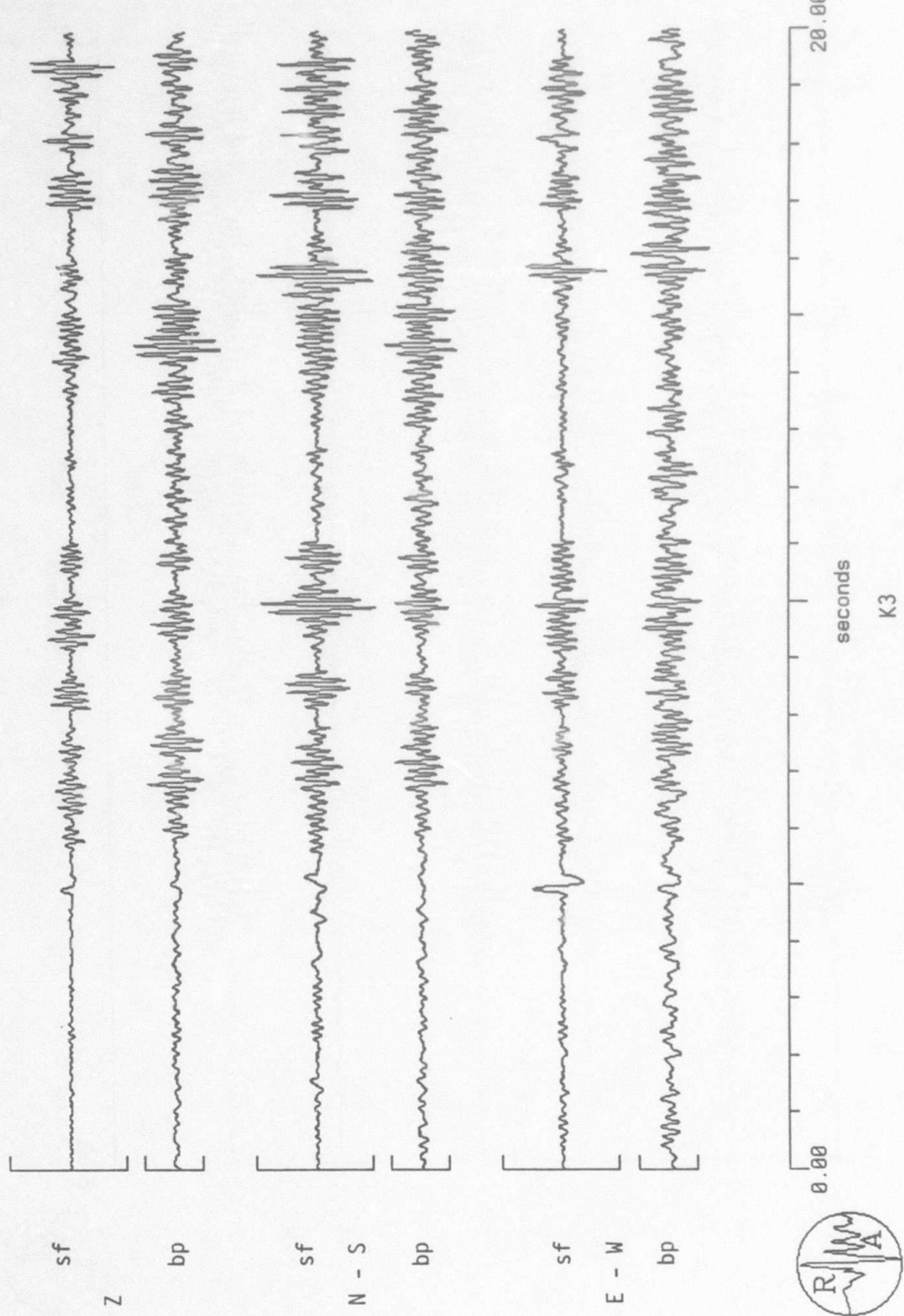
Figure 45. State filtered (sf) and band-pass filtered (bp) *P*-wave data for event K3, Δ=1157 km. The band-pass filter passed frequencies between 2 and 15 Hz. The polarization state filter was applied to the band-passed data and passed rectilinear motion.
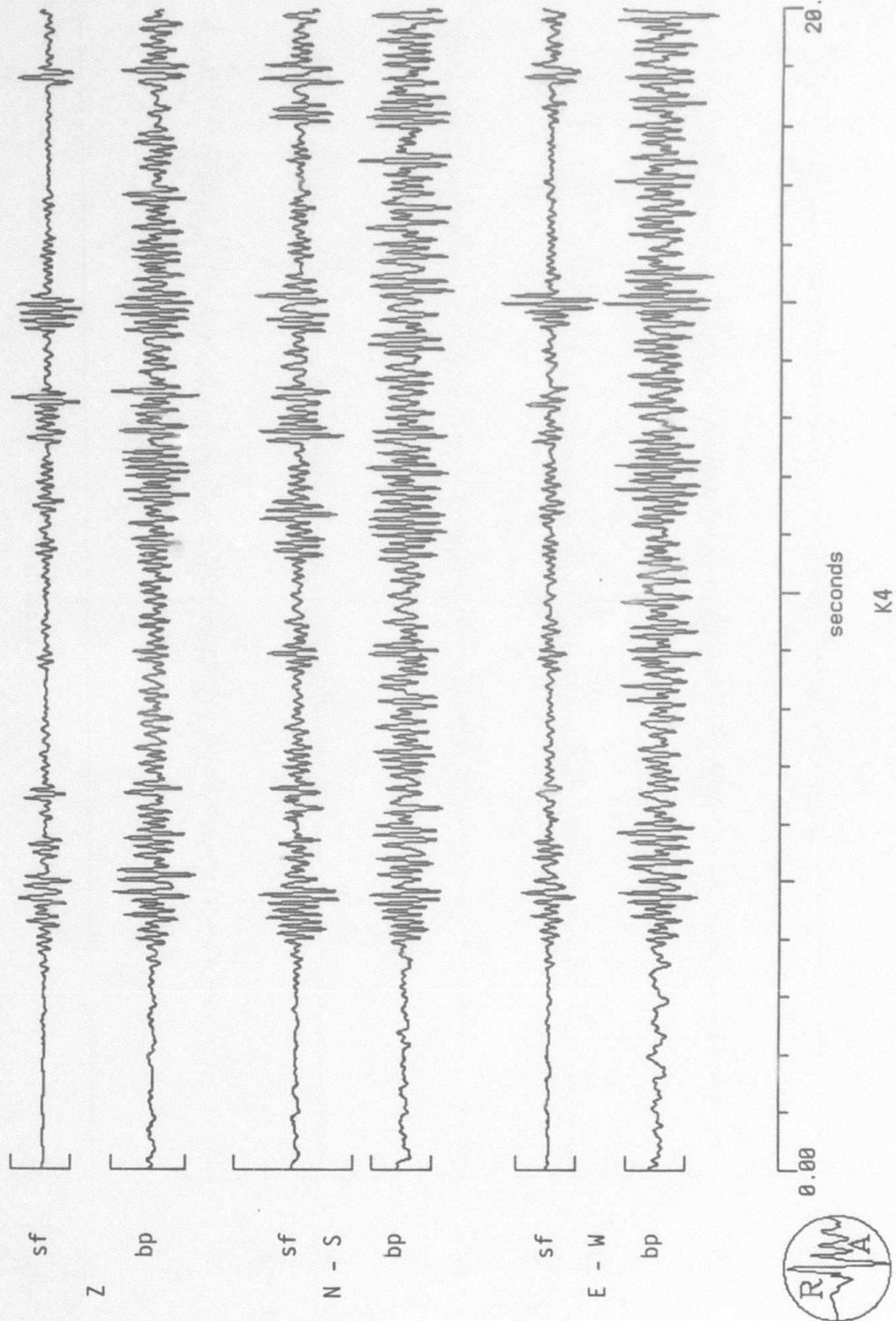
Figure 46. State filtered (sf) and band-pass filtered (bp) *P*-wave data for event K4, Δ=605 km. The band-pass filter passed frequencies between 2 and 15 Hz. The polarization state filter was applied to the band-passed data and passed rectilinear motion.

74
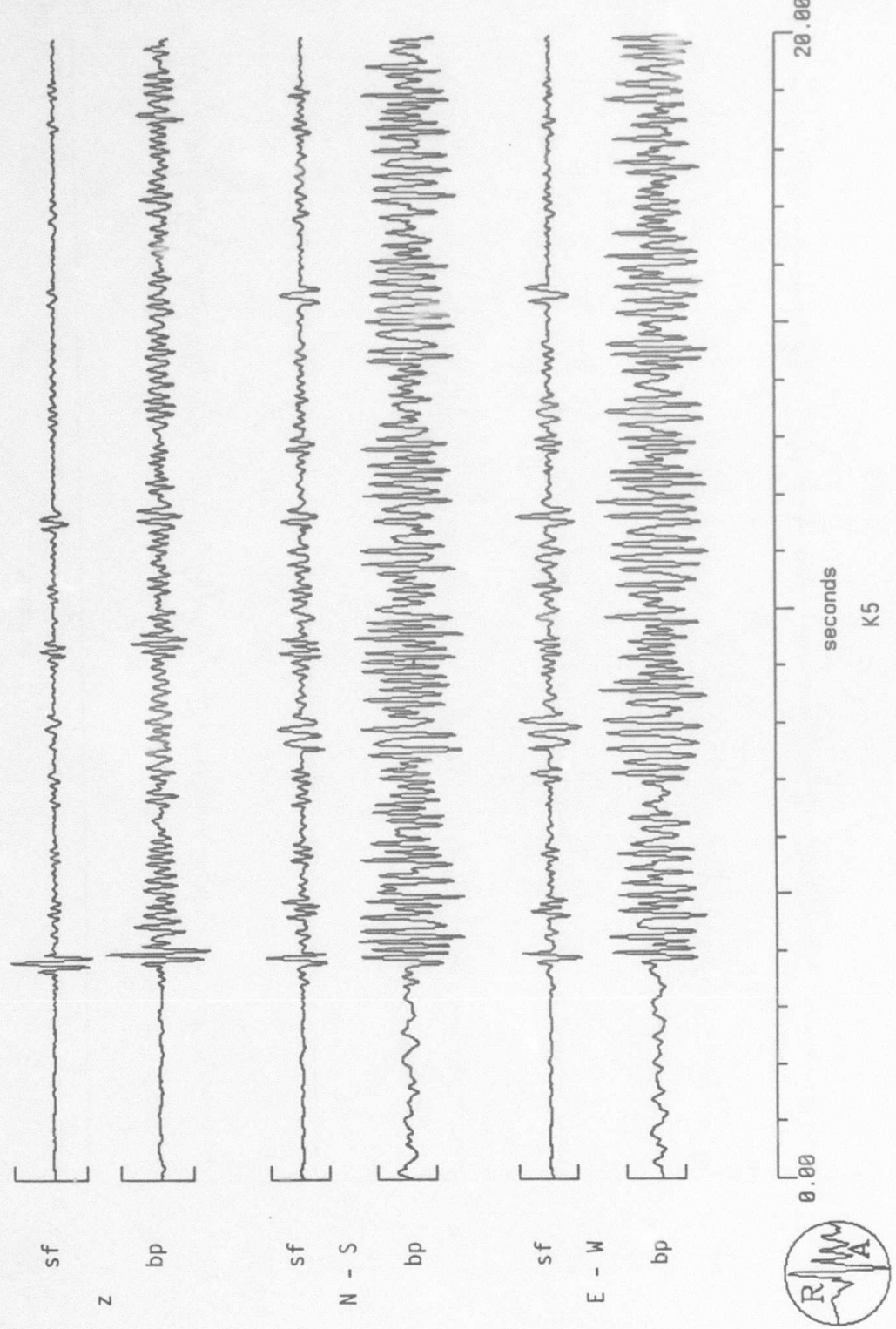
Figure 47. State filtered (sf) and band-pass filtered (bp) *P*-wave data for event K5 Δ=668 km. The band-pass filter passed frequencies between 2 and 15 Hz. The polarization state filter was applied to the band-passed data and passed rectilinear motion.
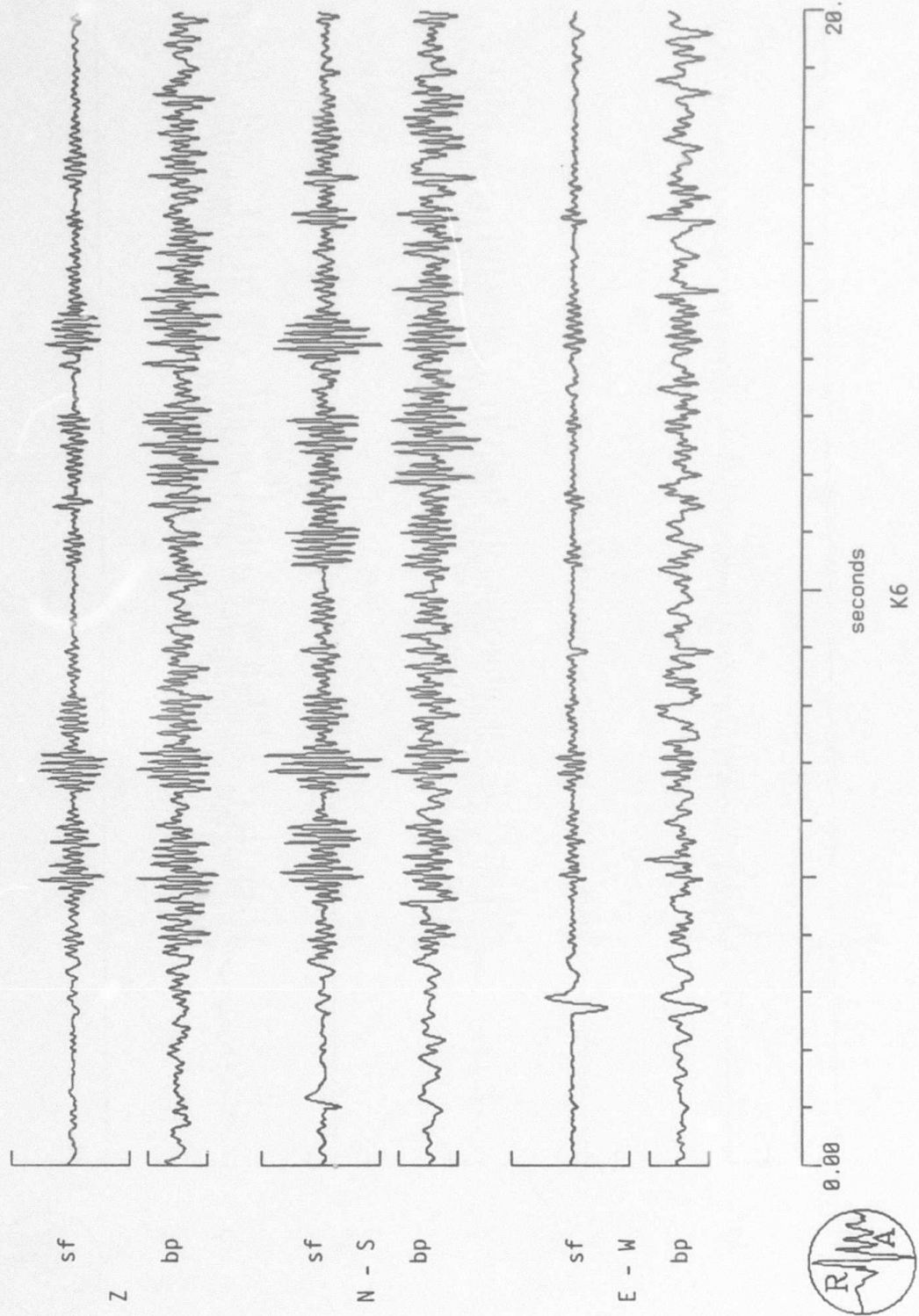
Figure 48. State filtered (sf) and band-pass filtered (bp) *P*-wave data for event K6, Δ=948 km. The band-pass filter passed frequencies between 2 and 15 Hz. The polarization state filter was applied to the band-passed data and passed rectilinear motion.
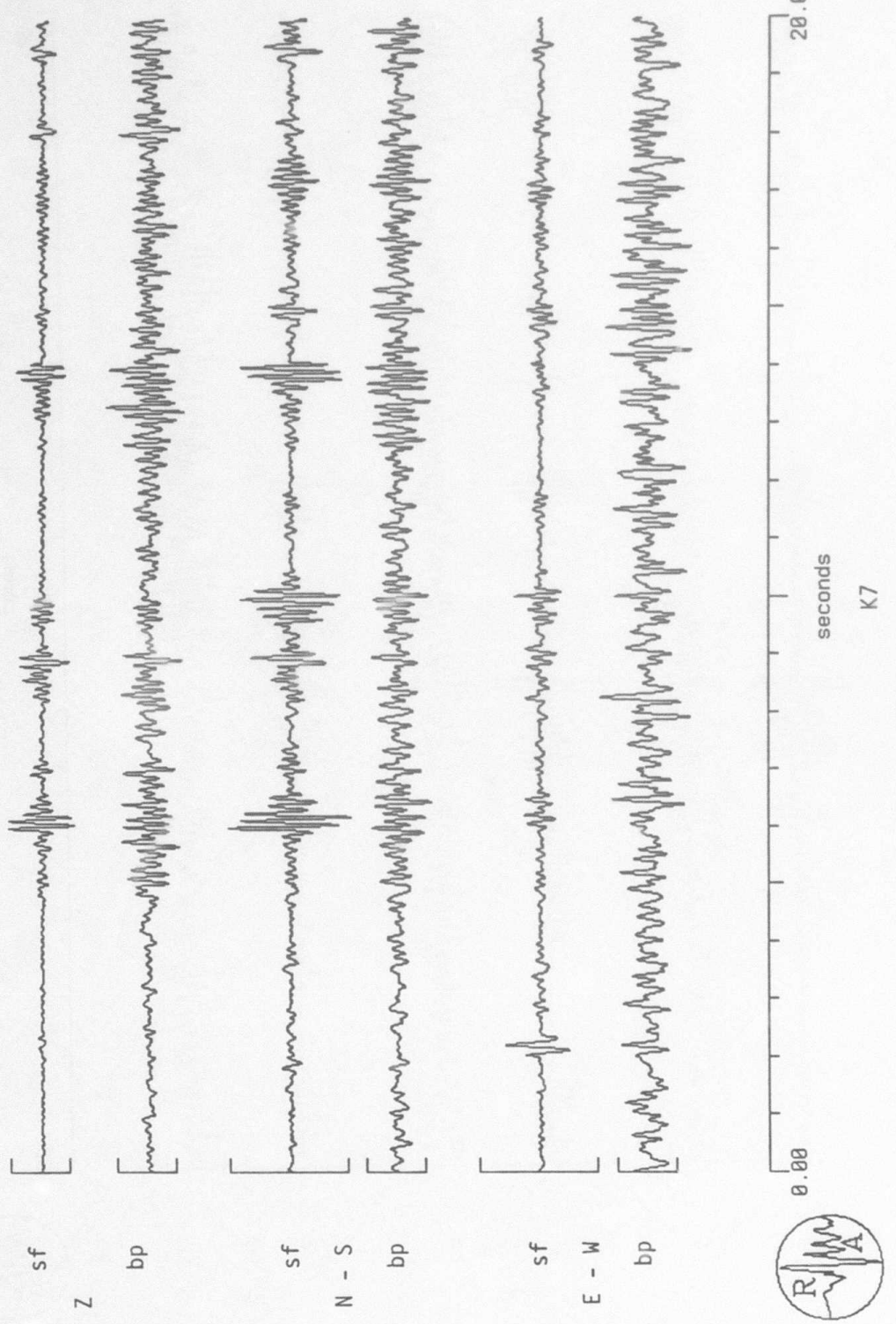
Figure 40. State filtered (sf) and band-pass filtered (bp) *P*-wave data for event K7, Δ=949 km. The band-pass filter passed frequencies between 2 and 15 Hz. The polarization state filter was applied to the band-passed data and passed rectilinear motion.

77
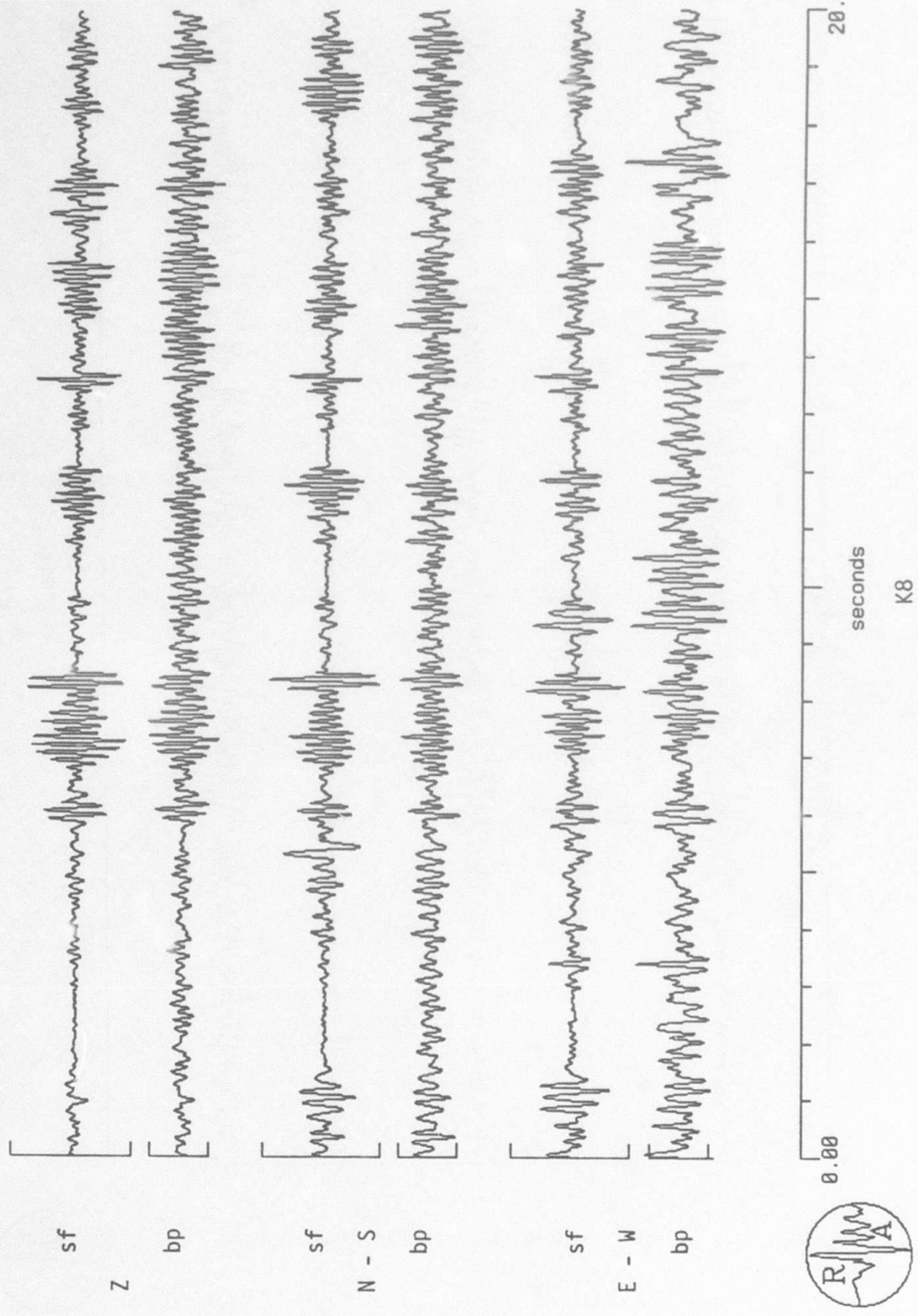
Figure 50. State filtered (sf) and band-pass filtered (bp) *P*-wave data for event K8, Δ=946 km. The band-pass filter passed frequencies between 2 and 15 Hz. The polarization state filter was applied to the band-passed data and passed rectilinear motion.

seconds

K8
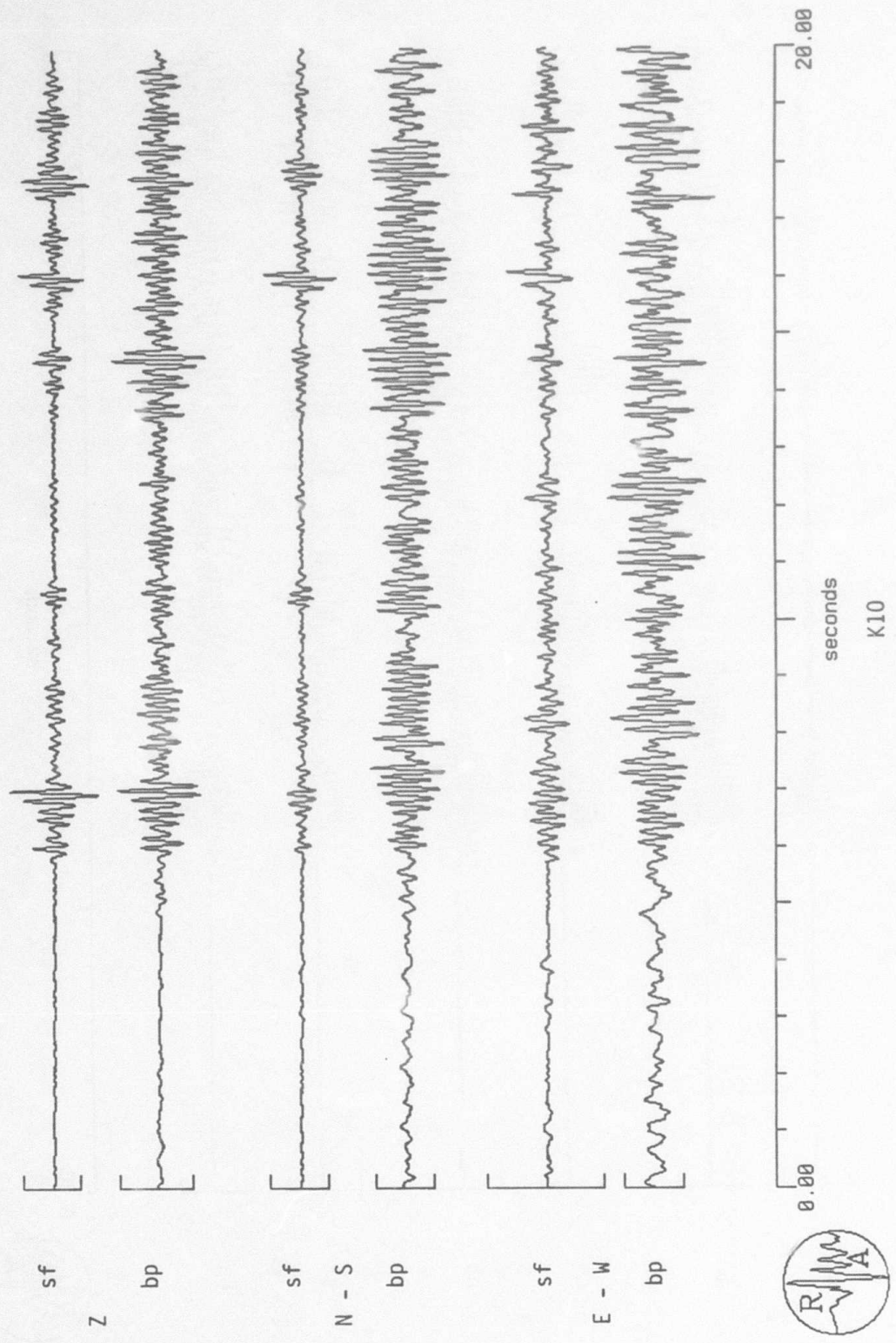
Figure 51. State filtered (sf) and band-pass filtered (bp) *P*-wave data for event K10, Δ=918 km. The band-pass filter passed frequencies between 2 and 15 Hz. The polarization state filter was applied to the band-passed data and passed rectilinear motion.

79
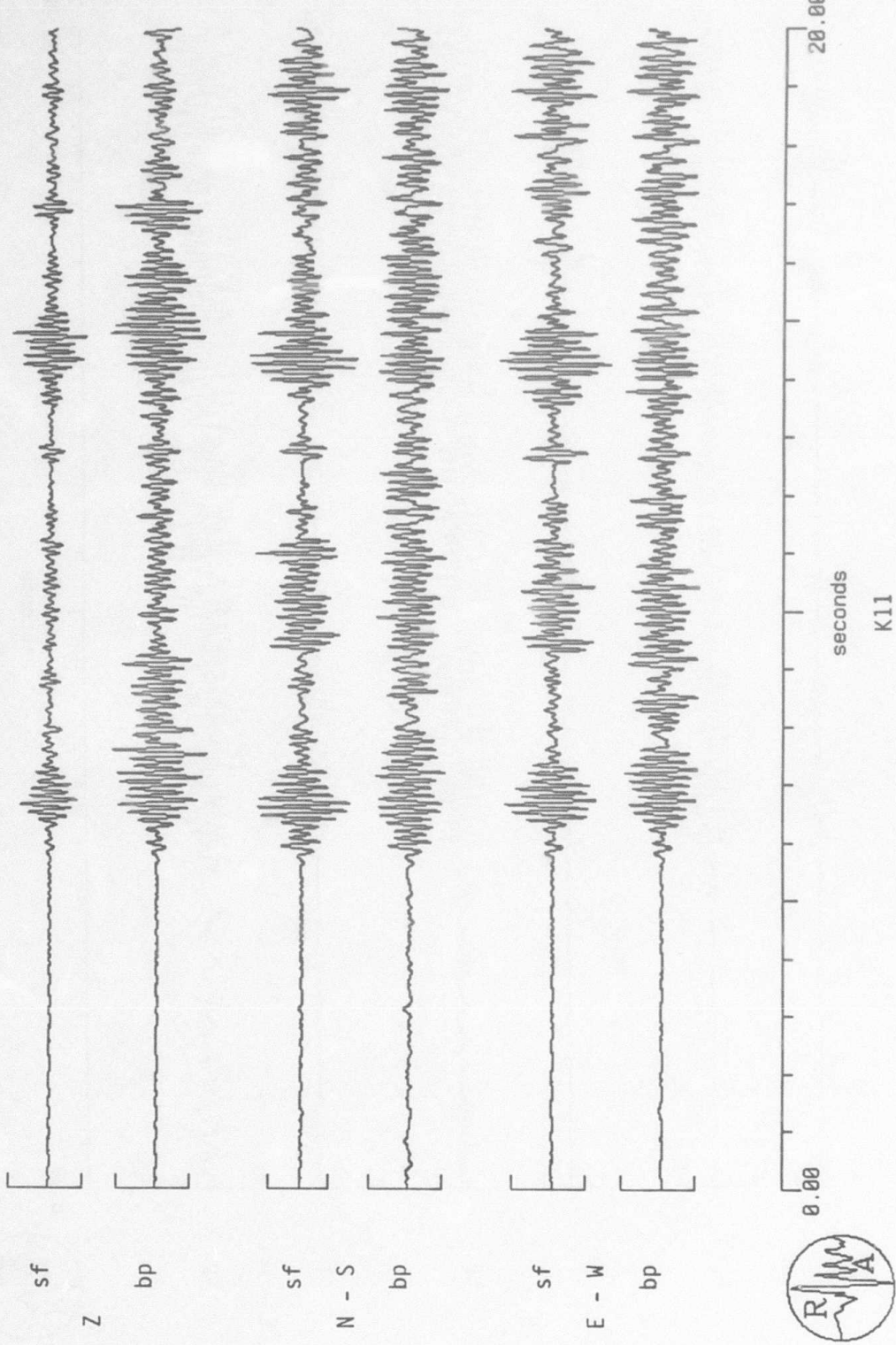
Figure 52. State filtered (sf) and band-pass filtered (bp) *P*-wave data for event K11, Δ=574 km. The band-pass filter passed frequencies between 2 and 15 Hz. The polarization state filter was applied to the band-passed data and passed rectilinear motion.
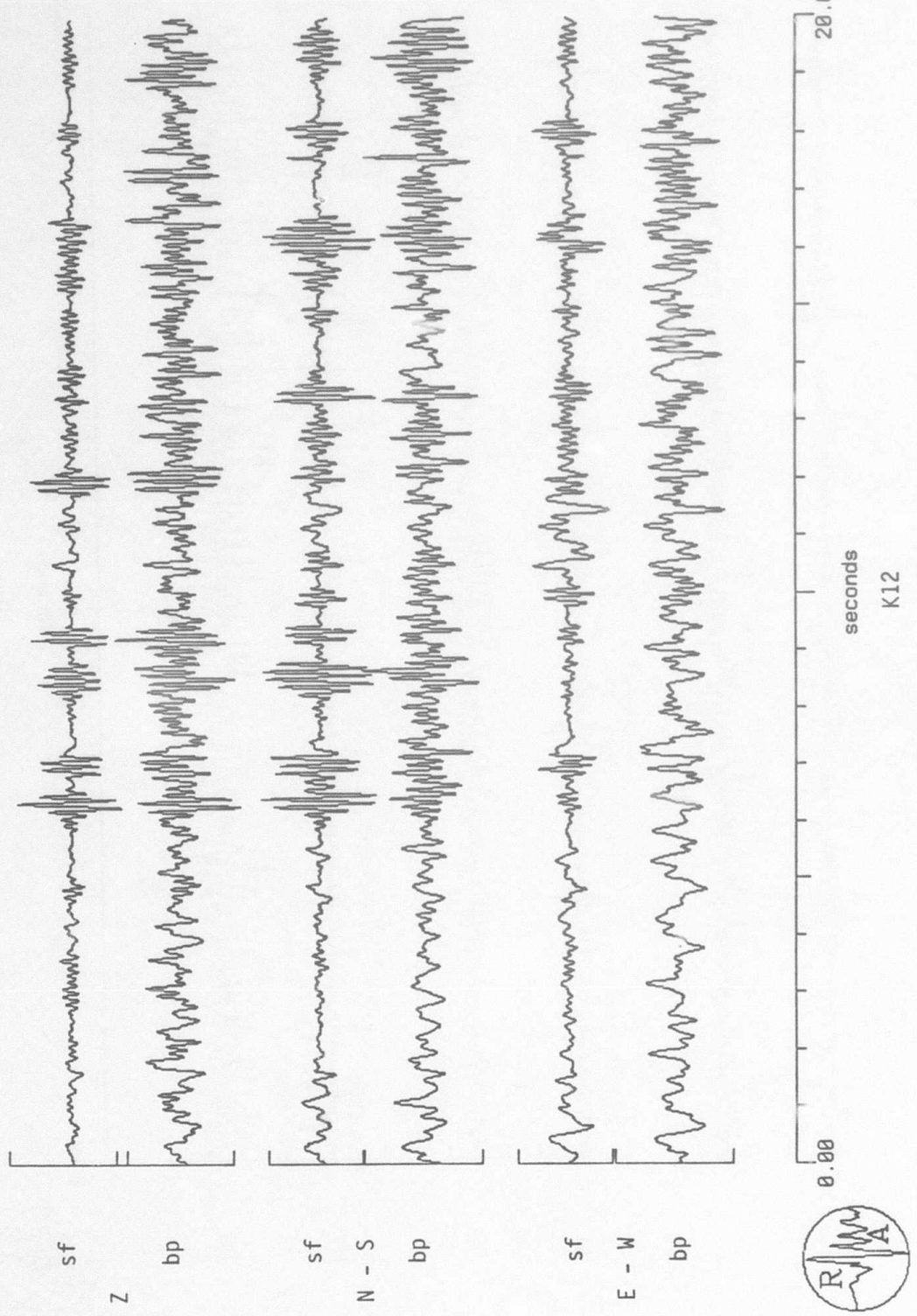
Figure 53. State filtered (sf) and band-pass filtered (bp) *P*-wave data for event K12, Δ=795 km. The band-pass filter passed frequencies between 2 and 15 Hz. The polarization state filter was applied to the band-passed data and passed rectilinear motion.

81
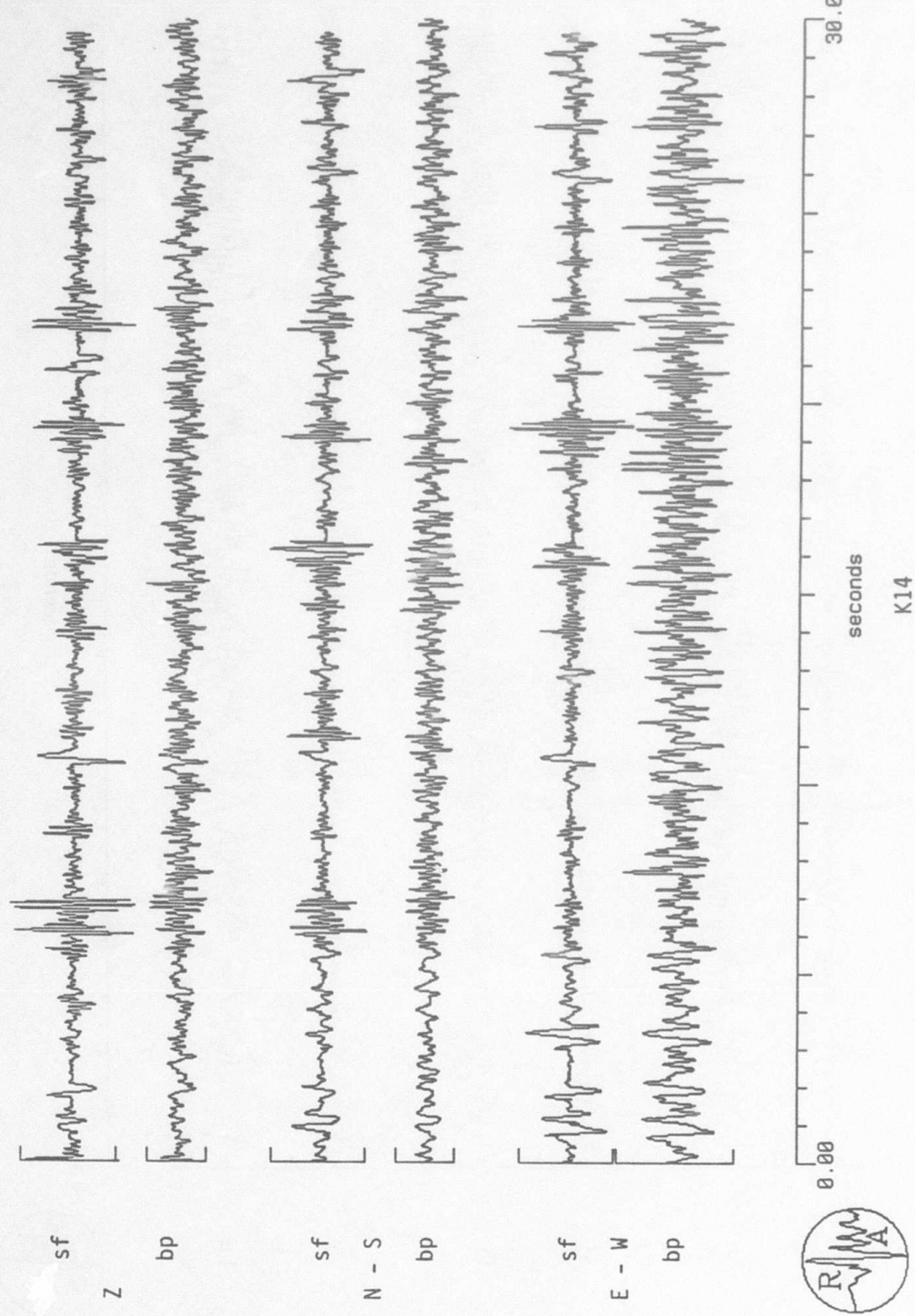
*Figure 54.* State filtered (sf) and band-pass filtered (bp) *P*-wave data for event K14, Δ=753 km. The band-pass filter passed frequencies between 2 and 15 Hz. The polarization state filter was applied to the band-passed data and passed rectilinear motion.
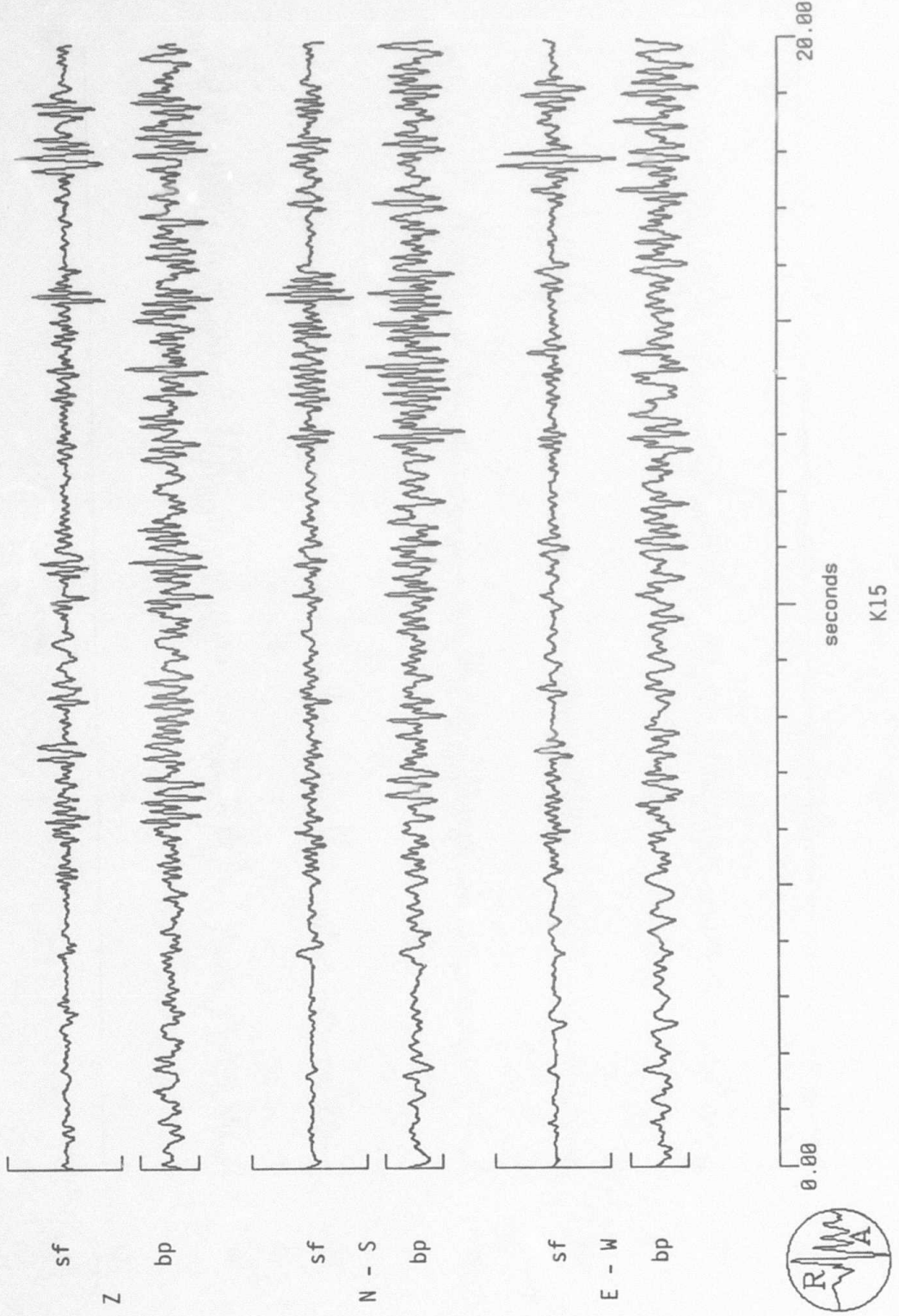
Figure 55. State filtered (sf) and band-pass filtered (bp) *P*-wave data for event K15, Δ=1260 km. The band-pass filter passed frequencies between 2 and 15 Hz. The polarization state filter was applied to the band-passed data and passed rectilinear motion.

83
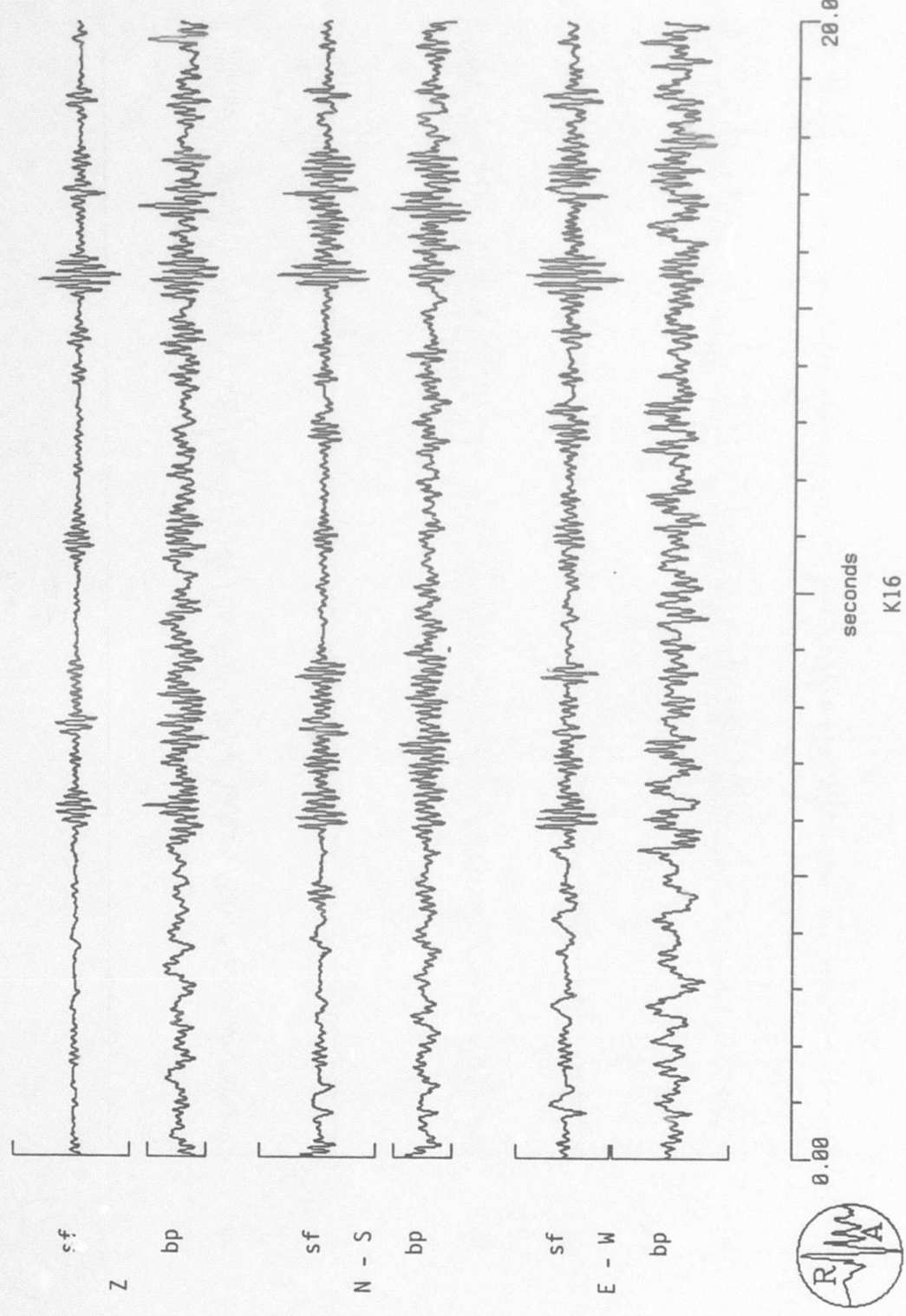
Figure 56. State filtered (sf) and band-pass filtered (bp) *P*-wave data for event K16, Δ=797 km. The band-pass filter passed frequencies between 2 and 15 Hz. The polarization state filter was applied to the band-passed data and passed rectilinear motion.
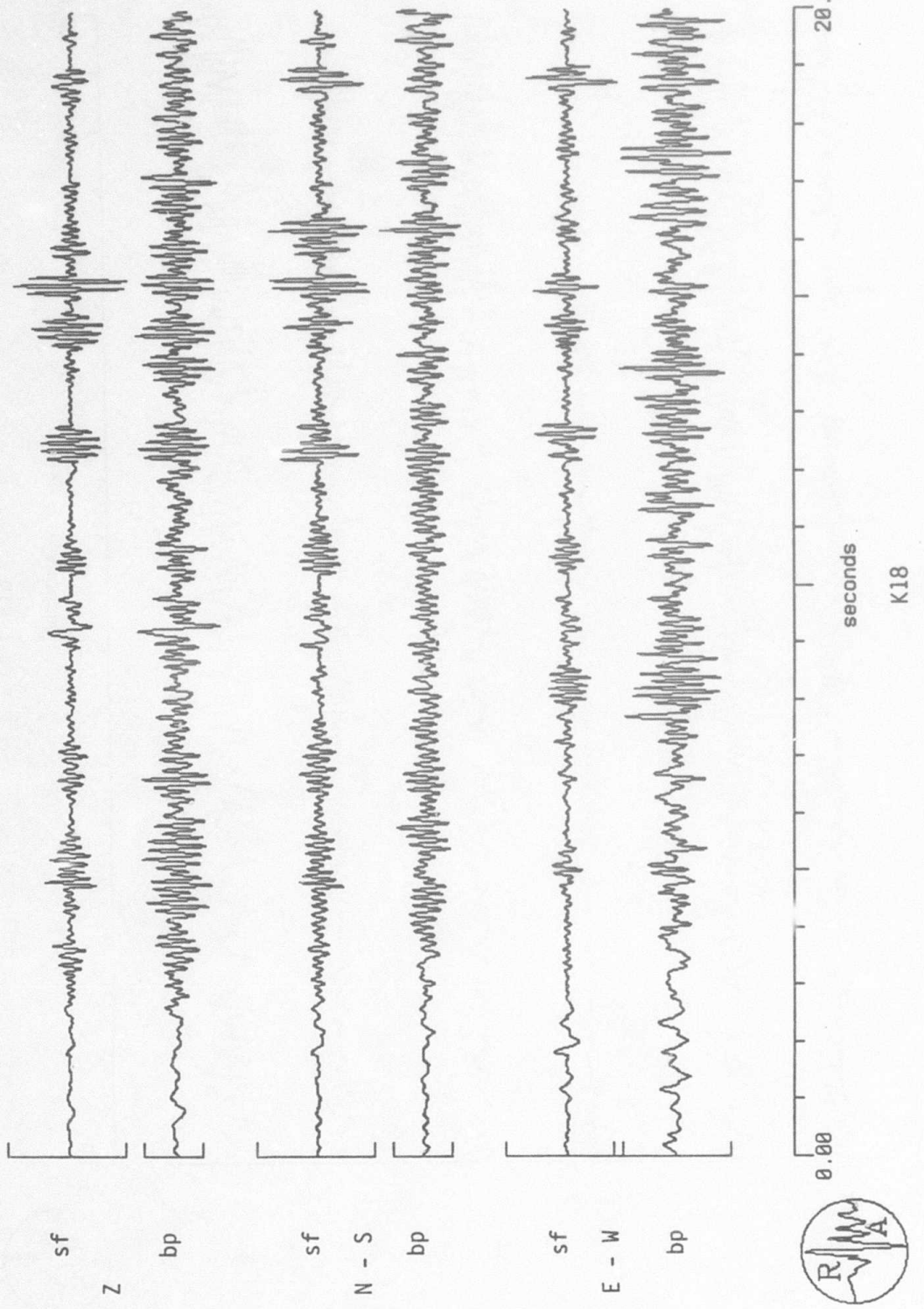
Figure 57. State filtered (sf) and band-pass filtered (bp) *P*-wave data for event K18, $\Delta = 788$ km. The band-pass filter passed frequencies between 2 and 15 Hz. The polarization state filter was applied to the band-passed data and passed rectilinear motion.

85
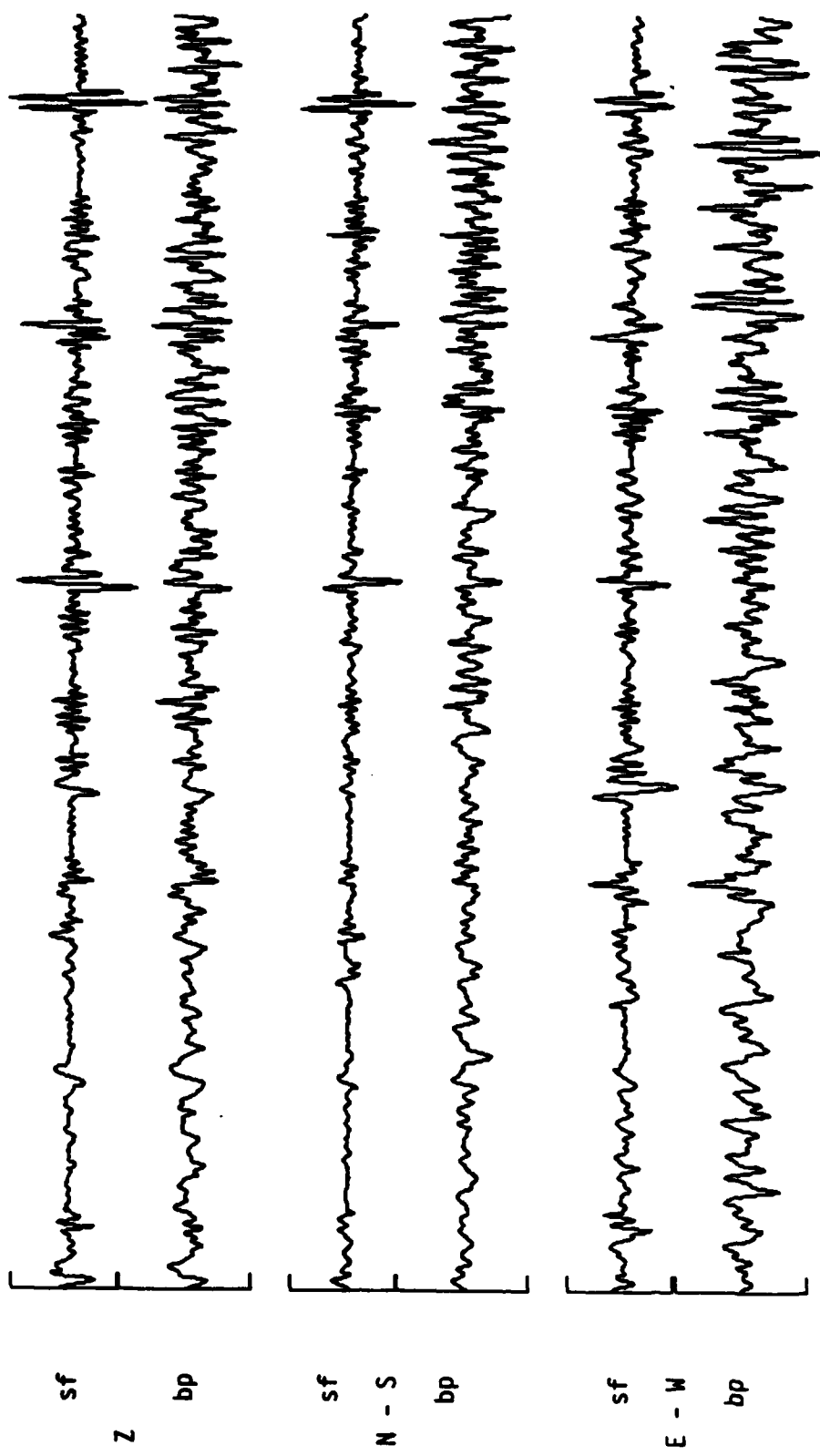
Figure 58. State filtered (sf) and band-pass filtered (bp) *P*-wave data for event K10, Δ=1307 km. The band-pass filter passed frequencies between 2 and 15 Hz. The polarization state filter was applied to the band-passed data and passed rectilinear motion.
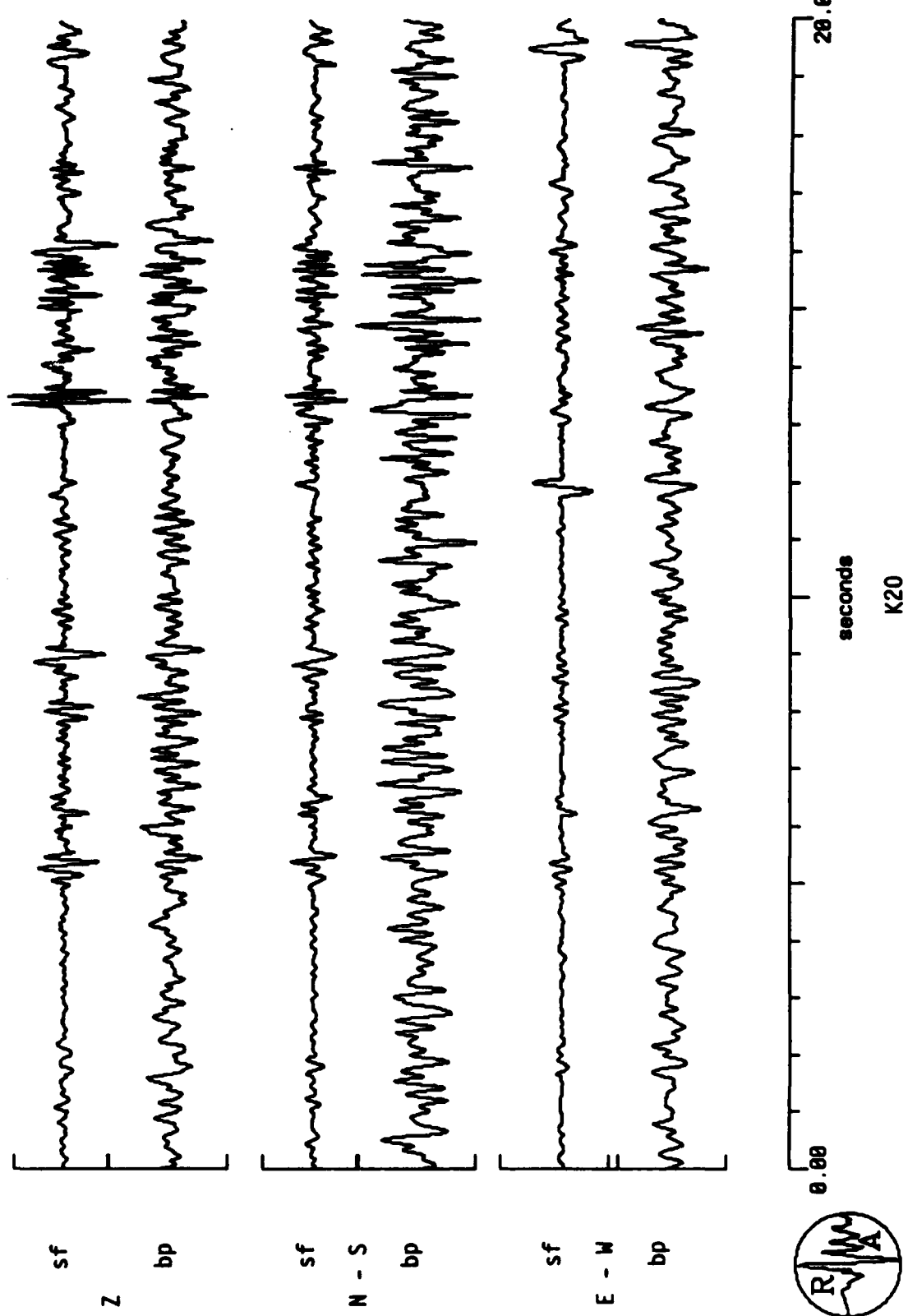
Figure 50. State filtered (sf) and band-pass filtered (bp) *P*-wave data for event K20, Δ=1291 km. The band-pass filter passed frequencies between 2 and 15 Hz. The polarization state filter was applied to the band-passed data and passed rectilinear motion.

SECTION V.

SUMMARY AND CONCLUSIONS

Application of the depth phase method for event depth determination in the northeastern U.S. and the Kuril/Kamchatka area gave mixed results. In the northeast, excellent results were obtained (see Table 5) while in the Kuril/Kamchatka area very poor performance was recorded. The conditions that led to the dramatic contrast in the results can be used to quantify the method's strengths and weaknesses.

One major difference between the two data sets is signal-to-noise ratios. With the exception of the Amsterdam earthquake and quarry blast, all of the recorded signals for the northeast events have good signal-to-noise ratios, whereas signal-to-noise ratios for the Kamchatka data were poor. This was due, in part, to the difference in epicentral distances; for northeast events all epicentral distances are less than 330 km, while for the Kamchatka data they are all between 570 and 1301 km. Also, the propagation paths from many of the Kamchatka events traverse a major tectonic boundary, the Kuril Trench, and this may contribute to a decrease in signal-to-noise. The signal-to-noise ratio plays a significant role in the depth determinations. Tests of the polarization state filter method used to help isolate depth phases have shown that performance degrades significantly below signal-to-noise ratios of 1. This hampered the efforts to identify depth phases for the Kamchatka events.

The second major difference between the data sets is the data quality. Data collected in the northeast U.S. were recorded by broad band stations RSNY and SRNY. Both record data digitally and have well known characteristics. The OSS data, collected using a remote sea-bottom recording system, has problems with skew, timing, and possibly instrument noise. The polarization methods described in this report require that the three components of motion be accurately aligned in time. Although skew was corrected for in the OSS data, some inaccuracies may have persisted.

The physical location of the recording stations also contributed to differences between the data sets. Both RSNY and SRNY are well coupled stations at or near the free surface of the Earth. In contrast, OSS-IV is well below the sea floor in deep ocean. Superimposed upon the upgoing seismic wavefield at OSS-IV are reflections from the sea-bottom interface and the sea surface. The resulting wavefield is complicated, making use of the adaptive polarization method for phase identification of minimal value as well as reducing the effectiveness of the polarization state filter.

Another difference that bears on the results is the way the two data sets were analyzed. The northeastern seismograms were compared to synthetic depth sections, whereas we simply attempted to pick upgoing and downgoing phases on the complex Kamchatka seismograms. The synthetic seismograms guided our identification of phases considerably and, without them, it would have been very difficult to identify properly-paired primary and depth phases in the northeastern data.

The preceding discussion pointed out possible reasons that the depth phase method gave depths consistent with reported depths for the northeastern U.S. data but did not work on the Kamchatka/Kuril data. In the course of applying the method to the northeastern data, we found that several other conditions were important for its success. The Ardsley event revealed that source complexity is possible in small events and that the phases associated with the complexity could be misidentified as depth phases. Since identification of phases can be aided by synthetic seismograms, it is important to have a measure of the validity of the models. A models' robustness could be tested by successfully modeling the data from several different receiving stations. Unfortunately, we do not often have on-scale digital data, especially three-component data, from more than one station in the northeast. Nevertheless, we can afford a certain degree of confidence in the modelling and interpretation of earthquakes we selected because: 1. the epicenters are well located by dense regional networks, 2. some of the depths are also well determined by virtue of close-in permanent or temporary stations, 3. for more than half the earthquakes, fault-plane-solutions have been obtained from P-wave first motions and 4. several regional velocity structures have been estimated from refraction experiments, teleseismic residuals, and travel-time curves. More comparisons need to be made, however, to establish whether the velocity models so derived (#4 above) are the most appropriate for waveform modelling at the frequencies of interest. It is apparent from the comparisons we have presented here that the data are not perfectly modelled by the synthetics. Future investigations should focus on improving these results through better understanding of both data and synthetics. Now that digital data are available from regional networks , there is great potential for discovering much more about source mechanics and crustal phase propagation. Future insights can give us a better idea of how to model the entire source-path-receiver system.

In conclusion, the depth phase method for depth determination can work quite well under certain conditions. The problem that remains to be solved is to identify when these conditions are met for a particular data set.

REFERENCES

Archambeau, C. B., J. C. Bradford, P. W. Broome, W. C. Dean, E. A. Flinn, and R. L. Sax, "Data processing techniques for the detection and interpretation of teleseismic signals," *Proc. IEEE*, vol. 53, pp. 1860-1884, 1965.

Bakun, W. H., R. M. Stewart, and C. G. Bufe, "Directivity in the high-frequency radiation of small earthquakes," *Bull Seism. Soc. Am.*, vol. 68, pp. 1253-1263, 1978.

Barstow, N. L., J. A Carter, and A. Suteau-Henson, "Focal depths of shallow local earthquakes from comparison of polarization filtered data with synthetics," *abstr. Earthquake Notes*, vol. 57, No.1, pp. 1860-1884, 1986.

Brown, E. J. and J. E. Ebel, "An investigation of the January 1982 aftershock sequence near Laconia, New Hampshire," *submitted to Earthquake Notes*, 1985.

Douglas, A., J. A. Hudson, and P. D. Marshall, "Earthquake seismograms that show Doppler effects due to crack propagation," *Geophys. J.*, vol. 64, pp. 163-185, 1981.

Ebel, J. E. and J. P. McCaffrey, S. J., "Hypocentral parameters and focal mechanisms of the 1983 earthquake near Dixfield, Maine," *Earthquake Notes*, vol. 55, No. 2, pp. 21-24, 1984.

Frankel, A. and H. Kanamori, "Determination of rupture duration and stress drop for earthquakes in southern California," *Bull. Seism. Soc. Am.*, vol. 73A, pp. 1527-1552, 1983.

Hartzell, S. H., "Earthquake aftershocks as Green's functions," *Geophys. Res. Letters*, vol. 5, pp. 1-4, 1978.

Harvey, D., "Seismogram synthetics using normal mode superpostion: the locked mode approximation method," *Geophys. J. Roy. Astr. Soc.*, vol. 66, pp. 37-69, 1981.

Houlday, M., R. Quittmeyer, K. Mrotek, and C. T. Statton, "Recent seismicity in north and east-central New York State," *Earthquake Notes*, vol. 55, No. 2, pp. 16-24, 1984.

Kanamori, H. and D. L. Anderson, "Theoretical basis of some empirical relations in seismology," *Bull Seism. Soc. Am.*, vol. 65, pp. 1073-1095, 1975.

Kanamori, H. and G. S. Stewart, "Seismological aspects of the Guatemala earthquake of February 9, 1976," *J. Geophys. Res*, vol. 83, pp. 3427-3434, 1978.

Kanamori, H., "A semi-empirical approach to prediction oflong-period ground motions from great earthquakes," *Bull. Seism. Soc. Am.*, vol. 69, pp. 1654-1670, 1979.

Khattri, K., "Body wave directivity functions for two-dimensional fault model and kinematic parameters of deep focus earthquake," *J. Geophys. Res*, vol. 77, pp. 2062-2071, 1978.

Mitchell, B. J., "Regional variation and frequency dependence on Q_β in the crust of the United States," *BSSA*, vol. 71, No. 5, pp. 1531-1538, 1981.

Mueller, C. S., "Source pulse enhancement by deconvolution of an empirical Green's function," *Geophys. Res. Letters*, vol. 12, pp. 33-36, 1985.

Pulli, J. J., J. C. Nabelek, and J. M. Sauber, "Source parameters of the January 19, 1982 Gaza, New Hampshire earthquake," *abstr. Earthquake Notes*, vol. 54, No. 3, pp. 28-29, 1983.

Samson, J. C., "Matrix and Stokes vector representations of detectors for polarized waveforms: theory with some applications to teleseismic waves," *Geophys. J. Roy. Astr. Soc.*, vol. 51, pp. 583-603, 1977.

Samson, J. C. and J. V. Olson, "Data-adaptive polarization filters for multichannel geophysical data," *Geophysics*, vol. 46 No. 10, pp. 1423-1431, 1981.

Schlesinger-Miller, E., N. L. Barstow, and A. L. Kafka, "The July 1981 earthquake sequence near Cornwall, Ontario and Massena, New York," *Earthquake Notes*, vol. 54, No.3, pp. 11-26, 1983.

Seeber, L., E. Cranswick, N. Barstow, J. Armbruster, G. Suarez, K. Coles, and C. Aviles, "Grenville structure and the Central Adirondack seismic zone including the October 7, 1983 mainshock-aftershock sequence Canadian Geophysical Union Meeting," *Halifax, Nova Scotia*, 1984a.

Seeber, L., E. Cranswick, J. Armbruster, and N. Barstow, "The October 1983 Goodnow, NY aftershock sequence; regional seismicity and structural features in the Adirondacks," *AGU abstr.*, vol. 65, No.16, p. 239, 1984b.

Seeber, L., J. G. Armbruster, and D. Coyle, "A prolonged, but spatially concentrated earthquake sequence at the northern outskirts of New York City," *abstr. SSA, Earthquake Notes*, vol. 57, No. 1, p. 18, 1986.

Suarez, G., L. Seeber, C. Aviles, and E. Schlesinger, "The Goodnow, NY earthquake: results of a broad band teleseismic analysis," *AGU abstr.*, vol. 65, No.16, p. 239, 1984.

Sutton, G. H. and P. W. Pomeroy, "Analog analysis of seismograms recorded on magnetic tape," *J. Geophys. Res.*, vol. 68, pp. 2791-2815, 1963.

Taylor, S. R., M. N. Toksoz, and M. P. Chaplin, "Crustal structure of the Northeastern United States: Contrasts between Grenville and Appalachian Provinces," *Science*, vol. 208, pp. 595-597, 1980.

Taylor, S. R. and B. J. Qualheim, "Regional seismic test network site descriptions," *UCID-19769*, Lawrence Livermore Laboratory, 1983.

Trifunac, M. D. and J. N. Brune, "Complexity of energy release during the Imperial Valley, California, earthquake of 1940," *Bull Seism. Soc. Am.*, vol. 60, pp. 137-160, 1970.

Wahlstrom, R., "The North Gower, Ontario, earthquake of 11 October 1983; focal mechanism and aftershocks," *submitted to Earthquake Notes*, 1985.

91

White, J. E., "Motion product seismograms," *Geophys.*, vol. 29, pp. 288-298, 1964.

Yang, J. and Y. P. Aggarwal, "Seismotectonics of northeastern United States and adjacent Canada," *J. of Geophys. Res.*, vol. 86, No.B6, pp. 4981-4998, 1981.

RECIPIENT   **NUMBER OF COPIES**

DEPARTMENT OF DEFENSE

DARPA/GSD
ATTN: Dr. R. Alewine and Dr. R. Blandford   2
1400 Wilson Boulevard
Arlington, VA 22209-2308

DARPA/PM   1
1400 Wilson Boulevard
Arlington, VA 22209-2308

Defense Intelligence Agency   1
Directorate for Scientific and
  Technical Intelligence
Washington, D.C. 20301

Defense Nuclear Agency   1
Shock Physics
Washington, D.C. 20305-1000

Defense Technical Information Center   12
Cameron Station
Alexandria, VA 22314

DEPARTMENT OF THE AIR FORCE

AFGL/LWH   2
ATTN: Dr. J. Cipar and Mr. J. Lewkowicz
Terrestrial Sciences Division
Hanscom AFB, MA 01731-5000

AFOSR/NPG   1
ATTN: Director
Bldg 410, Room C222
Bolling AFB, Washington, D.C. 20332

AFTAC/CA   1
ATTN: STINFO Officer
Patrick AFB, FL 32925-6001

AFTAC/TG   3
Patrick AFB, FL 32925-6001

AFWL/NTESG   1
Kirtland AFB, NM 87171-6008

DEPARTMENT OF THE NAVY

NORDA   1
ATTN: Dr. J. A. Ballard
Code 543
NSTL Station, MS 39529

DEPARTMENT OF ENERGY

Department of Energy   1
ATTN: Mr. Max A. Koontz (DP-52)
International Security Affairs
1000 Independence Avenue
Washington, D.C. 20545

Lawrence Livermore National Laboratory   2
ATTN: Dr. J. Hannon and Dr. M. Nordyke
University of California
P.O. Box 808
Livermore, CA 94550

Los Alamos Scientific Laboratory   2
ATTN: Dr. K. Olsen and Dr. T. Weaver
P.O. Box 1663
Los Alamos, NM 87544

Sandia Laboratories   1
ATTN: Mr. P. Stokes
Geosciences Department 1255
Albuquerque, NM 87185

OTHER GOVERNMENT AGENCIES

Central Intelligence Agency   1
ATTN: Dr. L. Turnbull
OSI/NED, Room 5G48
Washington, D.C. 20505

U. S. Arms Control and Disarmament Agency   1
ATTN; Dr. M. Eimer
Verification and Intelligence Bureau, Rm 4953
Washington, D.C. 20451

U. S. Arms Control and Disarmament Agency   1
ATTN: Mrs. M. Hoinkes
Multilateral Affairs Bureau, Rm 5499
Washington, D.C. 20451

U. S. Geological Survey   1
ATTN: Dr. T. Hanks
National Earthquake Research Center
345 Middlefield Road
Menlo Park, CA 94025

U. S. Geological Survey MS-913   1
ATTN: Dr. R. Masse
Global Seismology Branch
Box 25046, Stop 967
Denver Federal Center
Denver, CO 80225

UNIVERSITIES

Boston College   1
ATTN: Dr. A. Kafka
Western Observatory
381 Concord Road
Weston, MA 02193

California Institute of Technology   1
ATTN: Dr. D. Harkrider
Seismological Laboratory
Pasadena, CA 91125

Columbia University   1
ATTN: Dr. L. Sykes
Lamont-Doherty Geological Observatory
Palisades, NY 10964

Cornell University   1
ATTN: Dr. M. Barazangi
INSTOC
Snee Hall
Ithaca, NY 14853

Harvard University   1
ATTN: Dr. J. Woodhouse
Hoffman Laboratory
20 Oxford Street
Cambridge, MA 02138

Massachusetts Institute of Technology   3
ATTN: Dr. S. Soloman, Dr. N. Toksoz, and Dr. T. Jordan
Department of Earth and Planetary Sciences
Cambridge, MA 02139

Southern Methodist University   1
ATTN: Dr. E. Herrin
Geophysical Laboratory
Dallas, TX 75275

State University of New York at Binghamton   1
ATTN: Dr. P. Wu
Department of Geological Sciences
Vestal, NY 13901

St. Louis University   2
ATTN: Dr. O. Nuttli and Dr. R. Herrmann
Department of Earth and Atmospheric Sciences
3507 Laclede
St. Louis, MO   63156

The Pennsylvania State University   1
ATTN: Dr. S. Alexander
Geosciences Department
403 Deike Building
University Park, PA   16802

University of Arizona   1
ATTN: Dr. T. Wallace
Department of Geosciences
Tucson, AZ   85721

University of California, Berkeley   1
ATTN: Dr. T. McEvilly
Department of Geology and Geophysics
Berkeley, CA   94720

University of California Los Angeles   1
ATTN: Dr. L. Knopoff
405 Hilgard Avenue
Los Angeles, CA   90024

University of California, San Diego   1
ATTN: Dr. J. Orcutt
Scripps Institute of Oceanography
La Jolla, CA   92093

University of Colorado   1
ATTN: Dr. C. Archambeau
CIRES
Boulder, CO   80309

University of Illinois   1
ATTN: Dr. S. Grand
Department of Geology
1301 West Green Street
Urbana, IL   61801

University of Michigan   1
ATTN: Dr. T. Lay
Department of Geological Sciences
Ann Arbor, MI   48109-1063

University of Nevada   1
ATTN: Dr. K. Priestley
Mackay School of Mines
Reno, NV   89557

UNIVERSITIES (continued)

University of Southern California   1
ATTN: Dr. K. Aki
Center for Earth Sciences
University Park
Los Angeles, CA   90089-0741

DEPARTMENT OF DEFENSE CONTRACTORS

Applied Theory, Inc.   1
ATTN: Dr. J. Trulio
930 South La Brea Avenue
Suite 2
Los Angeles, CA   90036

Center for Seismic Studies   2
ATTN: Dr. C. Romney and Mr. R. Perez
1300 N. 17th Street, Suite 1450
Arlington, VA   22209

ENSCO, Inc.   1
ATTN: Mr. G. Young
5400 Port Royal Road
Springfield, VA   22151

ENSCO, Inc.   1
ATTN: Dr. R. Kemerait
445 Pineda Court
Melbourne, FL   32940

Gould Inc.   1
ATTN: Mr. R. J. Woodard
Chesapeake Instrument Division
6711 Baymeado Drive
Glen Burnie, MD   21061

Pacific Sierra Research Corp.   1
ATTN: Mr. F. Thomas
12340 Santa Monica Boulevard
Los Angeles, CA   90025

Rockwell International   1
ATTN: B. Tittmann
1049 Camino Dos Rios
Thousand Oaks, CA   91360

Rondout Associates, Inc.   1
ATTN: Dr. P. Pomeroy
P.O. Box 224
Stone Ridge, NY   12484

Science Applications, Inc.   1
ATTN: Dr. T. Bache, Jr.
P.O. Box 2351
La Jolla, CA   92038

Science Horizons   2
ATTN: Dr. T. Cherry and Dr. J. Minster
710 Encinitas Blvd.
Suite 101
Encinitas, CA   92024

Sierra Geophysics, Inc.   2
ATTN: Dr. R. Hart and Dr. G. Mellman
11255 Kirkland Way
Kirkland, WA   98124

SRI International   1
ATTN: Dr. A. Florence
333 Ravensworth Avenue
Menlo Park, CA   94025

S-Cubed A Division of   1
Maxwell Laboratories Inc.
ATTN: Dr. S. Day
P.O. Box 1620
La Jolla, CA   92038-1620

S-Cubed, A Division of   1
Maxwell Laboratories Inc.
ATTN: Mr. J. Murphy
11800 Sunrise Valley Drive
Suite 1112
Reston, VA   22091

Teledyne Geotech   2
ATTN: Dr. Z. Der and Mr. W. Rivers
314 Montgomery Street
Alexandria, VA   22314-1581

Woodward-Clyde Consultants   2
ATTN: Dr. L. Burdick and Dr. J. Barker
556 El Dorado Street
Pasadena, CA   91109

NON-US RECIPIENTS

Blacknest Seismological Center   1
ATTN: Mr. Peter Marshall
Atomic Weapons Research Establishment
UK Ministry of Defense
Brimpton, Reading RG7-4RS
United Kingdom

National Defense Research Institute   1
ATTN: Dr. Ola Dahlman
Stockholm 80, Sweden

NON-US RECIPIENTS

NTNF NORSAR
ATTN: Dr. Frode Ringdal   1
P.O. Box 51
N-2007 Kjeller
Norway

OTHER DISTRIBUTION

To be determined by the project office